

Ambient Pressure Oxidation of Ag(111) Surfaces: An in-situ X-Ray Study

Von der Fakultät Mathematik und Physik der Universität Stuttgart
zur Erlangung der Würde eines Doktors der
Naturwissenschaften (Dr. rer. nat.) genehmigte Abhandlung

Vorgelegt von
ALEXANDER REICHO
aus Bremen

Hauptberichter: Prof. Dr. H. Dosch
Mitberichter: Prof. Dr. U. Stroth

Eingereicht am: 07. November 2007
Tag der mündlichen Prüfung: 08. Februar 2008

Institut für Theoretische und Angewandte Physik
der Universität Stuttgart
Max-Planck-Institut für Metallforschung
in Stuttgart

Contents

Contents	v
1 Introduction	1
2 Interaction of Oxygen with Ag(111) Surfaces	3
2.1 Silver and Ag ₂ O	3
2.2 Oxidation of Ag(111) Surfaces	4
2.3 Motivation for our Experiments	11
3 Theoretical Background	13
3.1 X-Ray Diffraction	14
3.2 High Resolution Core Level Spectroscopy	24
3.3 Normal Incidence X-Ray Standing Waves	26
3.4 Low Energy Electron Diffraction	34
3.5 Auger Electron Spectroscopy	36
4 Experimental Details	37
4.1 Sample Preparation	37
4.2 Surface X-Ray Diffraction	38
4.3 High Resolution Core Level Spectroscopy	41
4.4 Normal Incidence X-Ray Standing Wave Absorption	42
5 Structure of O-p(4×4)/Ag(111)	45
5.1 Preparation by O ₂ and NO ₂	45
5.2 Decomposition of the p(4×4) reconstruction	50
5.3 Comparison with previously discussed Models	52
5.4 Structural Model of O-p(4×4)/Ag(111)	53
5.5 Stability Diagram of the p(4×4) structure	59
6 A Zoo of Oxygen Induced Structures	63
6.1 The clean Ag(111) Surface	63
6.2 Disordered chemisorbed Oxygen	64
6.3 Periodic Structures induced by chemisorbed Oxygen	69

6.4	Reconstructions involving adsorbed Silver Triangles	74
6.5	Structures related to $\text{Ag}_2\text{O}(\bar{1}\bar{1}\bar{1})$	77
6.6	Stability Diagram of the O/Ag(111)-system	82
7	Summary	87
A	2 and 3D Crystallography	91
A.1	Ag(111) Surfaces	91
A.2	2D Crystallography, Wood and Matrix notation	92
B	Theoretical Methods	95
B.1	Density Functional Theory	95
B.2	<i>Ab initio</i> Thermodynamics	96
C	Abbreviations and Acronyms	99
D	Symbols used in Equations	101
	Bibliography	105

Deutsche Zusammenfassung

Einleitung und Motivation

Die Oxidation von Metallen ist ein allgegenwärtiges Phänomen. Häufig beobachtet man das Rosten von Stahl oder die grüne Patina auf Kupferoberflächen. Die kontrollierte Oxidation von Metalloberflächen führt aber auch zu erwünschten Materialeigenschaften, hierbei haben passivierende Oxidschichten auf rostfreiem Stahl eine besondere technische Bedeutung. Von besonderer Relevanz für die vorliegende Arbeit ist die heterogene Katalyse, die für die industrielle Synthese einer Vielzahl von chemischen Verbindungen verwendet wird, wobei Edukte und Produkte gasförmig vorliegen und die Reaktionen auf der festen Katalysatoroberfläche stattfinden. Oxidationsreaktionen spielen dabei eine wichtige Rolle, dementsprechend gibt es große Bemühungen in Forschung und Entwicklung, die zum Verständnis der relevanten Prozesse beitragen sollen. Dies beinhaltet die Bestimmung der aktiven Sauerstoffspezies auf der Katalysatoroberfläche und Studien zur Selektivität und Deaktivierung des Katalysators auf atomarer Ebene.

Besonderes Augenmerk wird auf die Oxidation der 4d Übergangsmetalle Ru, Rh, Pd und Ag bei hohen Temperaturen und hohem Sauerstoffdruck gerichtet, da diese als Katalysator für eine Vielzahl von Oxidationsreaktionen verwendet werden [1]. Auf der Ru(0001) Oberfläche beobachtet man die Bildung des Bulkoxids $\text{RuO}_2(110)$ [2], während sich auf den Pd(100) und Rh(111) Oberflächen sogenannte Oberflächenoxide bilden [3, 4]. Ein Oberflächenoxid ist eine dreilagige ultradünne Oxidschicht, die dem entsprechenden Bulkoxid strukturell ähnelt, wobei eine metallische Lage von zwei Sauerstoffschichten umgeben ist, was zu einer Sauerstoff-Metall-Sauerstoff Stapelabfolge führt.

Silber besitzt eine einmalige Stellung als Katalysator. Es wird für die Epoxidation von Ethylen und die partielle Oxidation von Methanol zu Formaldehyd verwendet. Diese Oxidationsreaktionen laufen bei einer Temperatur von 500 bis 900 K und atmosphärischem Sauerstoffdruck ab. Sowohl Ethylenoxid als auch Formaldehyd sind wichtige Grundstoffe der chemischen Industrie, daher ist man an einer Optimierung dieser silberkatalysierten Reaktionen interessiert. Heutzutage versucht man die Selektivität der Reaktionen aufgrund empirischer Erfahrungen durch die Beimischung sogenannter Inhibitoren (I) [5] und Promotoren (P) zu verbessern [6, 7]. In diesem Zusammenhang versucht man eine direkte mikroskopische Kontrolle über die auftre-

tenden Oberflächenstrukturen zu erlangen und zukünftig die Dynamik der Oxidations- und Reduktionsreaktionen in Echtzeit zu analysieren. Ein wichtiger Schritt in diese Richtung ist die Aufklärung der sauerstoffinduzierten Oberflächenstrukturen auf atomarer Ebene, die sich unter hohen Temperaturen und hohem Sauerstoffdruck bilden.

Man beobachtet die Bildung ausgedehnter Ag(111) Facetten auf polykristallinem Silber unter den industriell angewendeten Bedingungen der katalytischen Reaktionen [8]. Aus diesem Grund beschäftigten sich eine Vielzahl theoretischer und experimenteller Studien mit dem Oxidationsverhalten der Ag(111) Oberfläche [8–21]. Seit den frühen 70iger Jahren ist die Bildung einer sauerstoffinduzierten $p(4\times 4)$ Rekonstruktion bekannt [9, 10]. Auf Basis von STM (Scanning Tunneling Microscopy) Messungen und DFT (Density Functional Theory) Berechnungen wurde für diese Rekonstruktion eine dreilagige Oberflächenoxidstruktur vorgeschlagen, die auf dem Bulkoxid $\text{Ag}_2\text{O}(111)$ beruht [15, 16]. Die Oxidation der Ag(111) Oberfläche schien daher ein ähnliches Oxidationsverhalten, wie das der im Periodensystem benachbarten Elemente Pd und Rh, aufzuweisen. Des Weiteren wurde die Stabilität der $p(4\times 4)$ Struktur unter industriell relevanten Bedingungen durch theoretische Berechnungen vorhergesagt [16, 22].

Einige Fragen blieben dennoch ungelöst. Die Stabilität der $p(4\times 4)$ Rekonstruktion unter industriell relevanten Bedingungen wurde experimentell nicht nachgewiesen, das Strukturmodell der $p(4\times 4)$ Struktur wurde durch keine kristallographische Methode bestätigt und bis dato unbekannte sauerstoffinduzierte Strukturen könnten eine wichtige Rolle für die katalytische Aktivität von Ag(111) Facetten spielen. Unser experimenteller Ansatz basiert auf der Anwendung von heutzutage verfügbarer hochbrillanter Röntgenstrahlung, die von Synchrotrons der dritten Generation erzeugt wird. Dabei wird eine Kombination von drei oberflächensensitiven Methoden verwendet. In-situ SXRD (Surface X-Ray Diffraction) erlaubt die Bestimmung von Rekonstruktionstypen und deren Struktur mit einer Auflösung im sub-Å-Bereich. Dabei lässt sich das sogenannte 'pressure gap' schließen, welches die Differenz zwischen UHV Untersuchungen und den katalytischen Bedingungen beschreibt. HRCLS (High Resolution Core Level Spectroscopy) ermöglicht Aussagen über die lokale chemische Umgebung der Sauerstoff- und Silberatome. NIXSW (Normal Incidence X-Ray Standing Wave Absorption) ist eine Kombination aus Diffraktion und Spektroskopie, die die Bestimmung der Atompositionen bezüglich der Ag(111) Ebenen zulässt. Des Weiteren haben wir systematische LEED (Low Energy Electron Diffraction) Messungen durchgeführt, wobei vormals unbekannte Rekonstruktionen der Ag(111) Oberfläche bestimmt werden können.

Theoretische Grundlagen

Oberflächenröntgenbeugung

Oberflächenröntgenbeugung (SXR) basiert auf der elastischen Streuung von Röntgenstrahlen an Elektronen [23–29]. Im Gegensatz zur Streuung am Volumenkristall führt die Präsenz der Oberfläche zu einer Unterbrechung der Periodizität entlang der Oberflächennormalen. Dies hat zur Folge, dass die destruktive Interferenz zwischen den Bragg Peaks entlang dieser Richtung nicht mehr vollständig ist und diffus gestreute Intensität entlang sogenannter reziproker Gitterstäbe (Crystal Truncation Rod CTR) beobachtet werden kann. Die gestreute Intensität ist proportional zum Betragsquadrat des Strukturformfaktors F_{total} , der durch folgende Beziehung gegeben ist

$$F_{\text{total}} = \sum_{\mathbf{r}_j}^{\text{Volumen Einheitszelle}} f_j(\mathbf{q}) e^{i\mathbf{q}\cdot\mathbf{r}_j} * \frac{1}{1 - e^{i2\pi L}} + \Theta \sum_{\mathbf{r}_s}^{\text{Oberflächen Einheitszelle}} f_s(\mathbf{q}) e^{i\mathbf{q}\cdot\mathbf{r}_s}.$$

Hierbei ist f der atomare Formfaktor, \mathbf{q} der Impulsübertrag des Streuprozesses gegeben durch den Vektor (H, K, L) , L die Komponente des Impulsübertrags parallel zur Oberflächennormalen und Θ ist die Bedeckung der Oberfläche mit der jeweiligen Rekonstruktion. SXR Messungen werden normalerweise unter streifendem Einfall durchgeführt um das Untergrundsignal zu minimieren. Die Streugeometrie eines Oberflächenröntgenbeugungsexperiments ist in Abbildung 1 dargestellt.

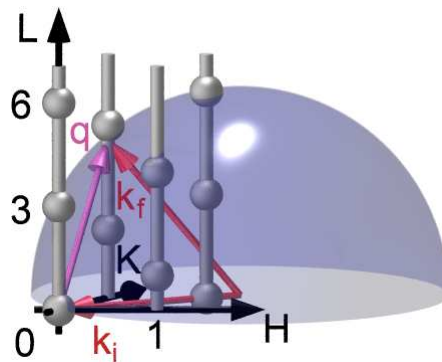


Abbildung 1: Ewaldkugel für SXR Streugeometrie unter streifendem Einfall. Die einfallende Welle breitet sich entlang der $(\bar{1}\bar{1}0)$ Richtung aus. Der Radius der Ewaldkugel entspricht einer Photonenenergie von 10,5 keV. Die CTRs der Ag(111) Oberfläche sind als Stäbe dargestellt und die Bragg Peaks als Kugeln.

Es sei hier noch erwähnt, dass eine Rekonstruktion der Oberfläche zu einer Vergrößerung der Periodizität der Einheitszelle in der Oberflächenebene führt. Eine Verdoppelung der Größe entlang der (100) Richtung führt zum Auftreten von Reflexen bei

Vielfachen von $(1/2,0,0)$. Wie im Fall der CTRs ist das Signal entlang der L -Richtung auf sogenannten Oberflächenrods verteilt. Die Oberflächenrods weisen eine intrinsische Oberflächensensitivität auf, da ihr Signal nur von Streuung an Atomen herrührt, die Teil der Rekonstruktion sind.

Hoch aufgelöste Spektroskopie von Rumpfniveaus

HRCLS ist auch unter dem Namen X-ray Photoelectron Spectroscopy (XPS) bekannt [30–32]. Man differenziert in der Namensgebung, um deutlich zu machen, dass HRCLS Experimente an Synchrotronstrahlungsquellen durchgeführt werden. Diese Technik basiert auf der Emission von Photoelektronen aus Rumpfniveaus durch die einfallende Röntgenstrahlung. Die relevante Größe ist die Bindungsenergie der Elektronen E_{bind} , die folgendermaßen definiert ist

$$E_{\text{bind}} = h\nu - E_{\text{kin}} - \Phi .$$

Hierbei ist $h\nu$ die Photonenenergie, E_{kin} die kinetische Energie der Photoelektronen und Φ die Austrittsarbeit des Metalls bezüglich der Fermienergie. Obwohl die Rumpfniveauelektronen nicht direkt an der Bindung der Silber- und Sauerstoffatome beteiligt sind, beobachtet man in Photoelektronenspektren sogenannte chemische Verschiebungen, die von der lokalen chemischen Umgebung des jeweiligen Atoms abhängen. Die gemessenen Spektren lassen sich in mehrere Komponenten zerlegen und man kann daraus z.B. Aussagen über die Anzahl der verschiedenen Sauerstoffatomspezies treffen. Diese Methode zeichnet sich durch eine hohe Oberflächensensitivität aus, da nur Photoelektronen aus den obersten Atomlagen die Probe verlassen.

Absorption stehender Röntgenwellen unter normalem Einfall

NIXSW ist eine Kombination von Röntgenbeugung und XPS. Die beobachteten Effekte lassen sich mittels der dynamischen Röntgenbeugungstheorie beschreiben [23, 24, 33–35]. Die einfallende und die gestreute Röntgenwelle bilden eine stehende Röntgenwelle inner- und außerhalb des Kristalls aus. Die Position des Wellenfeldes lässt sich um einen halben Gitterebenenabstand variieren, wenn man über den entsprechenden Bragg Peak scannt. Dies erfolgt entweder durch Änderung des Streuwinkels oder durch Variation der Photonenenergie. Die Maxima des Wellenfeldes bewegen sich dabei von einer Position zwischen den Streuebenen auf die Streuebenen. Dementsprechend beobachtet man eine charakteristische Variation des XPS Signals, welches maximal wird, wenn die Maxima des Wellenfeldes auf den Streuebenen liegen. Metallkristalle weisen eine große Mosaizität auf. Aus diesem Grund strahlt man die Röntgenwelle unter normalem Einfall ein, was zu einer maximalen Breite des Bragg Peaks führt [36], die dann größer als die Mosaizität des Kristalls ist. Die Photoelektronenausbeute $Y_{\text{dip}}^{\text{H}}$, in Dipolnäherung für den Photoemissionsprozess, ist gegeben durch

$$Y_{\text{dip}}^{\text{H}} = 1 + R + 2 P \sqrt{R} F^{\text{H}} \cos(v - 2\pi P^{\text{H}}).$$

Hierbei ist H der Impulsübertrag des jeweiligen Bragg Peaks, P ist eine Korrektur, die von der Polarisation der einfallenden Röntgenstrahlung abhängt, R die reflektierte Röntgenintensität und v ist die Phase zwischen der einfallenden und gestreuten Röntgenwelle. P^{H} ist die kohärente Position, die die Position der Atome, deren XPS Signal man detektiert, relativ zu H angibt. F^{H} ist die kohärente Fraktion, die ein Maß für die Ordnung der Verteilung um die mittlere Position ist, welche durch P^{H} gegeben ist. Sowohl P^{H} als auch F^{H} können Werte zwischen 0 und 1 annehmen. Die Profile der Photoelektronenausbeute Y lassen sich fiten und man kann dann eine Aussage über die Lage und Verteilung der Sauerstoff- und Silberatome relativ zur Position der Ag(111) Ebenen treffen.

Beugung niederenergetischer Elektronen

LEED basiert auf der elastischen Streuung von Elektronen, wobei eine Rückstreugeometrie verwendet wird [30, 32]. Typischerweise verwendet man Elektronenenergien im Bereich von 20 bis 300 eV, wobei Elektronen einer Energie von 150 eV eine de Broglie Wellenlänge von 1 Å aufweisen. Das Streubild wird mit einem Fluoreszenzschirm detektiert und erlaubt eine einfache Bestimmung des Rekonstruktionstyps. Im Gegensatz zu SXR D Messungen sind LEED Experimente nur im UHV und nur an leitfähigen Proben möglich. Ein Vorteil dieser Methode ist die intrinsische Oberflächensensitivität, da die Elektronen aufgrund ihrer starken Wechselwirkung mit Materie nur wenige Atomlagen in die Probenoberfläche eindringen.

Experimentelles

Alle Experimente wurden mit mechanisch und elektrochemisch polierten Ag(111) Einkristallen durchgeführt, die einen Miscut von $\pm 0,1^\circ$ gegenüber der (111) Ebene aufweisen. Vor den Experimenten wurden die Silberkristalle mit Hilfe von Sputter-Heiz-Zyklen gereinigt und die Sauberkeit der Probe wurde mit Auger Elektronen Spektroskopie oder XPS verifiziert.

Die in-situ SXR D Experimente wurden an der MPI-MF Beamline des Synchrotron ANKA (Angströmquelle Karlsruhe) bei einer Photonenenergie von 10,5 keV durchgeführt [37]. Während der Messungen befand sich die Ag(111) Probe in einer mobilen in-situ Oxidationskammer, die mit einem 2 mm starken, freistehenden Berylliumfenster ausgerüstet ist. Die Kammer ist mit einer Probenheizung ausgestattet, die Experimente in einem Temperaturbereich von 300 bis ca. 1000 K ermöglicht. Die Temperaturmessung erfolgt mit einem Thermoelement, das an der Seite der Probe fixiert ist, wobei die Temperatur auf ± 5 K bestimmt werden kann. Der Sauerstoffdruck kann vom UHV (niedriger 10^{-10} mbar Bereich) bis zu 2 bar eingestellt werden. Die ganze Kammer wird auf dem Diffraktometer montiert, welches im Z-Achsen-Modus betrieben wurde.

Das Diffraktometer besitzt 6 Freiheitsgrade (Kreise), wobei 3 dazu verwendet werden die Probe bezüglich des einfallenden Strahls zu justieren. 2 Kreise werden für die Bewegung des Detektors benötigt und ein Kreis rotiert die Probe um die Oberflächennormale, um die jeweilige Streuebene richtig zum einfallenden Strahl auszurichten. Nach erfolgter Justierung der Probe können Scans im reziproken Raum durchgeführt werden.

Die HRCLS Experimente wurden an Beamline I311 des Synchrotrons MAX II im MAX-lab in Lund durchgeführt [38]. Die Photonenenergie kann mit Hilfe eines Gittermonochromators von 30 bis 1500 eV variiert werden. Die Messungen wurden in einer UHV Kammer durchgeführt, die mit einem hochauflösenden hemisphärischen Elektronenenergieanalysator [39] ausgerüstet ist, in der ein Basisdruck von 10^{-11} mbar erreicht werden kann. Oberhalb der Messkammer befindet sich eine zweite UHV Kammer, in der die Ag(111) Oberfläche präpariert und oxidiert wurde. Des Weiteren ist die Präparationskammer mit einem LEED System ausgestattet. Die Probe wird mit einem Wolframdraht fixiert und ist an der Seite mit einem Thermoelement verbunden. Die Heizung der Probe erfolgt resistiv über den Wolframdraht, welcher mit einem Kupferblock verbunden ist, der mit flüssigem Stickstoff gekühlt wird. Dieser Aufbau erlaubt HRCLS Messungen bei einer Temperatur von ~ 100 K.

Die NIXSW Messungen wurden an Beamline ID32 des Synchrotrons ESRF (European Synchrotron Radiation Facility) bei einer Photonenenergie von ca. 2,6 keV durchgeführt [40]. Die UHV Kammer ist mit einer Sputterkanone und einem LEED System ausgerüstet. Der Probenhalter ist über ein Kupfergeflecht mit einem Kryostat verbunden. Dies ermöglicht Messungen bei einer Temperatur von ~ 120 K. Die Probenheizung erfolgt über ein Filament, wobei die Temperatur über ein Thermoelement ausgelesen wird, welches sich an der Seite der Silberprobe befindet. Während der Messungen ist die Messkammer fensterlos mit dem Speicherringvakuum verbunden, um starke Verluste aufgrund von Luftstreuung zu vermeiden. Die Photoelektronen werden mit einem hemisphärischen Elektronenenergieanalysator detektiert und die zurückgestreuten Photonen mit einer Photodiode.

Ergebnisse

Die saubere Ag(111) Oberfläche

Die Relaxation der sauberen Ag(111) Oberfläche wurde durch die Messung von fünf unabhängigen CTRs bei Raumtemperatur bestimmt. Der Fit an unsere Daten ergibt eine Kompression des ersten Silberlagenabstands um 1,23 % und eine Kontraktion von 1,17 % für den zweiten Silberlagenabstand. Die Resultate sind in Abbildung 2 zusammengefasst. Die Simulation der CTRs zeigt eine gute Übereinstimmung mit unseren Daten, was sich in einem χ^2 von 1,20 widerspiegelt, wobei χ^2 ein Gütefaktor für die Übereinstimmung von Messung und Berechnung ist. Eine optimale Anpassung würde ein χ^2 von 1 ergeben. Die Debye-Waller Faktoren B_i , die ein Maß für die

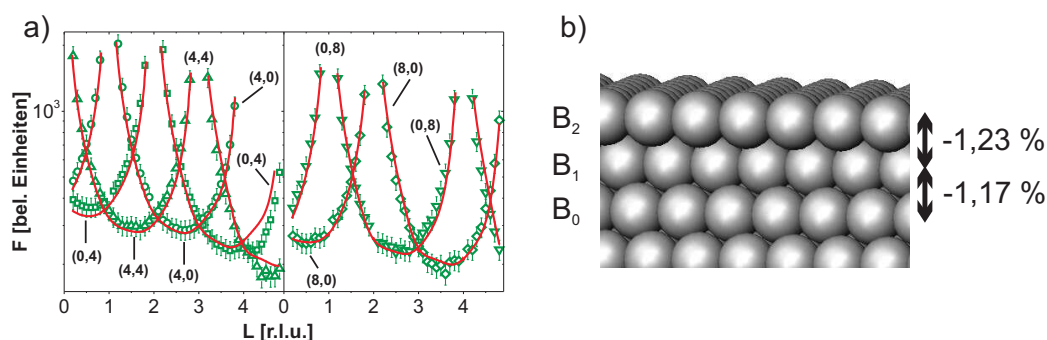


Abbildung 2: a) CTRs der sauberen Ag(111) Oberfläche mit dem entsprechenden Fit, dargestellt in reziproken Gittereinheiten (r.l.u.) der hexagonalen Oberflächeneinheit-zelle. b) Relaxation der Ag(111) Oberfläche und Definition der Debye-Waller Faktoren.

Schwingungsamplitude der Atome sind, wurden ebenfalls ermittelt. Der Debye-Waller Faktor der ersten Lage B₂ weist einen Wert von $1,62 \text{ \AA}^2$, für die zweite Lage ergibt sich $B_1 = 1,10 \text{ \AA}^2$ und die dritte Lage nimmt bereits den Bulkwert von $0,8 \text{ \AA}^2$ an. Dies bedeutet, dass die Schwingungsamplitude der Atome der obersten Atomlagen stark vergrößert ist, was ein erwartetes Verhalten für Silber ist, da es eine niedrige Debyetemperatur aufweist. Des Weiteren stehen unsere Ergebnisse in Einklang mit einer LEED-I(V) Studie [41].

Ungeordnet chemisorbierter Sauerstoff

Die Oxidation der Ag(111) Oberfläche bei niedrigem Sauerstoffdruck führt zunächst zur ungeordnet, dissoziativen Chemisorption von Sauerstoff bevor sich geordnete Überstrukturen ausbilden. Die teilweise negative Ladung der adsorbierten Sauerstoffatome führt zu einer abstoßenden Wechselwirkung zwischen den einzelnen Sauerstoffatomen, was bereits in STM Messungen beobachtet wurde [42]. Im Rahmen dieser Arbeit wurde die mittlere Höhe der Sauerstoffatome oberhalb der ersten Silberlage mittels NIXSW Messungen bestimmt. Als Resultat ergibt sich eine kohärente Position P von 0,67, was einer mittleren Höhe von $1,57 \text{ \AA}$ entspricht. Die kohärente Fraktion F weist einen relativ niedrigen Wert von 0,43 auf. Dies deutet auf eine breite Höhenverteilung hin, die durch die repulsive Wechselwirkung der Sauerstoffatome verursacht wird, was zu vielen Möglichkeiten der lokalen Bindungsgeometrie führt. Aus einer χ^2 -Analyse des Standing Wave Profils ergibt sich insgesamt für die Höhe der chemisorbierten Sauerstoffatome $1.47 \pm 0.3 \text{ \AA}$. Dieses Resultat ist mit einer Adsorption der Sauerstoffatome an dreifach koordinierten fcc Plätzen auf der Oberfläche in Einklang, wie es von mehreren DFT Studien vorhergesagt wurde [16, 43, 44]. Mit Hilfe von SXRD Messungen konnten wir nachweisen, dass die ungeordnete Chemisorption zu

zufälligen Verschiebungen der Silberatome der obersten Atomlage in der Größe von $0,12 \text{ \AA}$ führt. Dieses Ergebnis stimmt ebenfalls mit einer DFT Studie überein [43].

Die $p(4 \times 4)$ Rekonstruktion: Kein Oberflächenoxid

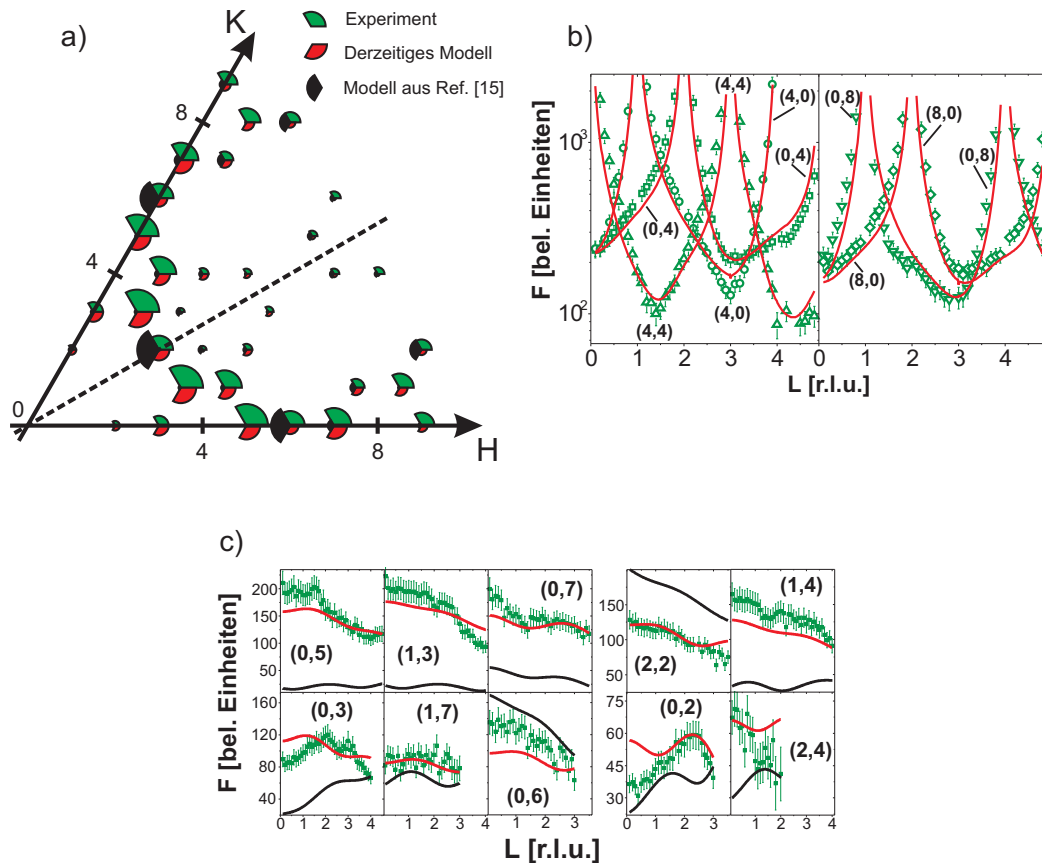


Abbildung 3: Experimentelle und berechnete Strukturfaktoren. a) In-plane Strukturfaktoren für $L = 0, 2$, b) CTRs und c) Oberflächenrods der $p(4 \times 4)$ Rekonstruktion. Die q -Werte sind in reziproken Gittereinheiten (r.l.u.) der (4×4) Zelle angegeben.

Bei Temperaturen über 420 K wandelt sich ungeordnet chemisorbierter Sauerstoff bei Erhöhung des Sauerstoffdrucks in die $p(4 \times 4)$ Rekonstruktion um [14]. Die Struktur der Rekonstruktion schien durch eine Kombination von STM Messungen und STM Simulationen und anschließenden DFT Rechnungen gelöst [15, 16]. Es wurde ein dreilagiges Oberflächenoxidmodell mit einer Ag_{11}O_6 Stöchiometrie vorgeschlagen, welches auf einer dreilagigen Schicht des Bulkoxids Ag_2O in (111) Orientierung beruht. Im Rahmen unserer SXR D Messungen konnten wir zeigen, dass dieses Strukturmodell inkompatibel mit unserem Datensatz ist. Ein Vergleich des Ag_{11}O_6 Modells

mit unseren Messergebnissen ist in Abbildung 3 a) und c) gezeigt. Ein neues Strukturmodell wurde durch eine Kollaboration bestimmt, dabei wurde eine Kombination von SXR, STM und HRCLS Messungen und DFT Berechnungen angewendet [19]. Das neue Modell der $p(4 \times 4)$ Rekonstruktion, das eine Ag_{12}O_6 Stöchiometrie aufweist, ist in Abbildung 4 c) gezeigt. Für den simultanen Fit an unseren kompletten SXR Datensatz, haben wir $p6mm$ Symmetrie verwendet, die unsere in-plane Strukturfaktoren aufweisen. Es ergibt sich eine gute Übereinstimmung zwischen Messung und simulierten Strukturfaktoren, die sich in einem χ^2 von 3,7 widerspiegelt. Die Fitergebnisse sind in Abbildung 3 dargestellt. Das Ag_{12}O_6 Modell besteht aus zwei adsorbierten Ag_6 Dreiecken, wobei sich ein Dreieck auf fcc Plätzen befindet und das andere auf hcp Plätzen. Der Ag-Ag Abstand innerhalb der Dreiecke ist nur minimal gegenüber den Bulkwerten vergrößert. Zwei Silberdreiecke sind immer durch zwei Sauerstoffatome miteinander verbunden. Dies ergibt insgesamt 6 Sauerstoffatome pro (4×4) Zelle, was einer Bedeckung von 0,375 Monolagen (ML) entspricht. Ein typisches Merkmal dieses Modells sind 'Löcher' am Ursprung der Einheitszelle, die auch in STM Messungen beobachtet wurden [15, 19, 20]. Des Weiteren zeigt diese Struktur eine sehr gute Übereinstimmung mit unseren HRCLS und NIXSW Messungen. Insgesamt handelt es sich also bei diesem Modell der $p(4 \times 4)$ Rekonstruktion um eine nanostrukturierte Adsorbatschicht, die keine Ähnlichkeit mit dem Bulkoxid Ag_2O aufweist.

Eine Vielzahl sauerstoffinduzierter Strukturen auf Ag(111)

Im Rahmen unserer SXR Und LEED Messungen wurden neben der $p(4 \times 4)$ Rekonstruktion noch fünf weitere sauerstoffinduzierte Strukturen beobachtet, die im Folgenden diskutiert werden. Alle beobachteten Strukturen wiesen unter bestimmten Bedingungen eine Koexistenz mit der $p(4 \times 4)$ Rekonstruktion auf. Eine Übersicht über die von uns vorgeschlagenen Strukturmodelle ist in Abbildung 4 gegeben.

Eine sauerstoffinduzierte Modulation der ersten Silberlage entlang der (110) Richtung, die eine Wellenlänge von 10,32 Å aufweist, wurde während unserer SXR Messungen für Temperaturen zwischen 473 und 503 K und einem Sauerstoffdruck von 5 bis 100 mbar beobachtet. Die inkommensurable Modulation wird höchstwahrscheinlich durch Streifen chemisorbierten Sauerstoffs verursacht. In Abbildung 4 a) ist die Struktur, die eine Sauerstoffbedeckung von 0,28 ML aufweist, dargestellt. In dieser Phase dominiert die repulsive O-O Wechselwirkung über die attraktive O-Ag Wechselwirkung. Aus diesem Grund beobachtet man die Inkommensurabilität entlang der (110) Richtung, wobei die abstoßende Wechselwirkung durch die Streifenbildung minimiert wird.

Im Rahmen unserer LEED Messungen wurde eine $(\sqrt{3} \times 2, 28)\text{rect}$ $R30^\circ$ Rekonstruktion nachgewiesen, nachdem die Ag(111) Oberfläche bei 430 K und 5 bis 10 mbar O_2 oxidiert wurde. Diese Struktur weist ebenfalls eine Inkommensurabilität entlang der (110) Richtung auf. Das vorgeschlagene Strukturmodell, welches in Abbildung 4 b) dargestellt ist, ähnelt dem der modulierten Struktur, wobei in diesem Fall die Streifen

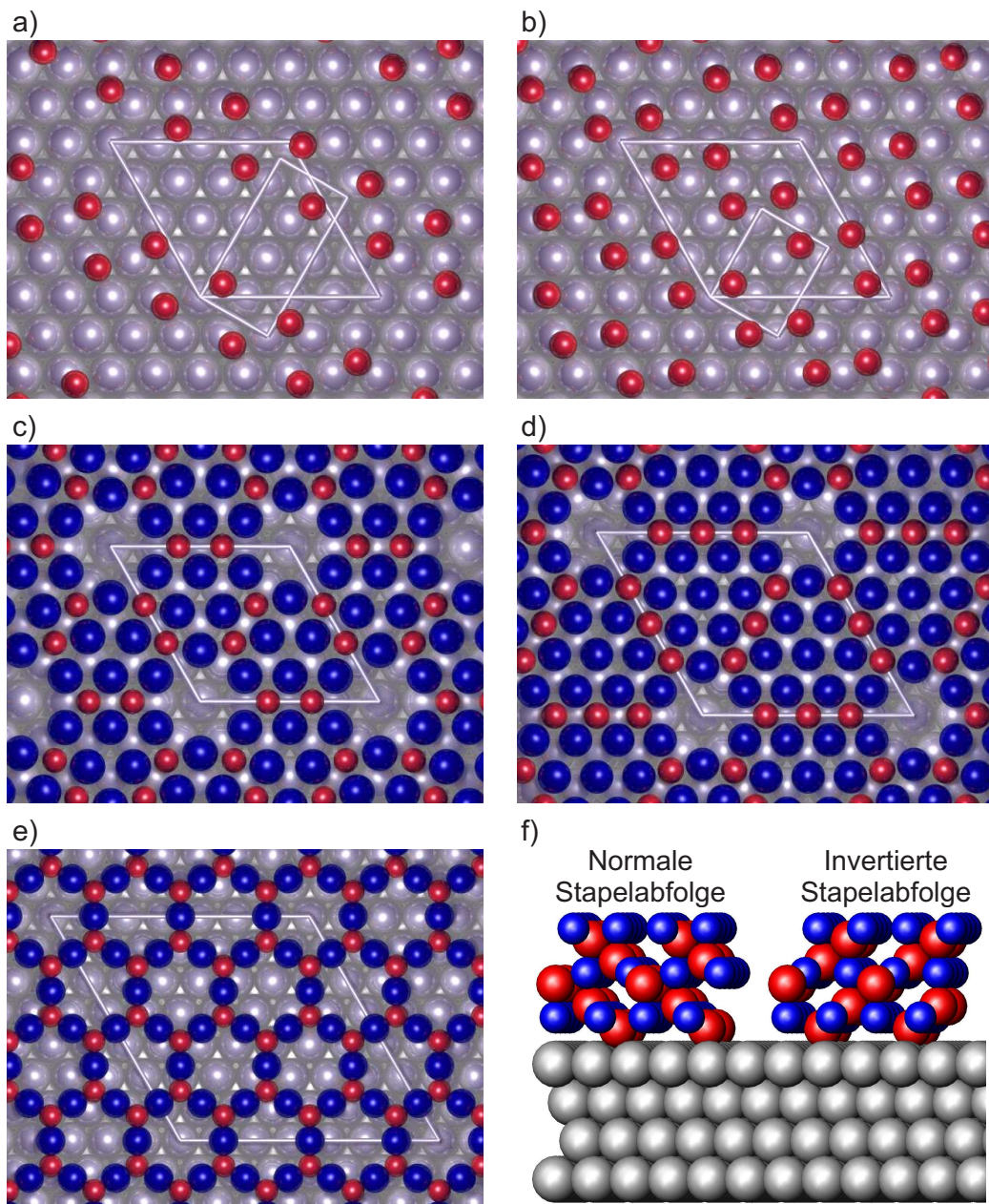


Abbildung 4: Strukturmodelle aller sauerstoffinduzierter Strukturen, die von uns beobachtet wurden. Blaue Kugeln stellen Silberatome dar und rote Kugeln Sauerstoffatome. a) Modulation entlang (110) b) $(\sqrt{3} \times 2, 28)_{\text{rect}} R30^\circ$ Rekonstruktion c) $p(4 \times 4)$ Struktur d) $p(5 \times 5)$ Überstruktur e) $p(7 \times 7)$ Koinzidenzstruktur f) $\text{Ag}_2\text{O}(111)$ und $\text{Ag}_2\text{O}(\bar{1}\bar{1}\bar{1})$.

chemisorbierten Sauerstoffs einen Abstand von $6,59 \text{ \AA}$ aufweisen. Es ergibt sich eine Sauerstoffbedeckung von $0,44 \text{ ML}$, die die höchste aller beobachteten Strukturen ist. Die $(\sqrt{3} \times 2, 28)\text{rect R}30^\circ$ Rekonstruktion ist aufgrund der stark abstoßenden O-O Wechselwirkung nur metastabil und wurde nur für relativ niedrige Temperaturen von ca. 430 K beobachtet.

Die Oxidation der Ag(111) Oberfläche bei einer Temperatur von 423 bis 453 K und atmosphärischem Sauerstoffdruck führt zu einer $p(5 \times 5)$ Rekonstruktion. Das Strukturmodell basiert auf dem Ag_{12}O_6 Modell der $p(4 \times 4)$ Rekonstruktion und ist in Abbildung 4 d) gezeigt. Die $p(5 \times 5)$ Rekonstruktion lässt sich durch zwei Ag_{10} Dreiecke pro Einheitszelle erklären, wobei sich ein Dreieck auf fcc Plätzen befindet und das andere Dreieck auf hcp Plätzen. Zwei Dreiecke sind immer durch drei Sauerstoffatome verbunden. Dies führt zu einer Ag_{20}O_9 Stöchiometrie und einer Sauerstoffbedeckung von $0,36 \text{ ML}$. Die Ausbildung adsorbierter Silberdreiecke scheint ein 'Baustein' zu sein, der sich auch in der $c(3 \times 5\sqrt{3})\text{rect}$ Rekonstruktion wiederfindet, die im Rahmen einer STM Studie beobachtet wurde [20].

Des Weiteren konnten wir eine Koexistenz der $p(4 \times 4)$ Rekonstruktion, einer $p(7 \times 7)$ Koinzidenzstruktur und des Bulkoxids Ag_2O in $(\bar{1}\bar{1}\bar{1})$ Orientierung bei 523 K und atmosphärischem Sauerstoffdruck beobachten, wenn die Probe von 773 K und 1 bar O_2 abgekühlt wurde [21]. Das Bulkoxid wächst in Inseln mit einer Höhe von $\sim 50 \text{ \AA}$ auf und weist im Vergleich zum Substrat eine invertierte Stapelabfolge auf (siehe Abbildung 4 f)). Die Struktur der $p(7 \times 7)$ Rekonstruktion lässt sich mit einem dreilagigen O-Ag-O Oberflächenoxidmodell auf Basis von Ag_2O erklären, welches dieselbe Orientierung wie das Bulkoxid aufweist. Das Modell ist in Abbildung 4 e) dargestellt. Die $p(7 \times 7)$ Struktur wäre somit die erste Beobachtung eines Oberflächenoxids auf der Ag(111) Oberfläche. Außerdem schlagen wir vor, dass das Bulkoxid einen Stranski-Krastanow Wachstumsmodus aufweist [45], wobei die Bulkoxidinseln auf der ultradünnen Oberflächenoxidschicht aufwachsen.

Das Stabilitätsdiagramm des O/Ag(111)-Systems

Durch unsere in-situ SXR D Messungen des Stabilitätsdiagramms des O/Ag(111)-Systems, welches in Abbildung 5 gezeigt ist, haben wir das sogenannte 'pressure gap' geschlossen, welches die Diskrepanz zwischen ex-situ UHV Untersuchungen und den Bedingungen der katalytischen Reaktionen beschreibt. Das theoretisch berechnete Phasendiagramm [16, 22] steht in Einklang mit unseren Messergebnissen, wobei aufgrund von Ungenauigkeiten der Berechnungen im theoretischen Phasendiagramm die Temperatur um 110 K unterschätzt wird und der O_2 Druck um drei Größenordnungen zu hoch ist [22]. Bis 503 K spielen kinetische Effekte eine wichtige Rolle, was die relativ großen Abweichungen zwischen Theorie und Messung in diesem Bereich erklärt. Oberhalb von 523 K sind ungeordnet chemisorbierter Sauerstoff und die $p(4 \times 4)$ Rekonstruktion im thermodynamischen Gleichgewicht mit der umgebenden Gasphase, was sich in einer instantanen Bildung oder Zersetzung der Strukturen widerspiegelt,

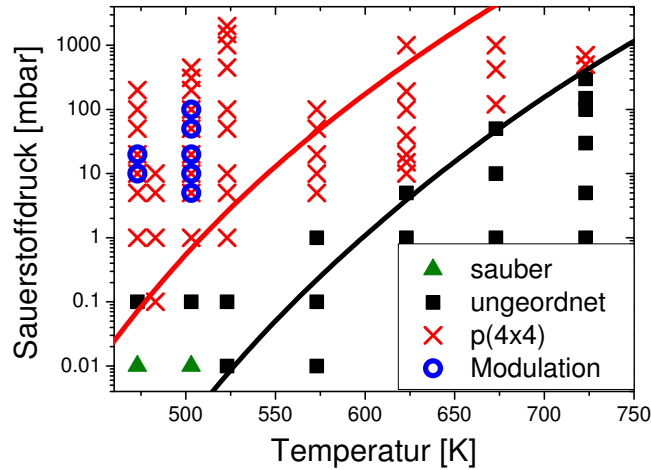


Abbildung 5: Stabilitätsdiagramm des O/Ag(111)-System, bestimmt durch in-situ SXR. Die schwarze Linie markiert die berechnete Phasengrenze von $1/16$ ML chemisorbiertem Sauerstoff [22]. Die rote Linie stellt die berechnete Phasengrenze des Ag_{12}O_6 Modells dar, wobei die van der Waals Wechselwirkung berücksichtigt wurde [19].

wenn man die Phasengrenzen passiert. Bis zu einer Temperatur von 503 K wurde die modulierte Struktur beobachtet, wobei sie sich mit steigendem Sauerstoffdruck in die $p(4 \times 4)$ Rekonstruktion umwandelt. Die Modulation entlang der (110) Richtung scheint eine metastabile Struktur zu sein, die bis zu einer Temperatur von 503 K 'eingefroren' ist und sich bei höheren Temperaturen sofort in die $p(4 \times 4)$ Rekonstruktion umwandelt. Die modulierte Struktur, die $(\sqrt{3} \times 2, 28)\text{rect R}30^\circ$ Rekonstruktion und die $p(5 \times 5)$ Struktur scheinen keine Bedeutung für die Epoxidation von Ethylen zu haben, da sie nicht unter den Bedingungen der katalytischen Reaktionen (500-600 K und atmosphärischer Sauerstoffdruck) beobachtet wurden. Ein wichtiges Ergebnis unserer Messungen ist, dass die $p(4 \times 4)$ Rekonstruktion unter den katalytischen Bedingungen der Epoxidation von Ethylen stabil ist (523 K und 2 bar O_2). Es wird aber noch kontrovers diskutiert, ob die $p(4 \times 4)$ Struktur in Mischungen von Ethylen und Sauerstoff stabil ist [46]. Abschließend sei noch angemerkt, dass nicht nur die $p(4 \times 4)$ Rekonstruktion sondern auch energetisch entartete Strukturen wie $\text{Ag}_2\text{O}(\bar{1}\bar{1}\bar{1})$ und das $p(7 \times 7)$ Oberflächenoxid eine wichtige Rolle für die katalytischen Eigenschaften von Ag(111) Facetten spielen können.

Chapter 1

Introduction

The oxidation of metals plays an outstanding role in everyday life. Typical phenomena are the formation of rust on steel or oxide scales on copper, showing up as a green patina. The formation of metal oxides is not always an unwanted process. The functionality of many materials is directly related to their controlled oxidation. The most prominent examples are passivating oxide layers on stainless steel. Relevant for this thesis are industrially applied heterogeneous catalytic reactions for the synthesis of many chemical products, where gaseous reactants are in contact with the solid surface of the catalyst. Oxidation reactions are very important in this context, leading to a big need of understanding of these processes in research and development. Thereby, the active oxygen species on the surface and selectivity and poisoning of the catalyst have to be studied on an atomic scale.

The high temperature and high pressure oxidation of the 4d transition metals Ru, Rh, Pd and Ag is a matter of particular interest, because these metals are widely used as oxidation catalysts [1]. On Ruthenium one observes the formation of RuO₂(110) bulk oxide islands at elevated temperatures and oxygen pressure [2]. In the case of the Pd(100) and Rh(111) surface oxidation can lead to the formation of so-called surface oxides [3,4]. These oxides are structurally related to the bulk oxide of the respective element. Furthermore, surface oxides are ultra thin oxides containing one metallic layer surrounded by two oxygen layers, giving rise to an oxygen-metal-oxygen sequence perpendicular to the surface plane.

A future vision is to get a direct microscopic control of the emerging surface structures and ultimately of the real-time oxidation/reduction dynamics allowing one to tailor such catalytic reactions to better performance. A necessary prerequisite to the microscopic control is the full atomistic understanding of the surface structures which form at high temperature and at high oxygen pressures.

Silver plays a unique role in heterogeneous catalysis. Supported Ag catalysts are used for the selective oxidation ('epoxidation') of ethylene and for the partial oxidation of methanol to formaldehyde. Ethylene oxide and its derivatives are basic chemicals for industry, used in a many technologies with a world-wide production of more than 10

million tons as in medicine for disinfection, sterilization, or fumigation, or in transport and energy technologies for engine antifreeze and heat transfer. Because of its ability to kill most bacteria, formaldehyde is extensively used as disinfectant and as preservative in vaccinations. Therefore, the optimisation of these two Ag-supported catalytic reactions is of paramount importance. Current strategies employed in the industrial process to enhance selectivity include the empirical use of inhibitors (CI) [5] and promoters (Cs) [6,7], however, on the way to a knowledge-based control of these reactions one has first to understand the surface structure of oxidized silver under relevant conditions in full detail.

The formation of extended Ag(111) facets is observed on polycrystalline silver during the above industrial catalytic oxidation reactions [8], in turn fundamental research (experiment and theory) has been devoted to the detailed understanding of oxidation of this surface [8–21]. The formation of an oxygen induced $p(4\times 4)$ reconstruction on the Ag(111) surface is known since the early 70s [9, 10]. A surface oxide trilayer model, based on a three-layer slab of $\text{Ag}_2\text{O}(111)$, was proposed [15, 16]. Accordingly, the Ag(111) surface seemed to show a similar behaviour like Pd and Rh, being neighbours in the periodic table. Further theoretical calculations predicted the stability of this reconstruction under industrially relevant conditions [16, 22].

Nevertheless, several questions remained unsolved: the stability of the $p(4\times 4)$ reconstruction under industrially relevant conditions was not checked experimentally, the structural model of the $p(4\times 4)$ structure was not proven by a crystallographic method and previously unknown structures might play an important role for the catalytic activity of Ag(111) facets. Our experimental approach is based on the nowadays routinely available highly brilliant x-ray radiation produced by third generation synchrotron light sources. This radiation is used by us in three surface sensitive x-ray techniques. In-situ surface x-ray diffraction (SXR) allows the identification and determination of structural models of surface reconstructions under industrially relevant conditions. This technique is combined with high resolution core level spectroscopy (HRCLS) and normal incidence x-ray standing wave absorption (NIXSW), giving insight into the local binding geometry of the oxygen and silver atoms.

Outline of the Thesis

In chapter 2 all results, concerning the oxidation of Ag(111), which are relevant for this thesis, are summarised. The theoretical background of the experimental techniques is explained in chapter 3. The sample treatment and the experimental setup are described in chapter 4. Chapter 5 deals with the structure and stability of the $p(4\times 4)$ reconstruction. The formation of oxygen induced structures, which were observed besides the $p(4\times 4)$ structure, is described in chapter 6. Chapter 7 gives a summary of all results and an outlook.

Chapter 2

Interaction of Oxygen with Ag(111) Surfaces

In the last decades, many studies on the oxidation of Ag(111) surfaces were performed. The results, which are relevant for this thesis, are summarised in the following sections.

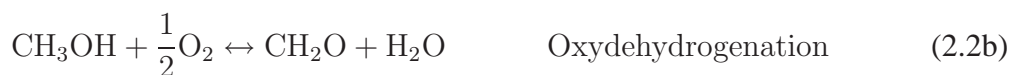
2.1 Silver and Ag₂O

Silver is a noble metal, crystallising in the fcc structure (cf. section A.1), showing a lattice constant of 4.0853 Å and a melting temperature of 1234.93 K [47]. Silver shows the highest thermal and electrical conductivity of all elements.

Silver is used as heterogeneous catalyst in two different oxidation reactions, which are applied industrially to produce ethylene epoxide and formaldehyde. These oxidation reactions are carried out at temperatures from 500 to 900 K and atmospheric oxygen pressure [8, 13]. The formaldehyde production, which is also called the 'BASF process', and the production of ethylene epoxide are of major interest, since both compounds act as basic materials in chemical industry to produce a variety of substances [8, 13]. The epoxidation of ethylene takes place at 500 to 600 K and atmospheric oxygen pressure and is described by the following reaction



The partial oxidation of methanol formaldehyde is described by two possible reactions which are carried out at a temperature of 800 to 900 K and atmospheric oxygen pressure



A detailed description of a reactor layout and the peculiarities of the BASF process can be found in [13].

The most stable silver oxide is Ag_2O . The unit cell is shown in figure 2.1 a). Ag_2O crystallises in the cuprite structure, showing a lattice constant of 4.72 \AA . Ag is transformed to Ag_2O by incorporation of oxygen atoms on one quarter of the tetrahedral sites. The transformation is accompanied by an expansion of the fcc lattice by 15.5 %.

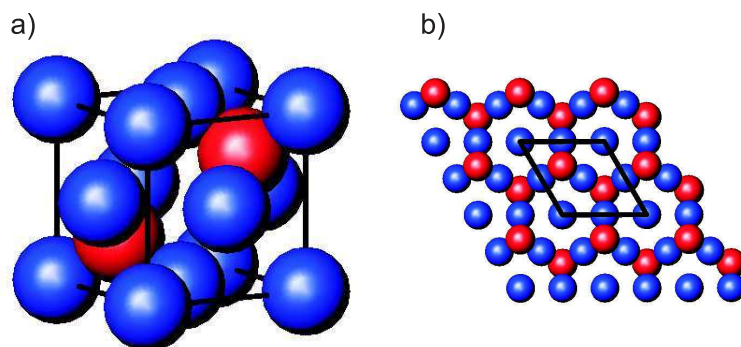


Figure 2.1: a) Cuprite structure of Ag_2O . Blue coloured smaller atoms are silver atoms. b) Three layer slab of $\text{Ag}_2\text{O}(111)$.

In (111) orientation Ag_2O can be described by a hexagonal unit cell with lattice constants $a = b = 6.675 \text{ \AA}$ and $c = 8.175 \text{ \AA}$. Along the c -axis oxygen and silver layers are alternating. A three layer slab of $\text{Ag}_2\text{O}(111)$ is shown in figure 2.1 b). Once formed Ag_2O is not stable in air. At atmospheric oxygen pressure Ag_2O decomposes at 503 K [13]. Correspondingly, tarnished silver is not caused by the presence of Ag_2O , but Ag_2S is the reason for this observation. The atmospheric corrosion occurs mainly due to reactions with H_2S [48].

2.2 Oxidation of Ag(111) Surfaces

In industrial applications, silver particles supported on Al_2O_3 are used for the catalytic reactions [6]. Important questions are, why is a noble metal catalytically active [17] and which facets of the nano particles are mostly present? A scanning electron microscopy image of Al_2O_3 supported silver nano particles is shown in figure 2.2.

The Ag(111) surface is used as model system, since it is known [8], that polycrystalline silver forms mainly (111) facets, which have the lowest surface energy, if the catalytic conditions are applied. Furthermore, it is widely accepted, that chemisorbed oxygen is responsible for the catalytic activity of silver. The bonding of chemisorbed oxygen to the Ag surfaces is not very strong, since silver is a noble metal. It is assumed, that the chemisorbed oxygen atoms act as a reservoir of atomic oxygen for the chemical reactions.

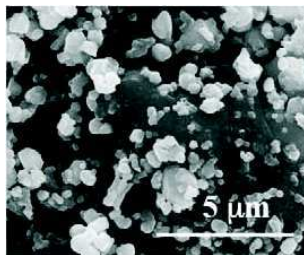


Figure 2.2: Scanning electron microscopy image of Al_2O_3 supported silver nano particles. From [6].

It is still under debate, which oxygen species is responsible for the catalytic activity of Ag(111) facets. In the following sections, the main results obtained for the oxygen induced $p(4\times 4)$ reconstruction of the Ag(111) surface, adsorption of disordered oxygen and the bulk oxide Ag_2O are summarised. (An explanation of the classification scheme of surface reconstructions is given in sections 3.1.1 and A.2.) The $p(4\times 4)$ reconstruction of the silver surface could be responsible for the catalytic activity, as will be shown in section 2.2.5.

2.2.1 Results from LEED and TPD

The oxygen induced $p(4\times 4)$ reconstruction of the Ag(111) surface (O- $p(4\times 4)$ -Ag(111)) was observed for the first time in the 70ies by low energy electron diffraction (LEED) measurements [9, 10]. The Ag(111) surface was oxidized with molecular oxygen. In a pressure range from 10^{-3} to 10 torr and temperatures between 373 and 523 K the formation of O- $p(4\times 4)$ -Ag(111) was observed. The presence of the $p(4\times 4)$ reconstruction was monitored by ex-situ LEED measurements under UHV conditions. Temperature programmed desorption (TPD) measurements of the oxidized Ag surface show an oxygen peak at 553 K, which is an indication, that oxygen atoms are involved in the structure of the $p(4\times 4)$ reconstruction. Furthermore, it was shown, that the $p(4\times 4)$ structure is stable under UHV conditions.

It was realised, that the diagonal of the hexagonal $\text{Ag}_2\text{O}(111)$ unit cell fits almost perfectly on 4 substrate unit cells. The lattice mismatch is only $\sim 0.1\%$. Correspondingly, a structural model was proposed, consisting of a Ag-O-Ag three layer slab of $\text{Ag}_2\text{O}(111)$, rotated by thirty degree with respect to the substrate unit cell, showing an epitaxial relationship to the substrate [10].

In 1985 a similar model was proposed on the basis of a combined LEED, TPD and x-ray photoelectron spectroscopy (XPS) study [11], consisting of an O-Ag-O three layer slab of $\text{Ag}_2\text{O}(111)$ rotated by 30° , which is shown in figure 2.1 b). A characteristic feature of this structure are linear O-Ag-O chains, showing a Ag-O distance of 2.05 \AA . The oxygen coverage of this structure is 0.375 monolayers (ML), which is in

agreement with the value of 0.41 ML determined by means of TPD [11].

A five times higher oxygen desorption in TPD was observed after oxidizing the Ag(111) sample at 443 K and 1400 Torr O_2 for 640 seconds. This peak corresponds to an oxygen coverage of 2.0 MLs, which is an indication for a thin layer of Ag_2O on Ag(111) with a thickness of $\sim 14 \text{ \AA}$ [11].

2.2.2 XPS Measurements

The oxidation of the Ag(111) surface was investigated by several XPS experiments [11, 12, 14]. The main results are shown in figure 2.3.

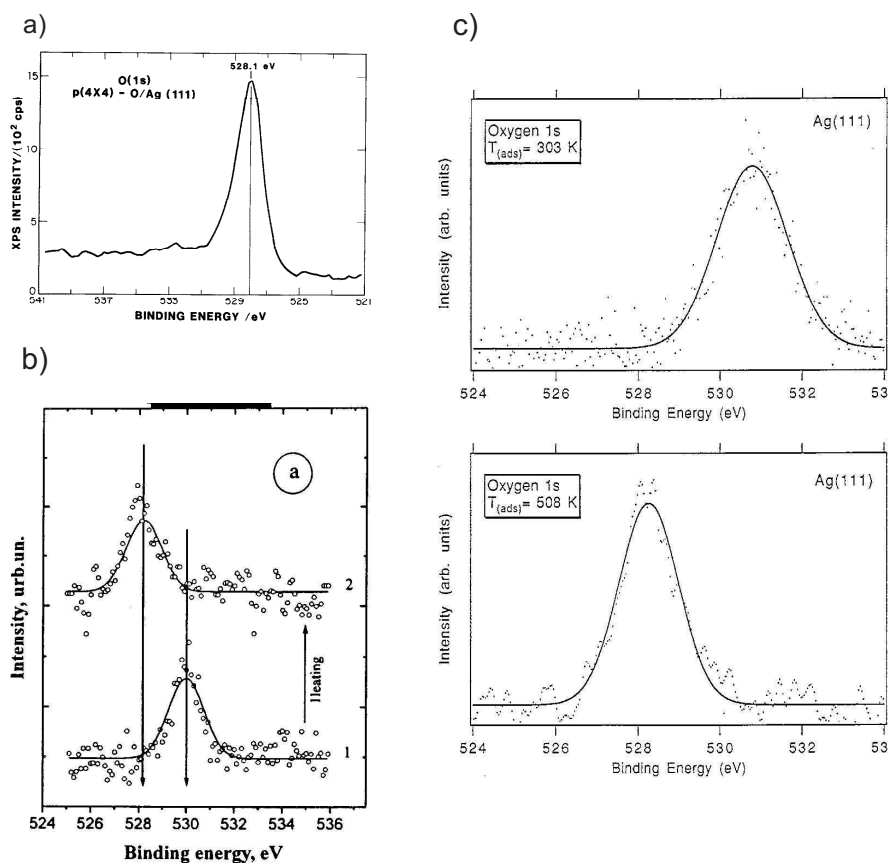


Figure 2.3: O 1s spectra of oxidized Ag(111) surfaces. a) O 1s spectrum of the p(4 \times 4) reconstruction prepared by molecular oxygen from [11], showing a peak at 528.1 eV. b) O 1s XPS spectrum of chemisorbed oxygen, showing a peak at 530 eV and O 1s spectrum of the p(4 \times 4) reconstruction showing a peak at 528.2 eV from [14]. c) O 1s spectrum of chemisorbed NO showing a peak at 530.8 eV and p(4 \times 4) reconstruction showing a peak at 528.2 eV from [12].

All O 1s spectra of the p(4×4) reconstruction show a single peak at a binding energy of ~ 528.2 eV, independent of the oxidation procedure. In reference [11] the p(4×4) reconstruction was prepared by dosing 5 torr O₂ for 20 seconds at a temperature of 490 K. In reference [14] a different procedure was applied. 1 mbar of molecular oxygen was dosed at a temperature of 300 K and in the O 1s spectrum a peak at a binding energy of 530.0 eV was observed, due to the presence of disordered chemisorbed oxygen. Upon heating the sample to 420 K the peak jumps to a binding energy of 528.2 eV, corresponding to the formation of the p(4×4) structure. In reference [12] NO₂ was used for the first time for the oxidation procedures. Dosing NO₂ at room temperature, leads to dissociative adsorption of NO, showing an O 1s peak at 530.8 eV, due to the presence of NO on the surface. A dose of only ~ 10 Langmuir (1 Langmuir = 1 L = 10^{-6} torr*s) at 508 K is enough to form the p(4×4) reconstruction, which was verified by LEED and the typical O 1s spectrum is shown in figure 2.3 c). The usage of NO₂ avoids the dosage of oxygen at high pressures, due to the low dissociative sticking coefficient of 10^{-6} for O₂ on Ag(111) surfaces [11, 12].

The O 1s spectrum of the p(4×4) reconstruction does not resemble the one of Ag₂O. The O 1s spectrum of Ag₂O shows a binding energy of 528.9 eV [49]. Furthermore, it was already mentioned in [11], that one would expect 2 peaks in the O 1s spectrum for a trilayer structure, like the O-Ag-O Ag₂O(111) model of the p(4×4) reconstruction. This topic will be discussed further in sections 5.3 and 5.4.

2.2.3 STM Measurements and DFT Calculations

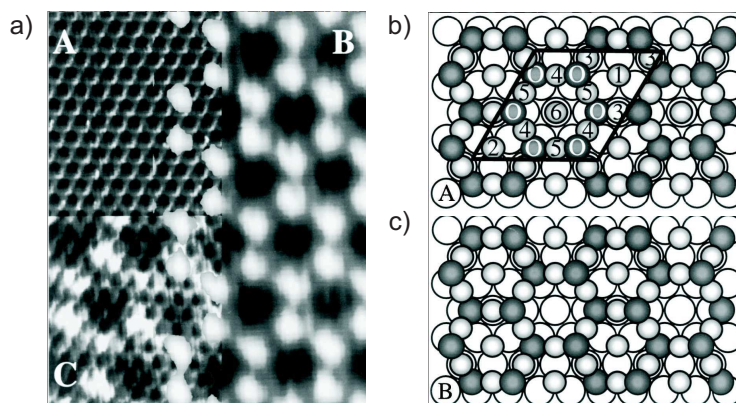


Figure 2.4: a) Scanning tunneling microscopy image of the clean Ag(111) surface. The STM images of the p(4×4) reconstruction show a honeycomb structure. b) Structural model of the p(4×4) structure from [11]. c) Silver deficient Ag_{1.83}O model proposed in [15].

The first atomically resolved scanning tunneling microscopy (STM) images of the

$p(4\times 4)$ reconstruction are shown in figure 2.4 a) [15]. The $p(4\times 4)$ structure was prepared by the NO_2 procedure proposed in [12], which was discussed in the preceding section. The STM images are shown in figure 2.4 a). The structural model was optimised by means of STM image simulations. A silver deficient surface oxide layer, showing a $\text{Ag}_{1.83}\text{O}$ (or Ag_{11}O_6) stoichiometry, was proposed and is shown in figure 2.4 c). The structure is based on the O-Ag-O trilayer model proposed in [11], shown in figure 2.4 b). The structure consists of hexagonal O-Ag-O rings, which are build up by linear O-Ag-O chains. Every third central Ag atom, situated in the middle of the O-Ag rings, was removed. The removal of these Ag atoms is motivated by their unfavourable on top position with respect to the Ag(111) substrate.

The structure of the Ag_{11}O_6 model was optimised by density functional theory (DFT) calculations [16]. An introduction to DFT is given in section B.1. It was shown, that the silver deficient model is by 0.6 eV per unit cell more favourable, than the model Ag_{12}O_6 shown in figure 2.4 b). This can be explained by the removal of the central Ag atoms located at unfavourable on top positions, as can be seen in figure 2.4 b) and c).

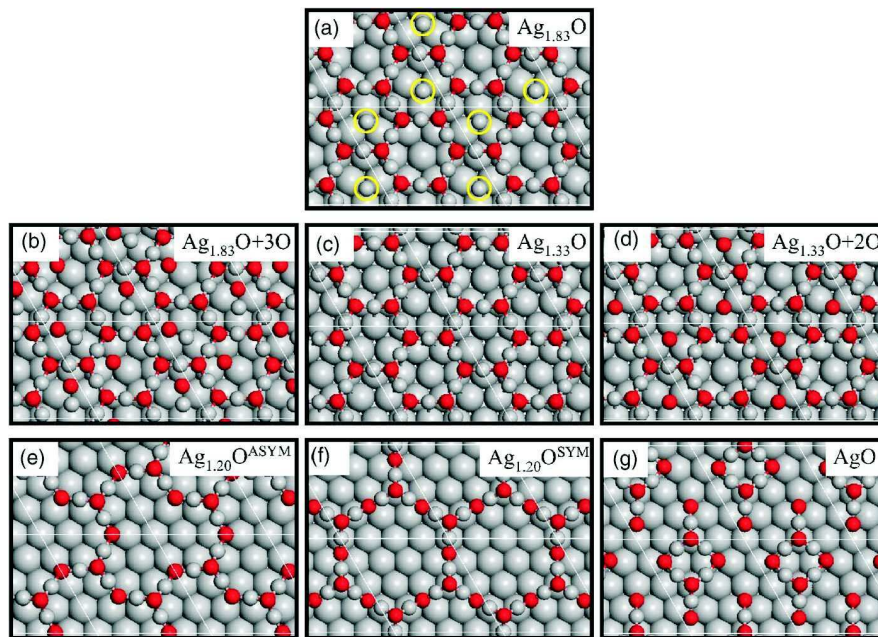


Figure 2.5: DFT optimised structural models of the $p(4\times 4)$ structure. From [18].

Further DFT calculations and STM image simulations were performed [50]. The oxidation and reduction behaviour of the Ag_{11}O_6 model was studied, resulting in several modifications of the structural model, which are also in agreement with the STM measurements shown in figure 2.4 a).

We could show by in-situ SXR D measurements, that all models of the $p(4\times 4)$ reconstruction related to a three layer slab of $\text{Ag}_2\text{O}(111)$ cannot be correct (cf. chapter

5). Furthermore, we observed a $p6mm$ symmetry of our x-ray data, giving rise to strong constraints for the construction of structural models of the $p(4\times 4)$ reconstruction.

Subsequently, further DFT calculations were performed [18], resulting in several models of the $p(4\times 4)$ structure, which are shown in figure 2.5. The most stable structure, showing $p6mm$ symmetry, is the so-called $Ag_{1.33}O$ model, which has a Ag_9O_6 stoichiometry. The Ag_9O_6 model is obtained from the $Ag_{11}O_6$ model by removing all central Ag atoms as can be seen in figure 2.5 c).

2.2.4 Disordered chemisorbed oxygen

The formation of disordered chemisorbed oxygen was observed by STM measurements, after oxidizing the Ag(111) surface at 470 K by NO_2 [42]. The results of the STM measurements are shown in figure 2.6 a). An oxygen coverage of 0.05 MLs was observed. The minimal distance between oxygen atoms was determined to be on the order of 10 \AA , due to the repulsive interaction of the partial negatively charged oxygen adatoms.

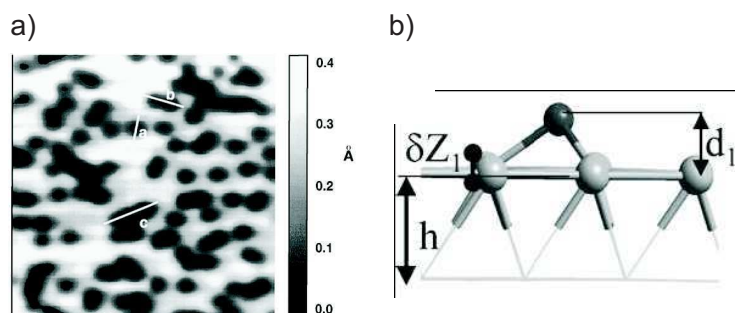


Figure 2.6: a) STM image of disordered chemisorbed oxygen. From [42]. b) DFT optimised structural model of chemisorbed oxygen at an fcc site. From [16].

The most favourable adsorption site for chemisorbed oxygen was determined by DFT calculations [16, 43, 44]. It was shown, that oxygen adsorbs at fcc sites on the surface for oxygen coverages up to 0.25 MLs, which is shown in figure 2.6 b). STM image simulations for the chemisorption of atomic oxygen atoms at fcc sites were performed [16], which are in agreement with the STM measurements from [42]. The height of the oxygen atoms above the first substrate layer was determined to be in the range of 1.21 to 1.32 \AA for a coverage of 0.25 ML [16, 43, 44].

It was predicted, that for oxygen coverages higher than 0.25 ML additional oxygen atoms occupy tetrahedral sites between the first and second substrate layer [51, 52]. The formation of subsurface oxygen becomes favourable due to the repulsive interaction of the oxygen atoms, leading to an enhanced binding energy of the oxygen atoms on the surface. The formation of onsurface and subsurface oxygen species at the same

time, can be regarded as a transient precursor state for the formation of the $p(4\times 4)$ reconstruction [51].

2.2.5 Phase Diagram of the O/Ag(111)-System

The extension of DFT calculations to finite temperatures and oxygen pressure by so-called *ab initio* thermodynamics results in a phase diagram of the O/Ag(111)-system, shown in figure 2.7 [22]. This theoretical approach is explained in section B.2.

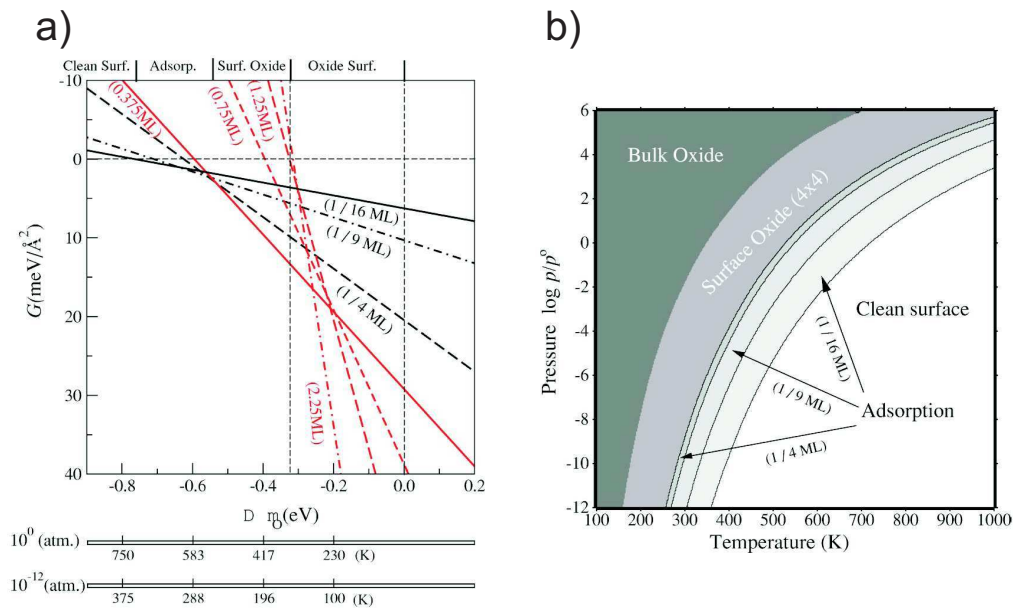


Figure 2.7: a) Phase diagram of the O/Ag(111)-system in terms of the surface free energy γ vs. oxygen chemical potential μ_{O} . From [22]. b) Same phase diagram in terms of temperature and oxygen pressure. From [22].

The surface free energy in terms of the oxygen chemical potential μ_{O} is determined from total energies calculated by DFT for all relevant oxygen induced structure. The structure showing the lowest surface free energy is thermodynamically stable. For the case of the O/Ag(111)-system four stability regions are observed, as can be seen figure 2.7 a) and b). The stability borders result from the intersections of the straight lines defining the surface free energy of the different structures. The higher the oxygen content per unit cell, the steeper the slope of the line. The stability diagram in terms of temperature and oxygen pressure can be calculated from the position of the intersections, shown in figure 2.7 a), via the ideal gas equation (cf. section B.2).

The clean silver surface is stable for low temperatures and low oxygen pressures. An increase in oxygen pressure leads to the formation of disordered chemisorbed oxy-

gen with different oxygen coverage. The $p(4\times 4)$ reconstruction is stable, if the oxygen pressure is increased further. The stability of the bulk oxide Ag_2O is predicted for low temperatures and high oxygen pressure. The error of the calculations can be estimated from the stability border of the bulk oxide at atmospheric oxygen pressure, which shows a value of 350 K. Experimentally, it is known, that Ag_2O decomposes at 460 K at atmospheric oxygen pressure. In the calculated phase diagram, the bulk oxide is not stable for pressures lower than 10^3 bar at 460 K. Correspondingly, the temperature is underestimated by 110 K and the oxygen pressure is 3 orders of magnitude too high.

The most important result is, that the Ag_{11}O_6 model is stable at temperatures of 500 to 600 K and atmospheric oxygen pressure, which are the catalytic conditions of the epoxidation of ethylene. The partial oxidation of methanol to formaldehyde takes place at 900 K and atmospheric oxygen pressure. Under these conditions it was predicted, that the clean silver surface is stable. It was suggested, that oxygen atoms bound to undercoordinated silver sites (e.g. defect and kink sites) are responsible for the catalytic activity of $\text{Ag}(111)$ surfaces.

It is important to note, that only structures, which are included in the total energy calculations, appear in the calculated phase diagram. Furthermore, kinetic effects are not included in *ab initio* thermodynamics calculations.

2.3 Motivation for our Experiments

All proposed models of the $p(4\times 4)$ reconstruction can be checked by our SXRD, HRCLS and NIXSW measurements and as the case may be a new model of the $p(4\times 4)$ reconstruction can be determined. By HRCLS the O 1s spectrum of the $p(4\times 4)$ reconstruction can be measured with higher resolution than in previous studies, allowing us to determine the number of oxygen species present in the $p(4\times 4)$ structure. By NIXSW the position of the oxygen atoms along the (111) direction can be determined.

Furthermore, the so-called 'pressure gap', which describes the discrepancy between ex-situ UHV studies and the catalytic conditions, can be closed by in-situ SXRD measurements, since all previous studies on the oxidation of $\text{Ag}(111)$ surfaces were ex-situ measurements. In-situ SXRD allows the determination of the stability diagram of the O/ $\text{Ag}(111)$ -system up to an oxygen pressure of 2 bar. The measured stability diagram can be compared with the calculated phase diagram.

Additionally, the stability and the adsorption geometry of disordered chemisorbed oxygen can be determined by means of SXRD and NIXSW measurements, which can be compared with the DFT calculations and STM measurements.

Finally, reconstructions of the $\text{Ag}(111)$ surface and the formation of the bulk oxide Ag_2O , which have not been observed before can be detected by systematic SXRD and LEED studies.

Chapter 3

Theoretical Background

The oxidation of Ag(111) surfaces was studied by three surface sensitive x-ray techniques, based on the utilisation of highly brilliant synchrotron radiation: **S**urface **X**-**R**ay **D**iffraction (SXRD), **H**igh **R**esolution **C**ore **L**evel **S**pectroscopy (HRCLS) and **N**ormal **I**ncidence **X**-**R**ay **S**tanding **W**ave **A**bsorption (NIXSW). In addition, **L**ow **E**nergy **E**lectron **D**iffraction (LEED) and **A**uger **E**lectron **S**pectroscopy (AES) were applied to characterise the oxidation state of the Ag(111) surface and to monitor the cleanliness of the samples.

SXRD is a powerful tool to determine the properties of reconstructions and relaxations of single crystal surfaces on an atomic scale with sub-Å resolution. The low scattering cross section of hard x-rays allows in-situ measurements of oxidation processes under industrial relevant conditions. Furthermore, kinematical diffraction theory can be applied, for the same reason, to calculate scattered intensity distributions for a given surface structure. This allows a straightforward determination of structural models of oxidized silver surfaces.

HRCLS as a spectroscopic method is well-suited to determine the oxidation state, chemical surrounding and the number of different species of a certain element on the surface. This method is element specific and the measured photoelectron spectra can be decomposed by the use of special line shapes, including final and initial state effects. Due to the strong interaction of the emitted photoelectrons with matter, UHV conditions are a necessary prerequisite for this technique. This drawback is compensated by the high sensitivity to adsorbed oxygen atoms.

Finally, NIXSW is a combination of x-ray diffraction and core level spectroscopy. The observed effects can be described by the theory of dynamical x-ray diffraction. The position of atoms can be determined in a direction perpendicular to the used scattering planes in units of the lattice plane spacing. Due to the detection of photoelectrons this technique is also sensitive to the position of oxygen atoms. NIXSW is as HRCLS an ex-situ method, but in combination with in-situ SXRD and HRCLS measurements a deeper understanding of oxidation processes can be obtained by these complementary techniques.

LEED and AES are standard tools of surface science, which were used for the characterisation of the Ag(111) samples. The presence of different reconstructions on Ag(111) can be easily monitored by LEED. In addition, AES was used during the sample preparation to check for present contaminations on the silver surface.

In the following, the theoretical background of the experimental techniques will be explained, which is necessary to understand the results presented in this thesis.

3.1 X-Ray Diffraction

Surface x-ray diffraction is based on elastic scattering of x-rays by electrons. An introduction to the theory of x-ray diffraction can be found in references [23, 24]. In kinematical diffraction theory, which is used to describe SXRD, the effect of primary extinction of x-rays due to multiple scattering and refraction effects are neglected. These effects turn out to be crucial for the theory of dynamical diffraction by perfect crystals, presented in section 3.3.1, which is used to describe the properties of x-ray standing waves. Furthermore, inelastic processes like Compton scattering or the photo effect are not taken into account.

The wavelength λ of hard x-rays is typically $\sim 1 \text{ \AA}$, which is in the order of lattice spacings of crystals, making x-ray diffraction from crystalline objects possible. The measured diffracted intensity $I(\mathbf{q})$ equals $|A(\mathbf{q})|^2$. The scattering amplitude $A(\mathbf{q})$ is given by

$$A(\mathbf{q}) \propto r_0 \underbrace{\sum_{\mathbf{r}_j} f_j(\mathbf{q}) e^{i\mathbf{q}\cdot\mathbf{r}_j}}_{\text{unit cell structure factor}} \underbrace{\sum_{\mathbf{R}_n} e^{i\mathbf{q}\cdot\mathbf{R}_n}}_{\text{lattice sum}} \quad (3.1)$$

The $I(\mathbf{q})$ distribution is experimentally accessible, the phase information contained in the scattering amplitude cannot be measured. This is known as the *missing phase problem of crystallography*. The determination of the crystal structure relies on a trial and error procedure, using structural models to calculate $I(\mathbf{q})$ (see also section 3.1.1). Equation 3.1 is derived by use of the translational symmetry of the crystal which is given by the \mathbf{R}_n , describing the crystal lattice. Each lattice point is occupied by one unit cell. The distribution of atoms at positions \mathbf{r}_j within this cell is described by the unit cell structure factor $F(\mathbf{q})$, which is the effective electron concentration at the origin of the unit cell. The electron density distribution of the atoms is included in the atomic form factor f_j , which is derived from results obtained for scattering by a free electron. The Thomson scattering length or the classical electron radius r_0 is the ability of a free electron to scatter x-rays. The correct superposition of the scattered x-rays is included in the phase factor $e^{i\mathbf{q}\cdot\mathbf{r}}$. One important quantity is the wave vector transfer \mathbf{q} defined by the wave vectors of the incident wave \mathbf{k}_i and the scattered wave \mathbf{k}_f

$$\mathbf{q} = \mathbf{k}_f - \mathbf{k}_i \quad (3.2a)$$

$$|\mathbf{k}_f| = |\mathbf{k}_i| = \frac{2\pi}{\lambda} \quad (3.2b)$$

$$|\mathbf{q}| = 4\pi * \frac{\sin \vartheta}{\lambda} \quad (3.2c)$$

where ϑ is the scattering angle, which is also found in Bragg's law $\lambda = 2d \sin \vartheta$ [53]. The lattice sum shows maxima, given by the number of illuminated unit cells N , if the Laue condition is fulfilled [54]

$$\boxed{\mathbf{q} = \mathbf{G} \quad \text{Laue Condition}} \quad (3.3)$$

$\mathbf{G} = H\mathbf{a}_1^* + K\mathbf{a}_2^* + L\mathbf{a}_3^*$ is a reciprocal lattice vector, defined by $\mathbf{a}_i \mathbf{a}_j^* = 2\pi \delta_{ij}$. The \mathbf{a}_i are the unit cell vectors in real space. H , K and L are called Miller indices. The fulfilment of the Laue condition is a necessary condition for the observation of a Bragg peak in the direction of \mathbf{k}_f . Normally, not all points of the reciprocal lattice give rise to allowed Bragg reflections. Only, if the structure factor of the unit cell $F(\mathbf{q})$ is not vanishing for a set of (HKL) , the reflection is allowed. The selection rules for $\text{Ag}(111)$ surfaces represented in a hexagonal coordinate system are given in appendix A.1.

The theory of kinematical x-ray diffraction as described so far can be applied to the study of imperfect crystalline bulk samples. In the following section this approach will be extended to explain surface x-ray diffraction measurements.

3.1.1 Surface X-Ray Diffraction

The presence of the surface in combination with an absorption ε per atomic layer of the x-rays leads to diffuse scattered intensity profiles between all Bragg peaks in a direction perpendicular to the surface. These profiles are called *Crystal Truncation Rods* (CTR) [25]. The incomplete destructive interference between the Bragg peaks can be explained by missing lattice planes due to the presence of the surface. The technique of SXRD is reviewed in references [25–29]. Normally, the \mathbf{a}_i are chosen in such a way, that \mathbf{a}_3 and \mathbf{a}_3^* are parallel to the surface normal. The truncation of the crystal due to the presence of the surface is reflected in a change in the lattice sum, introduced in equation 3.1. The lattice sum S_{surf} of the semi-infinite crystal can be written as [24, 26, 55]

$$\boxed{S_{\text{surf}} = \sum_{n=0}^{\infty} e^{i\mathbf{a}_3^* \mathbf{a}_3 n} e^{-\varepsilon n} = \frac{1}{1 - e^{i2\pi L} e^{-\varepsilon}}} \quad (3.4)$$

The effect of ε is most pronounced at the positions of Bragg peaks, the shape of the CTR itself remains mainly unaffected [24, 28]. For typical energies of hard x-rays ε can be neglected. Consequently, the structure factor of a CTR F_{CTR} is given by

$$F_{\text{CTR}} = F_{\text{unit cell}} * S_{\text{surf}} \quad (3.5a)$$

$$F_{\text{CTR}} = \sum_{\mathbf{r}_j} f_j(\mathbf{q}) e^{i\mathbf{q}\cdot\mathbf{r}_j} * \frac{1}{1 - e^{i2\pi L}} \quad (3.5b)$$

The truncation of the crystal has only an effect on the L direction, in the surface plane the Laue condition must be fulfilled furthermore

$$\mathbf{q}_{\parallel} = \mathbf{G}_{\parallel} \quad (3.6)$$

The surface of a crystal may be either relaxed or reconstructed. In the case of a relaxation the surface shows the same in-plane periodicity as the bulk. A reconstruction changes the size of the in-plane surface unit cell. The primitive in-plane surface unit cell may be rotated with respect to the substrate lattice. The signal scattered from the surface unit cell is calculated by the structure factor F_{surf} . The amount of reconstructed surface area is included in the coverage Θ

$$F_{\text{surf}} = \Theta \sum_{\mathbf{r}_s}^{\text{surface unit cell}} f_s(\mathbf{q}) e^{i\mathbf{q}\cdot\mathbf{r}_s} \quad (3.7)$$

In any case, the structure factor on the CTRs F_{total} is given by a coherent superposition of the bulk and the surface contribution

$$F_{\text{total}} = F_{\text{CTR}} + F_{\text{surf}} \quad (3.8a)$$

$$F_{\text{total}} = \sum_{\mathbf{r}_j}^{\text{bulk unit cell}} f_j(\mathbf{q}) e^{i\mathbf{q}\cdot\mathbf{r}_j} * \frac{1}{1 - e^{i2\pi L}} + \Theta \sum_{\mathbf{r}_s}^{\text{surface unit cell}} f_s(\mathbf{q}) e^{i\mathbf{q}\cdot\mathbf{r}_s} \quad (3.8b)$$

SXRD is very sensitive to small changes of the surface structure, this is demonstrated in figure 3.1, where the effect of relaxations of a Ag(111) surface and the surface contribution for different surface terminations is shown. A contraction of the first interlayer spacing shifts the minimum of the CTR to larger values of \mathbf{q}_z , the opposite is observed for an outward relaxation of the first silver layer (see figure 3.1a)). The surface contribution of one monolayer is a constant in \mathbf{q}_z , which is only reduced in intensity due to the q-dependency of the atomic form factor $f_s(\mathbf{q})$ [23, 24, 26]. A modulation of F_{surf} is observed for the case of two monolayers, due to the interference of x-rays scattered from the first and second layer. It is important to note, that the shape of the CTRs, which is given by $|F_{\text{total}}|$, is independent of the termination of the layers, since the silver layers used for the calculations, were not relaxed. All plots in this thesis, where the structure factor F is included, are strictly speaking graphs of $|F|$, but they are labeled by 'F' for the sake of simplicity. The use of synchrotron radiation is a

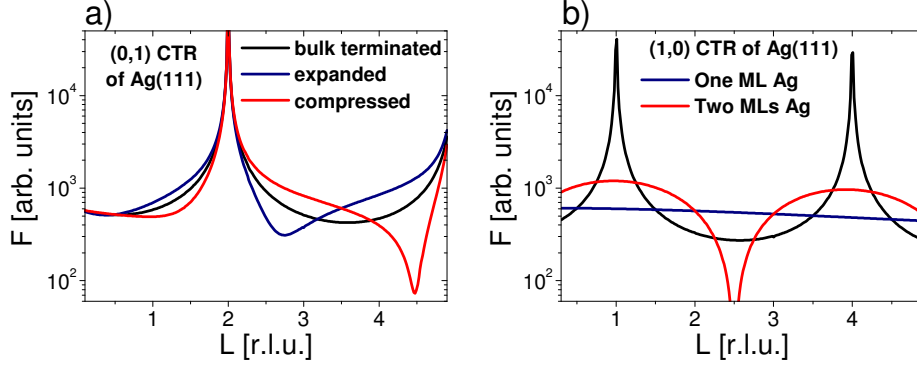


Figure 3.1: Surface sensitivity of SXRD exemplified on the shape of the $(0,1,L)$ and $(1,0,L)$ CTRs of the Ag(111) surface. The \mathbf{q}_z value L is given in reciprocal lattice units (r.l.u.) of the primitive Ag(111) unit cell in hexagonal coordinates. a) The effect of a contraction and expansion of the first Ag(111) layer by $\pm 10\%$ is compared to a bulk terminated surface. b) Surface contribution of one and two monolayers (MLs) silver on a Ag(111) surface.

prerequisite for SXRD measurements, since the scattered intensity $I(\mathbf{q}) \propto |F_{\text{total}}(\mathbf{q})|^2$ along the CTRs varies within 5 orders of magnitude, as can be seen in figure 3.1.

A reconstruction of the surface leads to the appearance of scattered intensity at non-integer values of H and K along the L direction, which are called surface rods. This observation is related to the enlargement of the surface unit cell in the surface plane, resulting in bigger lattice plane spacings. The H and K values associated to the reconstruction are consequently smaller than the bulk values. The signal on the surface rods is **only** induced by scattering from atoms within the reconstructed part of the surface and is given by F_{surf} defined in equation 3.7. Consequently, surface rods feature an *intrinsic surface sensitivity*. Generally, reconstructions are defined by their in-plane unit cell vectors \mathbf{b}_1 and \mathbf{b}_2 , which are related to \mathbf{a}_1 and \mathbf{a}_2 in the following way [56]

$$\mathbf{b} = \mathfrak{M} \cdot \mathbf{a} \quad (3.9a)$$

$$\mathfrak{M}_{p(4 \times 4)} = \begin{pmatrix} 4 & 0 \\ 0 & 4 \end{pmatrix} \quad \text{example of a } p(4 \times 4) \text{ reconstruction} \quad (3.9b)$$

A short introduction to 2D Crystallography and the classification of reconstructions is given in appendix A.2.

Surface X-Ray Diffraction under Grazing Incidence

The penetration depth of hard x-rays in solid materials is normally on the order of several μm . Surface sensitivity is enhanced due to total external reflection of x-rays at an interface. The index of refraction for x-rays is given by

$$n = 1 - \delta - i\beta \quad \delta \text{ and } \beta > 0 \quad (3.10a)$$

$$|n| \leq 1 = n_{\text{vacuum}} \quad (3.10b)$$

The dispersive part $\delta = \lambda^2 r_0 \rho / 2\pi$ is on the order of 10^{-5} , where ρ is the electron density. The dissipative part $\beta \sim 10^{-6}$. Total external reflection can be observed, since $|n| < n_{\text{vacuum}}$. The critical angle α_c for total external reflection can be derived from Snell's law.

$$\alpha_c \cong \sqrt{2\delta} \quad (3.11)$$

By convention, the angle is measured with respect to the surface plane. For silver $\alpha_c = 0.34^\circ$ at a photon energy of 10.5 keV. For an incident angle of the x-rays $\alpha_i \leq \alpha_c$ the component of \mathbf{k}_i parallel to the surface normal \mathbf{k}_z is exponentially damped, resulting in a so-called evanescent wave travelling in the surface plane [29].

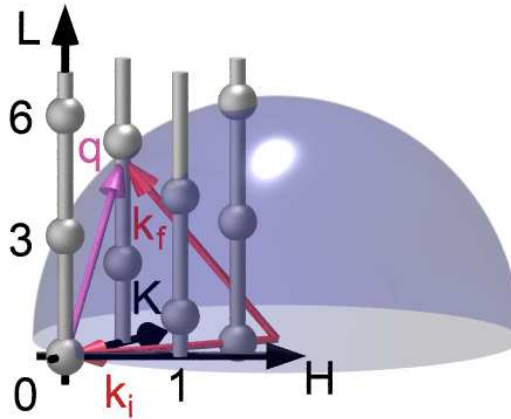


Figure 3.2: Ewald sphere for SXR D scattering geometry under grazing incidence. The incident angle of the incoming wave is set to 0° and the wave travels along the $(\bar{1}\bar{1}0)$ direction. The radius of the Ewald sphere corresponds to a x-ray energy of 10.5 keV. CTRs of the Ag(111) surface are shown as rods and Bragg peaks are marked by spheres.

The penetration depth of the evanescent wave is typically $\sim 50 \text{ \AA}$, giving rise to a drastic reduction of the background, if SXR D measurements are performed with α_i

close to α_c . The transmissivity shows a maximum of 4 for $\alpha_i = \alpha_c$, enhancing additionally the scattered signal. A full treatment of the *distorted wave Born approximation*, which is used to describe these effects, can be found in [29]. In figure 3.2 the scattering geometry is shown for a SXRD experiment under grazing incidence.

Debye-Waller Factor

The theory of kinematical x-ray diffraction presented so far, applies to rigid atom positions. Lattice vibrations modify the structure factor of the unit cell [23, 24, 57]

$$F_{\text{u.c.}} = \sum_{\mathbf{r}_j} f_j e^{i\mathbf{q}\cdot\mathbf{r}_j} \quad (3.12)$$

The instantaneous position due to lattice vibrations is given by $\mathbf{r}_n + \boldsymbol{\delta}_n$. \mathbf{r}_n is the time-averaged mean position of the atom n and the displacement is given by $\boldsymbol{\delta}_n$. Since we are dealing with harmonic oscillations, the time average of the displacement is given by $\langle \boldsymbol{\delta}_n \rangle = 0$. The important value is the time average of the scattered intensity

$$I(\mathbf{q}) = \left\langle \sum_m f_m(\mathbf{q}) e^{i\mathbf{q}\cdot(\mathbf{r}_m + \boldsymbol{\delta}_m)} \sum_n f_n^*(\mathbf{q}) e^{-i\mathbf{q}\cdot(\mathbf{r}_n + \boldsymbol{\delta}_n)} \right\rangle \quad (3.13a)$$

$$= \sum_m \sum_n f_m(\mathbf{q}) f_n^*(\mathbf{q}) e^{i\mathbf{q}\cdot(\mathbf{r}_m - \mathbf{r}_n)} \langle e^{i\mathbf{q}\cdot(\boldsymbol{\delta}_m - \boldsymbol{\delta}_n)} \rangle \quad (3.13b)$$

Only relevant are the components δ_{qm} and δ_{qn} perpendicular to the scattering planes. The last term in equation 3.13b is rewritten as

$$\langle e^{i\mathbf{q}\cdot(\boldsymbol{\delta}_m - \boldsymbol{\delta}_n)} \rangle = \langle e^{iq(\delta_{qm} - \delta_{qn})} \rangle \quad (3.14)$$

Further simplification of equation 3.13 is obtained by the relation

$$\langle e^{ix} \rangle = e^{-\frac{1}{2}\langle x^2 \rangle}, \quad (3.15)$$

which is valid for a Gaussian distribution of x or if x is small and has equal probability of being positive or negative [23]. Applying relation 3.15 to equation 3.13b gives the intensity distribution $I(\mathbf{q})$, modified by harmonic lattice vibrations

$$I(\mathbf{q}) = \sum_m \sum_n f_m(\mathbf{q}) e^{-\frac{1}{2}q^2\langle\delta_{qm}^2\rangle} e^{i\mathbf{q}\cdot\mathbf{r}_m} f_n^*(\mathbf{q}) e^{-\frac{1}{2}q^2\langle\delta_{qn}^2\rangle} e^{-i\mathbf{q}\cdot\mathbf{r}_n} \quad \text{DWF} \quad (3.16a)$$

$$+ \sum_m \sum_n f_m(\mathbf{q}) e^{i\mathbf{q}\cdot\mathbf{r}_m} f_n^*(\mathbf{q}) e^{-i\mathbf{q}\cdot\mathbf{r}_n} \left\{ e^{q^2\langle\delta_{qm}\delta_{qn}\rangle} - 1 \right\} \quad \text{TDS} \quad (3.16b)$$

The intensity distribution is split into two parts. The first term contains the *Debye-Waller factor* (DWF) and the second term explains the observation of *thermal diffuse*

scattering (TDS). The TDS contribution is governed by the correlations $\langle \delta_{qm} \delta_{qn} \rangle$, resulting in streaks of diffuse scattered intensity. An impressive example of TDS is given in [58]. An introduction to TDS and to diffuse x-ray scattering in general can be found in [59, 60]. For the x-ray diffraction studies presented in this thesis, TDS is a part of the background, which has to be subtracted.

The structure factor $F(\mathbf{q}, T)$ can be rewritten using equation 3.16a

$$F(\mathbf{q}, T) = \sum_{\mathbf{r}_j}^{\text{unit cell}} f_j(\mathbf{q}) e^{-M_j(q^2, T)} e^{i\mathbf{q} \cdot \mathbf{r}_j} \quad (3.17)$$

The exponential function $e^{-M_j(q^2, T)}$ in equation 3.17 is the Debye-Waller factor.

$$M_j(q^2, T) = \frac{1}{2} q^2 \langle \delta_{qj}^2(T) \rangle = \frac{B_j(T) q^2}{16\pi^2} \quad (3.18a)$$

$$B_j(T) = 8\pi^2 \langle \delta_{qj}^2(T) \rangle \quad B_{j, \text{isotropic}}(T) = \frac{8\pi^2}{3} \langle \delta^2(T) \rangle \quad (3.18b)$$

The factor of $16\pi^2$ is necessary, since $B_j(T)$ is defined in units of $\sin^2 \vartheta / \lambda$, which is the crystallographic definition of the wave vector transfer. The Debye-Waller factor decreases the scattered intensity, but does not change the width of the reflections. In addition, a q^2 -dependency is observed and as the amplitude of the vibrations is temperature dependent, the Debye-Waller factor decreases with increasing temperature. For the case of silver $B_{\text{Ag}}(T = 300 \text{ K}) = 0.82 \text{ \AA}^2$ [61].

Patterson Function

The electron density $\varrho(x, y, z)$ is simply given by the Fourier transform of the structure factor [23, 62]

$$\varrho(x, y, z) = \frac{1}{V} \sum_{\text{HKL}} F_{\text{HKL}} e^{-2\pi i [H(x/a) + K(y/b) + L(z/c)]}, \quad (3.19)$$

where V is the volume of the unit cell, and a , b and c are the lattice constants. The electron density may be projected on any lattice plane. Important for SXRD is a projection of the cell content along the c -axis. The corresponding electron density distribution $\varrho'(x, y)$ is given by [23, 62]

$$\varrho'(x, y) = \frac{1}{A_{\text{ab}}} \sum_{\text{HK}} F_{\text{HK}0} e^{-2\pi i [H(x/a) + K(y/b)]} \quad (3.20)$$

The area of the unit cell in the surface plane is given by A_{ab} . Experimentally, only $|F_{\text{HKL}}|$ can be determined. To overcome this problem, Patterson introduced an auto

correlation function of the electron density $P(X, Y, Z)$ [62], which only depends on $|F_{\text{HKL}}|^2$.

$$P(\mathbf{X}) = \iiint_V \varrho(\mathbf{x}) * \varrho(\mathbf{x} + \mathbf{X}) \frac{V}{abc} d\mathbf{x} \quad (3.21a)$$

$$P(\mathbf{X}) = \frac{1}{V} \sum_{\text{HKL}} |F_{\text{HKL}}|^2 \cos 2\pi \left(H \frac{X}{a} + K \frac{Y}{b} + L \frac{Z}{c} \right) \quad (3.21b)$$

Applying equation 3.20, we obtain the Patterson function $P(X, Y)$ for the relevant case of $\varrho'(x, y)$

$$P(X, Y) = \frac{1}{A_{ab}} \sum_{\text{HK}} |F_{\text{HK}0}|^2 \cos 2\pi \left(H \frac{X}{a} + K \frac{Y}{b} \right) \quad (3.22)$$

A maximum in the Patterson function corresponds to a distance between two atoms or a sum or a difference of distances respectively, only in this case $\varrho(\mathbf{x}) * \varrho(\mathbf{x} + \mathbf{X}) \neq 0$. Even though, $P(X, Y)$ is not a measure of the electron density ϱ , it delivers important information about interatomic distances, which are used to build a structural model. Subsequently, the model is refined by a least square fitting procedure. In figure 3.3a) a topview of the hexagonal Ag(111) unit cell is shown. In figure 3.3b) and c) the corresponding Patterson function is plotted in a contour diagram for different intervals of the summation over H and K.

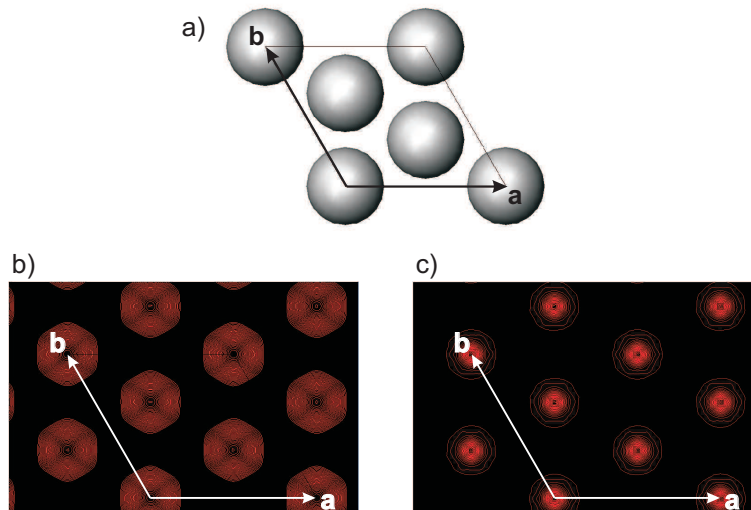


Figure 3.3: a) Topview of the Ag(111) unit cell. b) Patterson function calculated for $H, K \in [-2, 2]$. c) Patterson function calculated for $H, K \in [-10, 10]$.

The more Fourier components are included in the summation, the finer the details visible in $P(X, Y)$. The situation shown in figure 3.3b), corresponds to typically ac-

cessible values of q , if SXRD experiments are performed at a photon energy of ~ 10 keV.

The *heavy atom method* can be applied, if there is a big difference in ρ for the different types of atoms in the unit cell [63]. In this case, the Patterson function is dominated by the contribution of the heavy atoms. This condition is fulfilled by the contrast in electron density of silver and oxygen atoms. Consequently, the heavy atom method can be used to build a structural model of oxygen induced reconstructions of silver surfaces, keeping in mind, that the maxima of $P(X, Y)$ are projected along $\mathbf{a}_3 \equiv \mathbf{c}$, onto the $(\mathbf{a}_1, \mathbf{a}_2)$ -plane.

Determination of Structure Factors

In kinematical diffraction theory the crystal is thought to be built up of small mosaic blocks. The diffracted signal is an incoherent superposition of the signal scattered by each block, which is shown in figure 3.4.

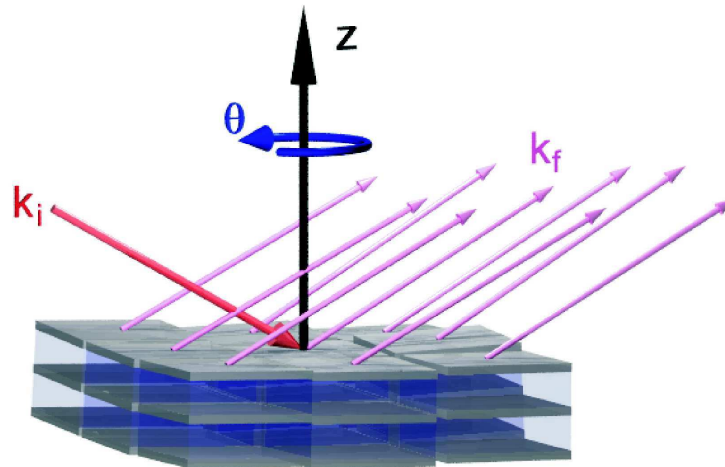


Figure 3.4: Illustration of scattering from an imperfect crystal, which is built up by mosaic blocks. The mosaicity of a metal crystal is typically on the order of 0.1° . For the sake of simplicity, only one \mathbf{k}_i is shown. In a SXRD experiment the integrated intensity is measured by rocking the crystal around the surface normal. The rocking angle is usually labelled as θ or ω .

The structure factor is determined from the integrated intensity of *rocking scans*, measured by SXRD, which are performed at constant \mathbf{q}_z . For this purpose, the sample is rotated (respectively *rocked*) by an angle θ around the surface normal at fixed detector position. The integrated intensity can be calculated by integration of the *differential*

scattering cross section $d\sigma/d\Omega$ [64].

$$\frac{d\sigma}{d\Omega} = r_0^2 \frac{A}{A_{ab}} |F(\mathbf{q})|^2 P u(\mathbf{q}) \quad (3.23a)$$

$$I_{\text{int}} = \frac{\Phi_0}{\omega_0} \int \frac{d\sigma}{d\Omega} d\gamma d\Psi d\theta \quad (3.23b)$$

A is the illuminated surface area, P is dependent on the polarisation of the x-rays, $u(\mathbf{q})$ is a normalised function describing the line shape, Φ_0 defines the incident photon flux, ω_0 is the angular velocity of the rocking scan and γ and Ψ are related to the angular acceptance of the detector. Integration of equation 3.23b results in

$$I_{\text{int}} = C_{\text{Experiment}} * |F(\mathbf{q})|^2 * C_{\text{tot}} \quad (3.24a)$$

$$C_{\text{Experiment}} = \frac{\Phi_0 r_0^2 A_0 \lambda^2 \Delta\gamma}{A_{ab}^2 \omega_0} \quad (3.24b)$$

$$C_{\text{tot}} = P L C_{\text{rod}} C_{\text{area}} \quad (3.24c)$$

A_0 is a geometrical constant defined by the in-plane widths of the incoming x-ray beam and the detector slits and $\Delta\gamma$ is the out-of-plane angular acceptance of the detector. The terms 'in-plane' and 'out-of-plane' are always referred to the surface plane. C_{tot} depends on the scattering geometry. The corrections listed in equation 3.24c, due to the polarisation of the x-rays P , the Lorentz factor L , a correction for the active surface area C_{area} and the rod interception C_{rod} , are derived for a z-axis diffractometer in [64]. The z-axis geometry, shown in figure 4.3, was used for our SXRD experiments. $C_{\text{Experiment}}$ is a constant during an experiment, so, $|F(\mathbf{q})|$ is determined by

$$|F(\mathbf{q})| = \sqrt{\frac{I_{\text{int}}}{C_{\text{tot}}}}. \quad (3.25)$$

Within this thesis $|F(\mathbf{q})|$ was calculated from measured rocking scans with the software ANA by E. Vlieg [65].

Determination of Surface Structures

The 3D surface structure can be determined by SXRD with sub-Å resolution. For this purpose, a given structural model is refined by a least square fitting routine. In each iteration step the $|F(\mathbf{q})|$ -distribution is calculated, by the scheme presented in the preceding sections, for all measured data points. The agreement between calculation and measurement is improved by moving the atoms along predefined directions. In this procedure constraints due to the symmetry of the diffraction pattern are included. The goodness of the fit is expressed in terms of χ^2

$$\chi^2 = \frac{1}{M - p} \sum_{\mathbf{q}} \frac{|F_{\text{calc}}(\mathbf{q})|^2 - |F_{\text{exp}}(\mathbf{q})|^2}{\zeta(\mathbf{q})} \quad (3.26)$$

M is the number of data points, p the number of fitting parameters and $\zeta(\mathbf{q})$ is the sum of statistical errors and systematical errors, due to the misalignment of the sample. The refinement procedures were accomplished with the software ROD by E. Vlieg [65].

3.2 High Resolution Core Level Spectroscopy

HRCLS is also known as **X-Ray Photoelectron Spectroscopy (XPS)** or **Electron Spectroscopy for Chemical Analysis (ESCA)** [30–32]. The term HRCLS is used for measurements, which are performed at synchrotron light sources. In this experimental technique a core hole is created by an incident photon and a photoelectron is emitted, showing a kinetic energy E_{kin} . The definition of the energy levels is shown in figure 3.5. The important quantity is the binding energy E_{bind} of the electron defined by

$$E_{\text{bind}} = h\nu - E_{\text{kin}} - \Phi, \quad (3.27)$$

where Φ is the work function of the metal surface and $h\nu$ the energy of the incident photon. Core level spectroscopy can be applied for all elements besides H and He, since at least one electron must occupy the L-shell.

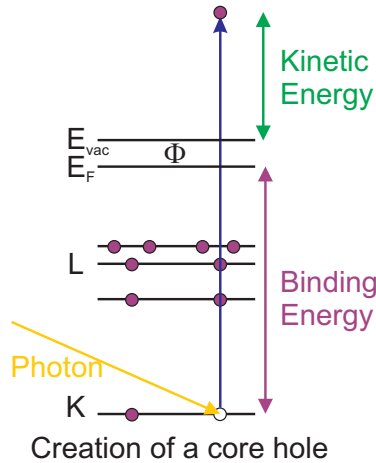


Figure 3.5: Emission of a photoelectron from a core level.

XPS spectra are element specific and are tabulated [66, 67]. In addition, photoelectron spectroscopy is highly surface sensitive, due to the low inelastic mean free path of electrons with a kinetic energy in the range of 10 to 1000 eV [32, 68]. Typical values

for the inelastic mean free path are 5 to 20 Å and can be described by a 'universal curve' [68].

Even though, core levels are not directly involved in the chemical bonds, so-called chemical shifts of the binding energy due to the chemical surrounding can be observed. These effects are caused by the local electronic structure, which is for example dependent on the oxidation state of the element. Furthermore, different adsorption sites correspond to different adsorption geometries, introducing also chemical shifts, which can be used as a fingerprint for the respective binding geometry.

HRCLS has two major advantages compared to the use of laboratory x-ray sources. The use of synchrotron radiation allows measurements with variable x-ray energy and the high brilliance of the synchrotron source results in a higher resolution of the spectra. Energy dependent measurements can be applied to distinguish between bulk and surface components of the substrate material. The higher the photon energy the lower is the relative photoelectron yield of the surface signal, due to the energy dependency of the inelastic mean free path of the electrons.

3.2.1 Doniach-Šunjić Line Shape

The line shape of the photoemission process is affected by many different effects, which are commonly divided into initial and final state effects [30–32].

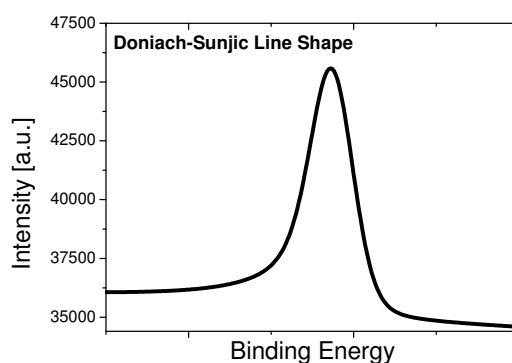


Figure 3.6: Doniach-Šunjić line shape convoluted with a Gaussian and a Lorentzian. The high energy side of the peak shows a higher photoelectron yield. By convention, the direction of the energy axis is inverted.

In a metal the escaping photoelectron creates many low energy electron hole pairs. The number of these pairs is dependent on the density of states at the Fermi level. This process is accompanied by a loss of kinetic energy of the photoelectrons, resulting in an asymmetric line shape, showing more intensity on the high binding energy side of

the peak. The first complete theoretical treatment of this issue was done by Doniach and Šunjić (DŠ) [69] and a typical example is shown in figure 3.6. The singular DŠ line shape is convoluted with a Lorentzian, showing a full width at half maximum (FWHM) γ , due to the lifetime of the core hole. The yield function $Y(\Delta E)$ of the photoemission process is given by [69]

$$Y(\Delta E) = \frac{\Gamma (1 - \alpha)}{(\Delta E^2 + \gamma^2)^{(1-\alpha)/2}} \cos \left\{ \frac{\pi \alpha}{2} + \Theta(\Delta E) \right\} \quad (3.28a)$$

$$\Theta(\Delta E) = (1 - \alpha) \tan^{-1}(\Delta E/\gamma). \quad (3.28b)$$

ΔE is the energy offset with respect to the line shape without lifetime broadening and Γ is the gamma function. α is the asymmetry parameter of the DŠ line shape, giving also rise to a shift of the peak. Typical values for α are on the order of 0.1. Additionally, the DŠ line shape is convoluted with a Gaussian, due to instrumental resolution and unresolved vibrations of the atoms.

Inelastic processes of the escaping photoelectron involving other electrons are classified in shake-up and shake-off processes. In a shake-up process an electron is excited, but does not leave the solid. A typical example are plasmon losses in metals giving rise to characteristic peaks on the high energy tail of the photoemission peak. In a shake-off process the excited electron leaves also the metal. Correspondingly, the DŠ line shape is a low energy shake-up excitation.

In this thesis HRCLS spectra of the substrate atoms and atoms of reconstructed parts of the surface are decomposed using DŠ line shapes. The fitting routines were performed with the software FitXPS by D.L. Adams. The decomposition reveals the number of different types of atoms of one element, due to the splitting of the spectrum by chemical shifts.

3.3 Normal Incidence X-Ray Standing Waves

X-Ray Diffraction by perfect crystals is described by dynamical diffraction theory. Multiple scattering effects, giving rise to primary extinction, and effects due to refraction are included in this theoretical description. The most prominent result is the finite width of the Bragg peaks [23, 24, 33, 70–74]. Important for NIXSW, is the occurrence of a x-ray interference field (XIF) in and outside the crystal [34, 35]. Normally, photoelectrons, excited by the XSW, are recorded by means of XPS. The XSW can be moved with respect to the lattice planes, by changing the Bragg angle ϑ . Combining the ability to move the XSW with XPS, allows the determination of atomic positions in a direction perpendicular to the scattering planes. The method is element specific and shows surface sensitivity due to XPS.

3.3.1 Dynamical X-Ray Diffraction Theory

The effect of anomalous transmission of x-rays through a crystal in Laue geometry observed by Borrmann [33], can only be explained by solving Maxwell's equations for a medium showing periodic electron density, by using Bloch waves. The main results obtained for the Bragg case (incident and scattered wave on the same side of the crystal), are presented in the following sections.

Darwin's Theory of Dynamical X-Ray Diffraction

A description of this theory can be found in [23, 24, 70, 71]. The scattering process is described by a semi-infinite slab of scattering planes, each showing a transmissivity and reflectivity. A wave which is scattered once, can be rescattered by the 'backside' of a diffraction plane, so that the wave, which was scattered twice, moves along the direction of the incoming wave field. Waves, which pass through an even number of scattering processes, contribute to the extinction of the incoming x-rays. The total scattered intensity is determined by summing up all the contributions from all layers, including the correct phase factors.

All results of this description are included in the approach developed by Ewald and von Laue, which is presented in the following section. Furthermore, a complete understanding of the splitting of the incident wave in the crystal and the energy flow can only be obtained by the full electrodynamic treatment of the diffraction process.

Ewald's and von Laue's Description of Dynamical X-Ray Diffraction

The approach presented in this section, was mainly developed by Ewald and von Laue [72–74]. The complete description can be found in the review article by Batterman and Cole [33]. The notation by Batterman and Cole is used in this section. In this notation the wave vector is given by \mathbf{K} and $|\mathbf{K}| = 1/\lambda$. The wave vector transfer is given by \mathbf{H} and $|\mathbf{H}| = 1/d$, whereas d is the lattice plane spacing. The scattering processes, fulfilling Bragg's law, are described by

$$\mathbf{K}_H = \mathbf{K}_0 + \mathbf{H} \quad (3.29)$$

The problem is to solve Maxwell's equations for a medium showing a periodic electron density $\varrho(\mathbf{r})$ (see also equation 3.19), which can be described by a complex dielectric constant $\kappa(\mathbf{r})$.

$$\kappa(\mathbf{r}) = 1 - \frac{r_0 \lambda^2}{\pi} * \varrho(\mathbf{r}) \quad (3.30)$$

Using the abbreviation Γ , we can express $\kappa(\mathbf{r})$ in terms of the complex structure

factor $F_{\mathbf{H}}$.

$$\Gamma = \frac{r_0 \lambda^2}{\pi V} = \left(\frac{e^2}{4\pi\epsilon_0 mc^2} \right) * \frac{\lambda^2}{\pi V} \quad (3.31a)$$

$$\kappa(\mathbf{r}) = 1 - \Gamma \sum_{\mathbf{H}} F_{\mathbf{H}} \exp(-2\pi i \mathbf{H} \cdot \mathbf{r}) \quad (3.31b)$$

$$F_{\mathbf{H}} = \sum_{\mathbf{r}_n} (f(\mathbf{H}) + f'(\hbar\omega) + i f''(\hbar\omega))_{\mathbf{n}} e^{2\pi i \mathbf{H} \cdot \mathbf{r}_n} \quad (3.31c)$$

$f'(\hbar\omega)$ and $f''(\hbar\omega)$ are the dispersion corrections to $f(\mathbf{H})$, due to resonance and absorption [24]. They must be included, to calculate the correct shape of the Bragg peaks. The dispersion corrections for any element can be found in [75, 76], $f(\mathbf{H})$ can be calculated by approximation parameters listed in [77].

It can be shown [33, 74], that Bloch waves can be used as Ansatz to obtain a set of waves, which satisfy Bragg's law (see 3.29) and Maxwell's equations at the same time:

$$\mathfrak{A} = \left\{ \sum_{\mathbf{H}} \mathfrak{A}_{\mathbf{H}} e^{-2\pi i \mathbf{H} \cdot \mathbf{r}} \right\} e^{-2\pi i \mathbf{K}_0 \cdot \mathbf{r}} e^{2\pi i \nu t} \quad \text{Bloch wave} \quad (3.32a)$$

$$\nabla \times \mathfrak{E} = -\mu_0 \frac{\partial \mathfrak{H}}{\partial t} \quad (3.32b)$$

$$\nabla \times \mathfrak{H} = \epsilon_0 \frac{\partial (\kappa \mathfrak{E})}{\partial t}, \quad (3.32c)$$

where \mathfrak{A} is either \mathfrak{E} or \mathfrak{H} and the wave vectors inside the crystal are complex numbers. This Ansatz describes the elastic scattering of waves by a periodic charge density, which is given by the Fourier transform of $F_{\mathbf{H}}$. The result is the following pair of equations for the field amplitudes of the incident and the scattered wave vector.

$$\left\{ k^2(1 - \Gamma F_0) - (\mathbf{K}_0 \cdot \mathbf{K}_0) \right\} E_0 - k^2 P \Gamma F_{\bar{\mathbf{H}}} E_{\mathbf{H}} = 0, \quad (3.33a)$$

$$-k^2 P \Gamma F_{\mathbf{H}} E_0 + \left\{ k^2(1 - \Gamma F_0) - (\mathbf{K}_{\mathbf{H}} \cdot \mathbf{K}_{\mathbf{H}}) \right\} E_{\mathbf{H}} = 0. \quad (3.33b)$$

k is the value of the incident wave vector outside the crystal and P is a factor depending on the polarisation state of the incoming x-ray beam. For the sake of simplicity we assume that $P = 1$, which is true for σ polarisation (\mathfrak{E}_0 perpendicular to the plane defined by \mathbf{K}_0 and $\mathbf{K}_{\mathbf{H}}$). A nontrivial solution is obtained, if the determinant of the pair of linear homogeneous equations of the field vectors equals zero. Introducing the abbreviations ξ_0 and $\xi_{\mathbf{H}}$, one obtains the fundamental equation, which describes the hyperbolic dispersion surface (comparable to the electronic band structure of a solid),

which defines the loci of allowed wave vectors \mathbf{K}_0 and \mathbf{K}_H inside the crystal.

$$\xi_0 = \sqrt{\mathbf{K}_0 \cdot \mathbf{K}_0} - k \left(1 - \frac{1}{2} \Gamma F_0\right), \quad (3.34a)$$

$$\xi_H = \sqrt{\mathbf{K}_H \cdot \mathbf{K}_H} - k \left(1 - \frac{1}{2} \Gamma F_0\right) \quad \text{and} \quad (3.34b)$$

$$\xi_0 \xi_H = \frac{1}{4} k^2 \Gamma^2 F_H F_{\bar{H}}. \quad \text{Dispersion Surface} \quad (3.34c)$$

Keeping in mind, that $|\mathbf{K}_0| = |\mathbf{K}_H|$, one can show, that equation 3.34c describes a hyperboloid, which is shown in figure 3.7.

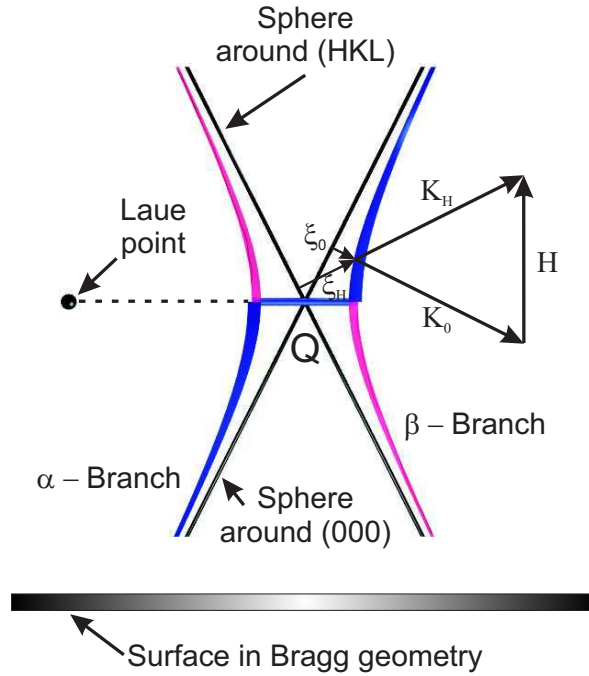


Figure 3.7: Illustration of the dispersion surface and the construction of incident and scattered wave vectors. In Bragg geometry, the blue coloured parts of the dispersion surface are active, due to the boundary conditions.

The scattering occurs in the plane defined by \mathbf{K}_0 and \mathbf{K}_H . A coordinate transformation is always possible in a way, that the dispersion surface is given by two hyperbolae, as it is shown in figure 3.7. Since $|\mathbf{K}_0| < k$ the Ewald sphere construction is modified. The Laue point L, which is shown in figure 3.7, is the centre of the Ewald sphere valid in kinematical diffraction theory. In dynamical x-ray diffraction theory \mathbf{K} is a complex number and the centre of the Ewald sphere is defined by the point Q, shown in figure 3.7. The distance $LQ \ll k$. The spheres about (000) and (HKL) can be approximated

linearly in the vicinity of Q and show an asymptotic behaviour with respect to the dispersion surface. The offset of the centre of the Bragg peak given by the distance LQ, can be calculated by [24]

$$\varsigma_0 = \frac{2d^2 |F_0|}{\pi m V} r_0, \quad (3.35)$$

where m is the order of the reflection. Important for x-ray diffraction is the complex ratio of the field amplitudes, which is given by

$$\boxed{\frac{E_H}{E_0} = -\frac{k \Gamma F_H}{2 \xi_H}} \quad (3.36)$$

At the diameter points of the hyperbolae the ratio of the field amplitudes tends to $E_H/E_0 \rightarrow \pm 1$. The width of the area of total reflection, for the case of no absorption, is correspondingly given by the distance of the diameter points D. For this case $\Re(\mathbf{K}_0) = 0$ and the phenomenon of total external reflection is observed.

$$D = k \Gamma |F_H| \sec \vartheta_B \quad (3.37)$$

The boundary conditions, given by the scattering geometry, select the active parts of the dispersion surface. In figure 3.7 the active part is shown in blue colour, for the relevant case of the Bragg geometry. It can be shown [33], that the reflected intensity R of a Bragg peak in Bragg geometry, is given in terms of the complex variable $\eta = \eta' + i\eta''$, by

$$R = \frac{|E_H|^2}{|E_0|^2} = \left| \eta - \sqrt{\eta^2 - 1} \right|^2 \quad \text{for } \eta' \geq 1, \quad (3.38a)$$

$$R = \frac{|E_H|^2}{|E_0|^2} = \left| \eta - i \sqrt{1 - \eta^2} \right|^2 \quad \text{for } |\eta'| \leq 1, \quad (3.38b)$$

$$R = \frac{|E_H|^2}{|E_0|^2} = \left| \eta + \sqrt{\eta^2 - 1} \right|^2 \quad \text{for } \eta' \leq -1, \quad (3.38c)$$

$$\eta' = (-\Delta \vartheta \sin 2\vartheta + \Gamma F'_0) / |P| \Gamma F'_H \text{ and} \quad (3.38d)$$

$$\eta'' = -(F''_H/F'_H)(\eta' - 1/|P|F''_H/F''_0). \quad (3.38e)$$

The shape of the Bragg peak, the so-called Darwin-Prins curve, defined by the slope of the reflectivity $R = |E_H|^2/|E_0|^2$ is shown in figure 3.8. The asymmetric shape of the Darwin-Prins curve, can be explained by the coherent superposition of E_H and E_0 , leading to a standing wave field in and outside the crystal. For $\eta = 1$ the maxima of the x-ray interference field (XIF) lie in the middle of the Ag(111) planes, where no atoms are present. The absorption, described by $f''(\hbar\omega)$, shows consequently a minimum for $\eta = 1$, leading to a maximum in the reflected signal. In the whole range, given by

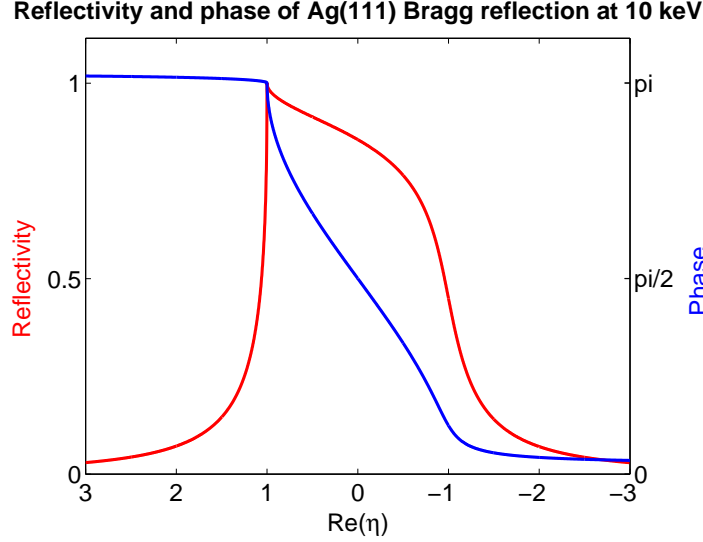


Figure 3.8: Darwin-Prins curve for the Ag(111) reflection at a photon energy of 10 keV. Additionally, the phase between E_H and E_0 is shown. The complex structure factor is given by $F_{111} = 4 * (37.435 + 0.054 - i * 2.924)$. Without absorption (Darwin curve) the reflectivity R equals 1 for $|\eta| \leq 1$.

$|\eta| \leq 1$, total external reflection of the impinging plane wave is observed. Nevertheless, the reflected intensity shows a minimum for $\eta = -1$, due to a shift of the XIF by half a lattice plane spacing $d/2$, which corresponds to the phase shift of π between E_H and E_0 , shown in figure 3.8. For $\eta = -1$ the antinodes of the XIF lie on the lattice planes, accordingly the absorption of the x-rays shows a maximum at this position. The Bragg peak is a resonant excitation of the periodic charge density by the x-rays, consequently the phase shift of π between E_H and E_0 is observed along the Darwin-Prins curve. It is important to note, that scattering by a free electron introduces a phase shift of π between the incident plane wave and the scattered wave [24, 78]. The sides of the Bragg peaks pass into the CTRs, which are described by kinematical diffraction theory. Without absorption ($f''(\hbar\omega) = 0$) the reflectivity equals 1 for $|\eta| \leq 1$. The shape of the Bragg peak is then described by the flat top shaped Darwin curve [24, 33].

The angular full width at half maximum (FWHM) of a Darwin curve w_D^{FWHM} (without absorption) is given by [24]

$$w_D^{\text{FWHM}} = \frac{6}{\pi \sqrt{2}} \left(\frac{d}{m} \right)^2 \frac{r_0 |F|}{V} * \tan \vartheta. \quad (3.39)$$

For the case of the Ag(111) reflection at 10 keV, one obtains a value of $\sim 0.002^\circ$.

As can be seen from equation 3.39, w_D^{FWHM} becomes smaller for higher photon energies, since ϑ gets smaller.

3.3.2 Standing Wave Technique

The x-ray standing wave technique [34, 35] is a combination of x-ray diffraction in Bragg geometry (cf. preceding section) combined with spectroscopy. The choice of the spectroscopic technique depends on the intention of the experiment, either fluorescence or Auger electrons or photoelectrons excited by the x-ray interference field are measured. Batterman realised the first XSW experiment, by measuring the fluorescence of a perfect Ge crystal excited by Mo K_α radiation [79].

An extension of this principle are XSW experiments under normal incidence of the x-ray beam. This allows measurements of metal crystals, showing a mosaicity on the order of 0.1° , which is 2 to 3 orders of magnitudes larger than typical Darwin widths. Under normal incidence ϑ equals 90° , correspondingly, equations 3.38 and 3.39 cannot be applied. If $\vartheta = 90^\circ$ is approached $w_D^{\text{FWHM}} \rightarrow \infty$ since the term $\tan \vartheta$ diverges. The theory of dynamical x-ray diffraction was modified for this case and the width of the region of total external reflection (RTR) can be calculated by [36]

$$w^{\text{RTR}} = 2 * |\chi_H|^{0.5} = 2 * \sqrt{\Gamma |F_H|}. \quad (3.40)$$

χ_H is the Fourier component to the wave vector transfer H of the susceptibility. The Darwin curve shows a width of $\sim 0.32^\circ$ for the Ag(111) reflection, being slightly bigger than typical values of the mosaicity of Ag crystals.

Under normal incidence, the photon energy cannot be chosen arbitrarily, but is given by the Bragg equation for $\vartheta = 90^\circ$

$$2 d = m \lambda \quad (3.41a)$$

$$E_{\text{Photon}} = \frac{m h c}{2 d} \quad (3.41b)$$

For the Ag(111) reflection one obtains a photon energy of 2.6283 keV for $2 \vartheta = 180^\circ$. The Darwin curve, which is also called rocking curve, can either be measured by changing ϑ or by scanning the photon energy E .

The x-ray interference field is given by the coherent superposition of the incoming and the Bragg reflected wave, the total electric field $\mathbf{E}(\mathbf{r})$ and the intensity $I(\mathbf{r})$ are given by [34, 80]

$$\mathbf{E}(\mathbf{r}) = \left(\mathbf{e}_0 E_0 e^{i\mathbf{K}_0 \cdot \mathbf{r}} + \mathbf{e}_H E_H e^{i\mathbf{K}_H \cdot \mathbf{r}} \right) e^{-i\omega t} \quad (3.42a)$$

$$I(\mathbf{r}) = |E_0|^2 \left[1 + R + 2 P \sqrt{R} \cos(v + \mathbf{H} \cdot \mathbf{r}) \right], \quad (3.42b)$$

where \mathbf{e}_0 and \mathbf{e}_H are the polarisation unit vectors. v is the phase defined by $E_H/E_0 = \sqrt{R} \exp(iv)$.

Equation 3.42b describes the XSW in and outside the crystal. The rocking curve is measured experimentally. Along the Bragg peak the phase v is changed by π , accordingly, the XSW is moved by half a lattice plane spacing. At each point of the rocking curve the element specific yield of photoelectrons, Auger electrons or the fluorescence is measured. In this work the photoelectron yield was measured by means of XPS. The advantage of XPS is the possibility to detect chemical shifts of adsorbates and the high surface sensitivity. The decomposition of the XPS spectra allows the determination of standing wave profiles for each type of oxygen atom adsorbed on the Ag(111) surface.

The photoelectron yield is determined by time-dependent perturbation theory [34, 80–82], resulting in matrix elements M_{fi} for the transition of the electron from the bound state $|i\rangle$ to the unbound final state $|f\rangle$, where M_{fi} is given by

$$M_{fi} = \langle f | \exp(i\mathbf{k}\mathbf{r})(\mathbf{e}\hat{p}) | i \rangle \quad |\mathbf{k}| = \frac{2\pi}{\lambda} \quad (3.43)$$

\mathbf{e} is the polarisation vector of the electric field and $\hat{p} = -i\hbar\nabla$ the momentum operator. In a multipole expansion the $\exp(i\mathbf{k}\mathbf{r})$ term is approximated by its Taylor series $1 + i\mathbf{k}\mathbf{r} - 1/2(\mathbf{k}\mathbf{r})^2 - \dots$. In the dipole approximation, which is valid for large wavelengths of the x-rays compared to the size of the orbitals of the electrons, only the first term of the expansion is used. The photoelectron yield Y_{dip}^H for the Bragg reflection with wave vector transfer H is then given by [34]

$$Y_{\text{dip}}^H = 1 + R + 2P\sqrt{R}F^H \cos(v - 2\pi P^H). \quad (3.44)$$

P^H and F^H are the phase and amplitude of the Fourier coefficients of the distribution function of the atoms, showing both values between 0 and 1 [34]. P^H and F^H are called coherent position and coherent fraction respectively. In dipole approximation a standing wave profile is completely described by P^H and F^H , where P^H is a measure of the position of the atom in a direction parallel to \mathbf{H} in units of the lattice spacing d . F^H is a measure of the local order of the atoms. The smaller the coherent fraction F^H the wider is the distribution of atoms around the mean position determined by P^H .

In figure 3.9 simulated XSW profiles are shown for $F^H = 0.69$. The profiles show a big difference in their shape in dependency of P^H . For the case of a high coherent fraction, as shown here, a straightforward fit of the profiles is possible. If F^H tends to zero, the yield function is dominated by R and the XSW profiles show only slight differences.

It was realised, that non-dipole effects may play an important role for NIXSW measurements. A complete description of these effects can be found in [80, 81]. For the emission of photoelectrons the matrix element connected to the incoming x-rays and the one connected to the scattered x-rays, which are coupled coherently, must be evaluated. In the following, the effect of electric quadrupole transitions is also

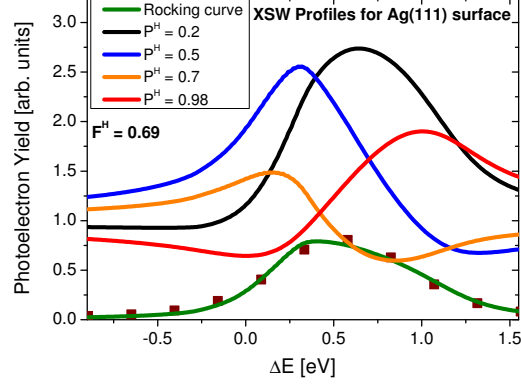


Figure 3.9: Simulated XSW profiles for the Ag(111) Bragg reflection in terms of the offset to the Bragg angle. In the lower part, a Ag(111) rocking curve measured under normal incidence is shown. All XSW profiles are calculated for $F^H = 0.69$.

considered. Magnetic transitions can be neglected. The result is a generalised yield function Y^H in terms of $\mathbf{s}_0 = \mathbf{k}_0/|\mathbf{k}_0|$ and $\mathbf{s}_H = \mathbf{k}_H/|\mathbf{k}_H|$.

$$Y^H = 1 + S_R R + 2 |S_I| \sqrt{R} F^H \cos(v - 2\pi P^H + \psi) \quad (3.45a)$$

$$S_R = \frac{S_{HH}}{S_{00}}, \quad S_I = |S_I| e^{i\psi} = \frac{S_{0H}}{S_{00}} \quad (3.45b)$$

$$S_{00} = \langle |M_{fi}(\mathbf{s}_0)|^2 \rangle \quad (3.45c)$$

$$S_{HH} = \langle |M_{fi}(\mathbf{s}_H)|^2 \rangle \quad (3.45d)$$

$$S_{0H} = \langle M_{fi}(\mathbf{s}_0) * M_{fi}(\mathbf{s}_H) \rangle \quad (3.45e)$$

The analysis of the measured rocking curves and the fits of the standing wave profiles with the generalised yield function were done with the software DARE by J. Ze-genhagen within this thesis.

3.4 Low Energy Electron Diffraction

Diffraction of electrons was observed for the first time by Davisson and Germer [83]. The wave length of electrons is related to their momentum p via the de Broglie relation $\lambda = h/p$. Electrons with a kinetic energy of 150 eV have a de Broglie wave length of 1 Å.

LEED is based on elastic scattering of electrons in back scattering geometry, typical electron energies are in the range of 20 to 300 eV [30,32]. A typical feature of LEED is the intrinsic surface sensitivity, due to the strong interaction of electrons with matter, as already mentioned in section 3.2. The scattering process in reciprocal space is shown in figure 3.10. Modern LEED systems are equipped with a fluorescence screen, to monitor the diffraction pattern. This is an advantage compared to SXRD measurements with a point detector, since all intersections of the Ewald sphere with the rods are monitored at the same time. The higher the electron energy the closer are the reflections to the (00) reflection. A complete structure determination of the surface unit cell is possible by so-called LEED-I(V) measurements. In this technique the intensity I of the rods is measured versus the acceleration voltage V of the electrons. The simulation of the measured profiles is done by dynamical electron scattering theory, which is feasible for small surface unit cells. Furthermore, LEED measurements can be performed only under UHV conditions and only for non-charging systems. In this thesis the structure of surface reconstruction is determined by in-situ SXRD measurements (cf. section 3.1.1).

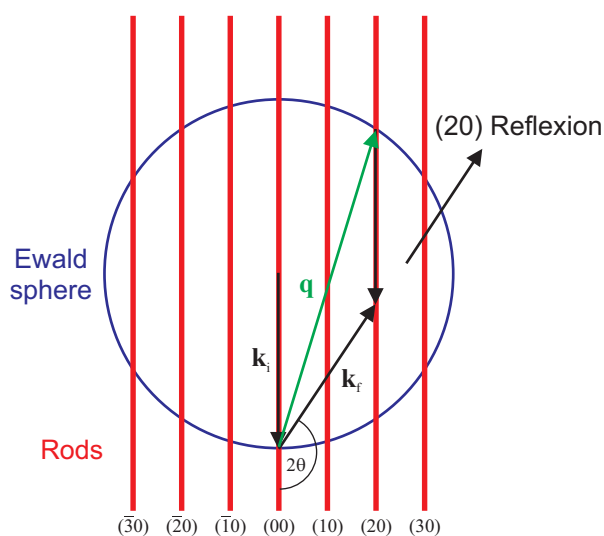


Figure 3.10: Scattering geometry of a LEED experiment. The surface normal is parallel to \mathbf{k}_i . The (20) reflexion is observable in the direction of \mathbf{k}_f .

Nevertheless, LEED is a versatile tool to determine the type of reconstruction on the surface and the quality of the substrate surface is reflected in the spot size of the reflections. Additional information can be gained by examination of the background signal.

3.5 Auger Electron Spectroscopy

Auger electron spectroscopy is based on the Auger process [30, 32, 84]. The Auger process is a radiationless transition competing with the emission of characteristic x-rays. A core hole, which is either produced by photoemission or by incident electrons with kinetic energies in the range of 3 keV, is occupied by an electron from a higher shell. The energy release is transferred to a third electron, which is emitted with a characteristic energy. The emission of Auger electrons can be observed for all elements besides H, He and Li. A typical Auger transition is shown in figure 3.11.

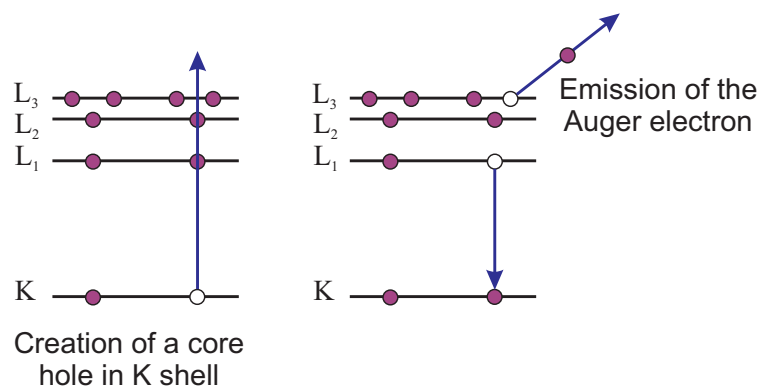


Figure 3.11: The KL₁L₃ Auger transition.

Auger electrons show a kinetic energy up to 1000 eV, giving rise to the intrinsic surface sensitivity of this technique. AES spectra of all elements are tabulated [85] and can be compared with experimental results. Within this thesis, AES was applied to monitor the cleanliness of the silver samples. AES is very sensitive to small amounts of carbon and sulphur, which are characteristic contaminations of silver surfaces.

Chapter 4

Experimental Details

Well-defined experiments are only possible with polished silver single crystals showing a small miscut with respect to the (111) planes. The sample preparation and the experimental setup, which was used for the experiments performed at the different synchrotron light sources, is described in the following sections.

4.1 Sample Preparation

The silver samples have a disk like shape with a diameter of 10 mm. The samples were aligned by x-ray diffraction. The accuracy obtained by this method is on the order of 0.1° . After the alignment, the sample is lapped with Al_2O_3 suspensions in three steps, showing a grain size of 20, 9 and $3\ \mu\text{m}$. Afterwards, the Ag(111) samples are polished in three steps. First with a diamond polishing suspension with grain sizes of 3 and $1\ \mu\text{m}$. The final polishing step is performed with an Al_2O_3 suspension with a grain size of $0.05\ \mu\text{m}$.

The polishing procedure leads to a destruction of the crystallinity of the surface. The depth of this disordered layer is two to three times the grain size of the polishing grains used in the last step of the polishing procedure. Additionally, polishing grains are incorporated in the defective surface layer. The topmost silver layers were removed by an electrochemical polishing procedure, using a solution containing acetic acid, sulphuric acid, methanol and thiourea. This preparation results in an almost defect free Ag(111) surface.

The final cleaning procedure is performed under UHV conditions, applying repeated sputter and annealing cycles. The sample is sputtered by Argon ions with a kinetic energy of 0.5 to 1 keV. The sputtering procedure removes contaminations from the surface, but at the same time the crystallinity of the topmost silver layers is destroyed. The crystallinity of the sample surface is restored by an annealing cycle with a temperature well below the melting point. For Ag a temperature of 873 to 923 K is applied, which leads to a mobilisation of the silver atoms at the surface, leading to a recrystallisation of the topmost silver layers. The annealing of the sample may lead to

the segregation of contaminations from the bulk to the surface, which is controlled by AES. The sputter anneal cycles are repeated until the LEED image shows sharp spots and no impurities are visible in the AES spectra. This situation is shown in figure 4.1. Typical contaminations of silver surfaces are sulphur and carbon.

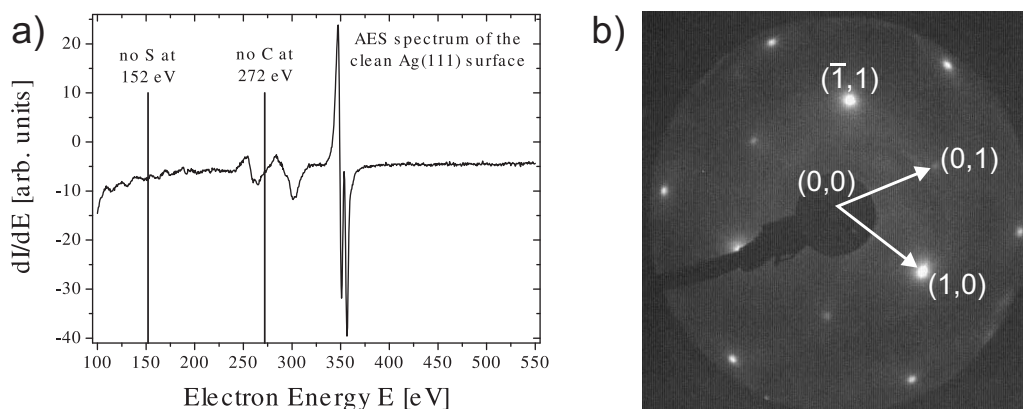


Figure 4.1: a) AES spectrum of the clean Ag(111) surface. No C or S impurities are present. b) LEED image of the clean Ag(111) surface recorded at an electron energy of 140 eV. The threefold symmetry of the Ag(111) surface is clearly visible.

The AES spectrum of the clean silver surface shows only the silver peaks at 260, 266, 301, 304, 351 and 356 eV [85]. Furthermore, no oxygen is present, which would show up as a line at ~ 500 eV.

The sputter anneal cycles are routinely performed in our home laboratory or in the UHV chambers used at the different synchrotron light sources. In the case of the SXRD experiments the clean Ag(111) sample is transferred to our mobile x-ray diffraction chamber. During the transfer the sample gets in contact with air for a short time and it is enough to heat the sample to 823 K at an oxygen pressure of 10^{-5} mbar to obtain a clean Ag(111) surface again.

During all oxidation experiments the sample was heated to 873 K in UHV to remove all oxygen species from the surface. The $p(4 \times 4)$ reconstruction decomposes for example at ~ 520 K under UHV conditions (cf. section 2.2.1). After the annealing cycle the surface is clean again and a new oxidation procedure can be performed.

4.2 Surface X-Ray Diffraction

The SXRD experiments were performed at the dedicated Max-Planck beamline at the 2.5 GeV synchrotron ANKA (Angströmquelle Karlsruhe) in Karlsruhe, Germany [37]. The beamline is located at a bending magnet, which produces the white x-ray beam. The beamline consists of optical components interconnected by evacuated flight tubes,

to reduce intensity losses due to air scattering of the x-rays. An engineering drawing of the beamline layout is shown in figure 4.2.

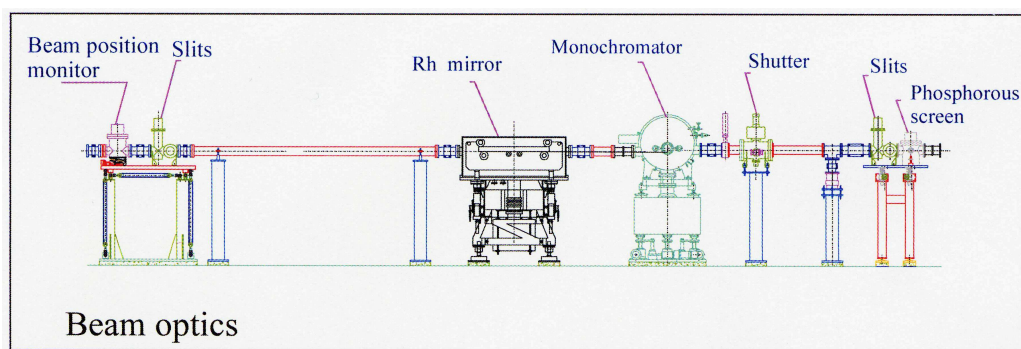


Figure 4.2: Beam optics of the dedicated Max-Planck beamline at the synchrotron ANKA.

The white x-ray beam hits a water cooled Rh coated Si mirror. The mirror can be bent allowing a vertical focussing of the x-ray beam. Furthermore, higher photon energies are cut off, due to total external reflection of the white x-ray beam. The IR and UV part of the light, emitted by the bending magnet, is absorbed by a water cooled Beryllium window in front of the double crystal monochromator. The monochromator is composed of two (111) cut silicon crystals. The energy E of the x-rays is selected by rotation of the crystals with respect to the incident beam, according to Bragg's law. A resolution $\Delta E/E = 3 \cdot 10^{-4}$ is obtained. The first crystal has to be water cooled for stable performance, due to the high power deposition of the white beam. The second monochromator crystal can be bent, allowing a strong horizontal focussing of the beam at the sample position. The measurements were performed at a photon energy of 10.5 keV. Accordingly, the cut-off energy at the mirror was selected to be ~ 16 keV, resulting in an effective suppression of higher harmonics at $\lambda/2$ and $\lambda/3$, which could pass the monochromator and falsify the experimental results. The beam size at the sample position is defined by a pair of horizontal and vertical slits and is typically 2×0.3 mm respectively. The intensity of the incoming monochromatised beam is monitored by an ionisation chamber. This allows a correction of the data acquisition time, since the incident beam intensity varies, due to variations of the electron beam current in the storage ring.

The Ag sample was mounted horizontally in our portable in-situ oxidation x-ray diffraction chamber. The whole chamber is then fixed to the diffractometer, which is shown in figure 4.3 a). The oxidation chamber is equipped with a gas system allowing operation from a base pressure on the order of 10^{-10} mbar up to an oxygen pressure of 2 bar. The x-rays enter and leave the chamber through a 2 mm thick freestanding beryllium window, allowing full access to reciprocal space for scattering in the surface

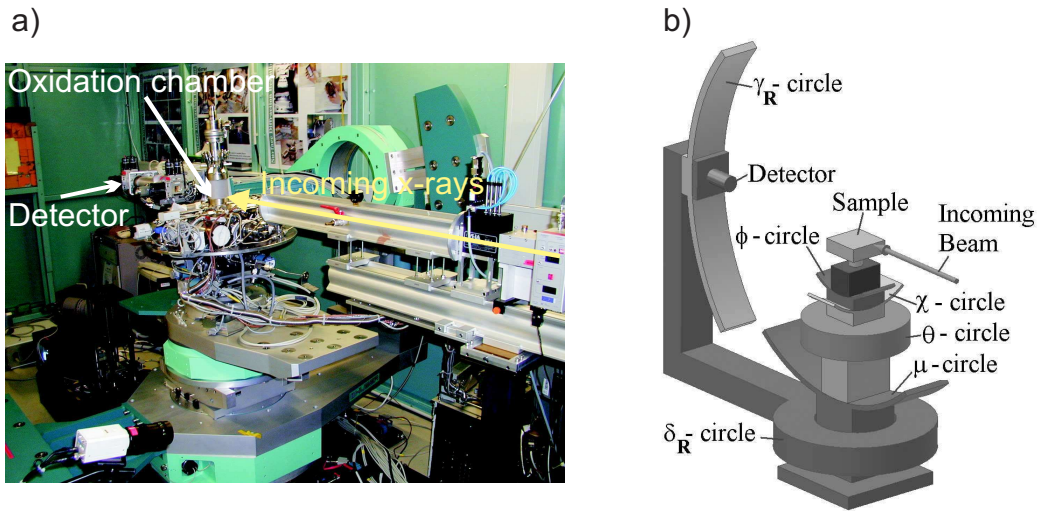


Figure 4.3: a) View in the experimental hutch at ANKA. The oxidation chamber is mounted on the diffractometer. b) Diffractometer setup used at ANKA.

plane. The scattered x-rays can leave the chamber up to an exit angle of $\sim 50^\circ$ for the case of out of plane scattering. The sample holder is connected to a heating station. The sample temperature can be varied between room temperature and ~ 1000 K. The temperature of the Ag surface is measured by a thermocouple, attached to the side of the Ag sample, with a precision of ± 5 K. The cleaning of the sample is performed by sputter-anneal cycles, with the sputter gun connected to the top of the chamber, as can be seen in figure 4.3 a).

The used diffractometer setup, shown in figure 4.3 b), resembles a six-circle diffractometer. Measurements were performed in z-axis mode with fixed incident angle. The whole diffractometer is mounted on a table to align it with respect to the incident beam. The differences between a normal z-axis diffractometer and the setup used at ANKA are described in [37]. The measurements were performed under grazing incidence with a fixed incident angle close to the critical angle of total external reflection, which results in an optimal signal to noise ratio. The angles χ and ϕ are used to align the surface normal parallel to the z-axis of the diffractometer. As the incident angle, defined by the angle μ , χ and ϕ are fixed during the experiment. The diffractometer is controlled by the software spec [86]. An orientation matrix is defined by the angular positions of all circles for at least two Bragg peaks. A properly defined orientation matrix allows scans in reciprocal space by moving the motors θ , δ and γ of the diffractometer. θ turns the crystal around the surface normal, until the selected scattering planes are in the correct position with respect to the incident beam. The motors δ and γ move the detector in and perpendicular to the surface plane, until the chosen momentum transfer is set. Finally, the x-rays are detected with a scintillation point detector, which is equipped with

detector slits, to define the angular acceptance of the detector.

4.3 High Resolution Core Level Spectroscopy

The HRCLS experiments were performed at beamline I311 at the 1.5 GeV synchrotron MAX II at MAX-lab in Lund, Sweden. The VUV and soft x-ray radiation is produced by an undulator. Several mirrors are used to focus the radiation on the sample position. A detailed description of the optical layout can be found in [38]. The heart of the beamline is a plane-grating monochromator. Photon energies from 30 to 1500 eV can be used. The monochromator resolution varies from 4 meV at 30 eV photon energy to 1.4 eV at 1500 eV. The beamline is shown in figure 4.4 a).

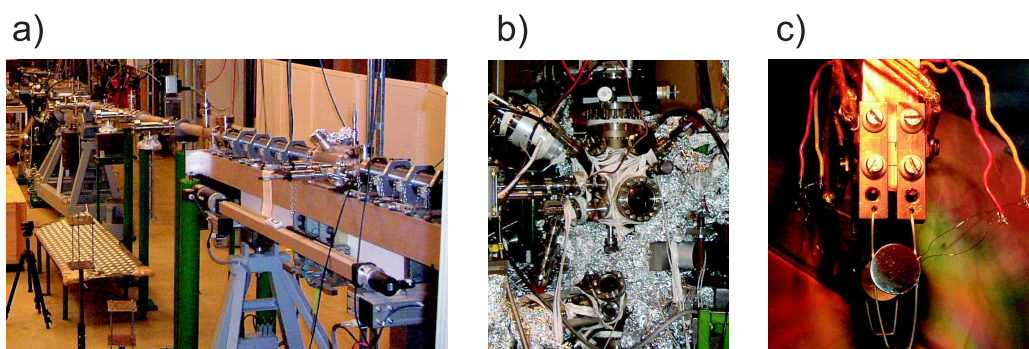


Figure 4.4: a) Beamline I311 at MAX-lab. b) Experimental end station of beamline I311. c) Ag(111) sample fixed by a tungsten wire, in front of the LEED system. The thermocouple is attached to the side of the sample.

The experimental end station, shown in figure 4.4 b), is build up by two UHV chambers which are connected by a valve. The preparation chamber, containing a LEED system, a sputter gun and the gas system is located on top of the analysis chamber. The analysis chamber is equipped with a high resolution hemispherical electron energy analyser [39] for the photoelectron spectroscopy measurements. A base pressure on the order of 10^{-11} mbar is routinely obtained in the analysis chamber. The sample is mounted by a tungsten wire to the vertical transfer rod, allowing a transfer of the sample from the preparation chamber to the analysis chamber. The sample holder is shown in figure 4.4 c). The sample is cooled by a liquid nitrogen reservoir inside the transfer rod, connected to the tungsten wire by a copper block, visible in the upper part of figure 4.4 c). The sample is directly heated by an electric current, flowing through the tungsten wire. The HRCLS measurements are performed at a sample temperature of ~ 100 K, to minimise contributions to the line width, due to phonons.

4.4 Normal Incidence X-Ray Standing Wave Absorption

The NIXSW experiments were performed at beamline ID32 at the 6 GeV synchrotron ESRF (European Synchrotron Radiation Facility) in Grenoble, France. Beamline ID32 is equipped with three undulators, which can be used at the same time, depending on the desired photon energy. The design of the beam optics is similar to the MPI beamline at ANKA. The white beam is monochromatised by a double crystal monochromator, whereas the first crystal is cooled by liquid nitrogen. A detailed description of the beamline layout can be found in [40]. During the NIXSW measurements the XSW chamber is connected windowlessly to the storage ring vacuum by evacuated flight tubes. This is indispensable due to the low photon energy used for the NIXSW measurements, which is on the order of 2.6 keV. The incident photon flux is monitored by a metallic mesh in front of the XSW chamber. This allows a normalisation of the measured standing wave profiles. The XSW chamber is shown in figure 4.5 a).

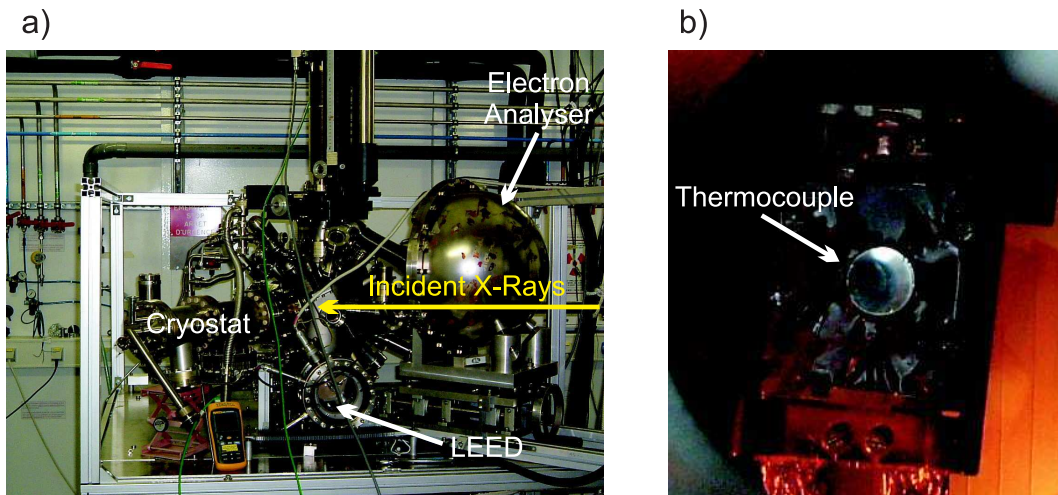


Figure 4.5: a) XSW chamber at beamline ID32 at the ESRF. b) Sample holder with Ag(111) sample inside the XSW chamber.

The XSW chamber is operated at a base pressure on the order of 10^{-10} mbar. It is equipped with the standard tools of surface science: a LEED system, a sputter gun and a gas system for sample preparation and characterisation. The sample holder, shown in figure 4.5 b) is connected by a copper netting to a cryostat, cooled by liquid nitrogen. The sample temperature is raised by a filament heater. The sample temperature is measured by a thermocouple fixed to the side of the silver sample. NIXSW measurements were performed at a sample temperature of ~ 120 K. The chamber is equipped with a hemispherical electron energy analyser, to measure the photoelectron spectra during

the XSW measurements. The backscattered x-ray signal is detected by a photodiode inside the UHV chamber.

Chapter 5

Structure of O-p(4×4)/Ag(111)

The structural model of the oxygen induced p(4×4) reconstruction O-p(4×4)/Ag(111) will be discussed in this chapter. A new model was developed by a collaborative work combining results from SXRD, STM, HRCLS and NIXSW measurements and DFT calculations [19]. In this chapter we will focus on our results obtained by in-situ SXRD, HRCLS and NIXSW. At first, the preparation procedure of the p(4×4) reconstruction by O₂ and NO₂ is presented. In the following it will be shown, that previously proposed models of the p(4×4) structure can be ruled out by our SXRD results. The new model of O-p(4×4)/Ag(111) is discussed in detail and finally the stability diagram of the O/Ag(111)-system, as determined by our in-situ SXRD measurements, is presented.

5.1 Preparation by O₂ and NO₂

The preparation of the p(4×4) reconstruction by molecular oxygen was optimized by means of in-situ SXRD measurements. For this purpose a strong in-plane reflection of the p(4×4) reconstruction was measured as a reference in dependency of sample temperature and oxygen pressure.

The integrated intensity of the reference scan is proportional to the coverage of the surface with the p(4×4) reconstruction, whereas the width of the scan is a measure of the mosaicity of the layer. The optimal preparation conditions result in a maximum of the integrated intensity at a minimal width of the rocking scan. In a first step the temperature was varied at an oxygen pressure of 2 mbar, showing an ideal growth temperature of 553 K. The effect of a stepwise increase of the oxygen pressure at a temperature of 553 K on the integrated intensity of the reference scan is shown in figure 5.1. A saturation of the signal was observed for oxygen pressures higher than 100 mbar, which means, that almost the whole surface is covered by the p(4×4) reconstruction. At an oxygen pressure of 200 mbar the reference scan showed a minimal full width at half maximum (FWHM) of 0.32 °. A more detailed view on the initial growth of the p(4×4) reconstruction is given by the sequence of reference scans measured between 1 and 10 mbar at 553 K, shown in the inset of figure 5.1. At an oxygen pressure of 1

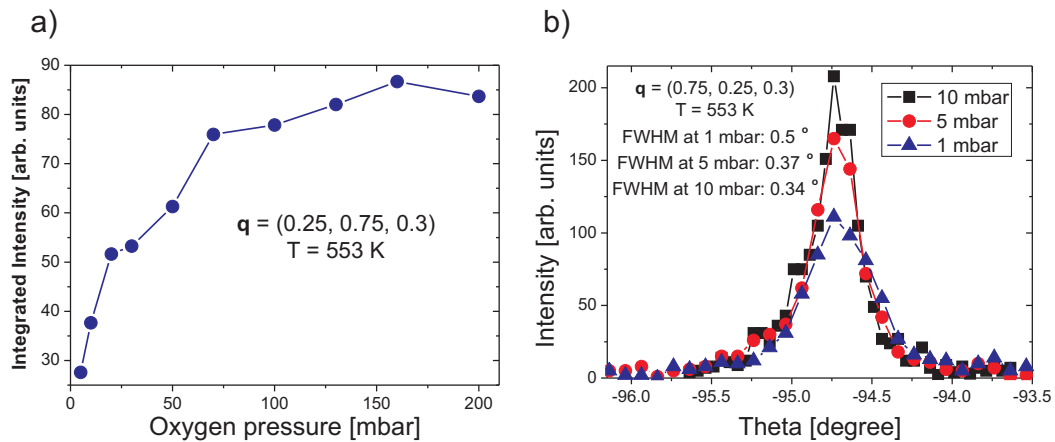


Figure 5.1: Evolution of the integrated intensity of a strong in-plane reflection of the $p(4\times 4)$ reconstruction at a q -value of $(0.25, 0.75, 0.3)$ for increasing oxygen pressure. A saturation of the signal was observed for pressures higher than 100 mbar. b) Sequence of rocking scans measured at $(0.75, 0.25, 0.3)$ for an oxygen pressure between 1 and 10 mbar and a temperature of 553 K. The growth of the $p(4\times 4)$ reconstruction with increasing oxygen pressure is accompanied by a reduction of the mosaicity of the domains.

mbar the $p(4\times 4)$ reconstruction starts to form, showing a mosaicity of 0.5° . This value has to be compared with the one of the substrate of 0.27° . Initially, small islands of the $p(4\times 4)$ reconstruction are formed, which show a mosaicity almost twice as large as the one of the substrate. The small size of the domains at the initial stage of the growth results in a rather loose alignment of the islands of the $p(4\times 4)$ reconstruction. With increasing oxygen pressure the size of the domains is increased, which is reflected in a large reduction of the mosaicity to 0.34° at 10 mbar, reaching almost the lowest value of 0.32° , which was observed at 200 mbar of oxygen. According to this, the mosaicity of the $p(4\times 4)$ reconstruction is limited by the perfection of the substrate. The small difference between the mosaicities of the substrate and the $p(4\times 4)$ reconstruction is in line with STM measurements, where domain sizes of the $p(4\times 4)$ reconstruction of hundreds of nanometers were observed [19].

The $p(4\times 4)$ reconstruction can be either prepared by O_2 , as already described, or by dosing NO_2 at temperatures around 500 K. The crucial question, which had to be solved, is, if the structure of the $p(4\times 4)$ reconstruction is independent of the oxidation procedure? The preparation by NO_2 was introduced in [12]. NO_2 decomposes into NO and O on the $Ag(111)$ surface and under appropriate conditions NO desorbs, resulting in a sufficient high coverage of atomic oxygen to form the $p(4\times 4)$ structure. This method has the advantage, that the $p(4\times 4)$ reconstruction can be grown in a standard UHV chamber, because a NO_2 pressure on the order of only 10^{-6} mbar has to be

applied. This preparation recipe was used for all STM measurements [15, 19, 42] and for our HRCLS and NIXSW measurements. The preparation with O_2 is carried out at oxygen pressures of at least 1 mbar, due to the low dissociative sticking probability of 10^{-6} for molecular oxygen on Ag(111) [12]. For our in-situ SXRD measurements we have used molecular oxygen, since it is used for the industrial applications of silver as a catalyst.

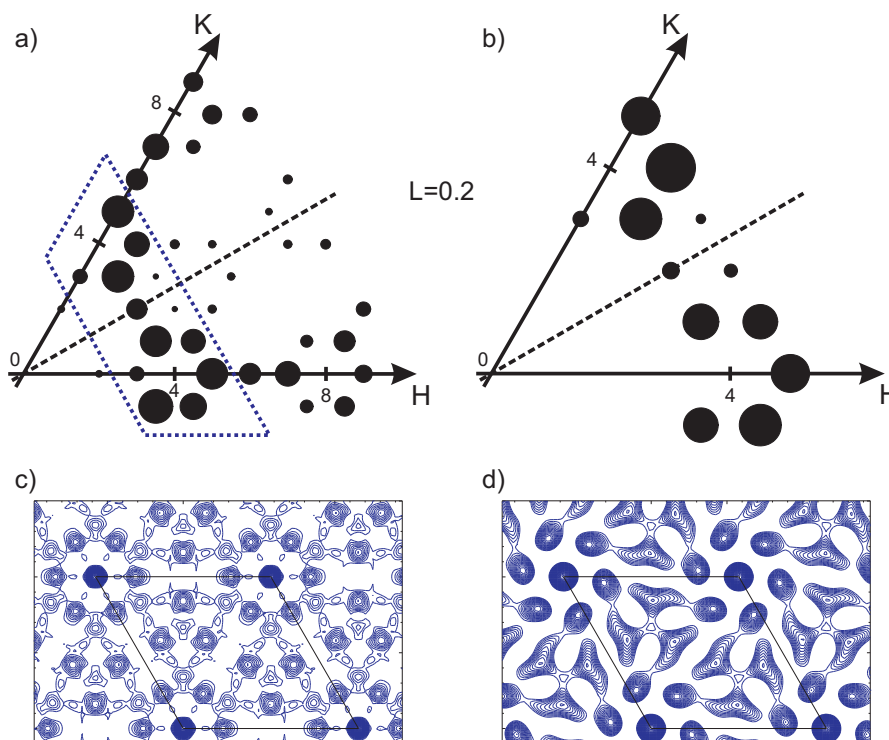


Figure 5.2: a) in-plane data set; preparation with O_2 . H and K values are given in units of the $p(4 \times 4)$ unit cell. The dashed line marks the mirror plane of the observed $p6mm$ symmetry. The box marked by the dotted line is the range in which the measurements for the case of the preparation with NO_2 were performed. b) in-plane data set; preparation with NO_2 . c) Patterson function calculated from the in-plane structure factors obtained with O_2 . The $p(4 \times 4)$ unit cell is marked by the black line. d) Patterson function for the case of the NO_2 preparation.

For the purpose of comparison, we used both preparation methods and measured the in-plane structure factors. For the preparation with NO_2 we have dosed 600 Langmuir NO_2 at a temperature of 500 K. The data set was measured at 300 K and under UHV conditions. In the other case, the $p(4 \times 4)$ structure was prepared by dosing 200 mbar of oxygen for 30 minutes at 553 K and maintaining 5 mbar of oxygen during the measurements, which were performed at 300 K. The in-plane structure factors for

the O₂ preparation are shown in figure 5.2 a). The dashed line marks the mirror plane of the observed p6mm symmetry. The box marked by the dotted line is the range of q-values for which the in-plane structure factors for the case of the NO₂ preparation were measured, which are shown in figure 5.2 b). A fast decomposition of the p(4×4) reconstruction prepared by NO₂ during the experiment prevented a measurement of the complete in-plane data set and explains the observed differences in the structure factors. Nevertheless, both data sets show the same symmetry and the same features. Further confirmation for this observation is given by the Patterson functions [62] shown in figure 5.2 c) and d), which were calculated from the in-plane structure factors, using only the superstructure reflections. The Patterson function $P(X, Y)$

$$P(X, Y) = \frac{1}{A_{ab}} \sum_{HK} |F_{HK0}|^2 \cos 2\pi \left(H \frac{X}{a} + K \frac{Y}{b} \right) \quad (5.1)$$

is an auto correlation function of the electron density projected onto the surface (cf. section 3.1.1). The Patterson function is a function in real space and a maximum at (x_0, y_0) means, that there is a vector (x_0, y_0) between two atoms in the surface unit cell, or a sum / difference of vectors. Both Patterson functions show the same main maxima and the one obtained for the preparation with NO₂ shows fewer details, since the structure factors with large in-plane momentum transfer were not measured in this case. Finally, we could show, that the structure of the p(4×4) reconstruction is independent of the oxidation procedure.

For the HRCLS and NIXSW measurements an oxidation and annealing cycle was used to prepare the p(4×4) structure. In the first step the clean Ag(111) sample was oxidized by 600 L NO₂ ($5 \cdot 10^{-7}$ mbar NO₂ for 20 minutes) at a sample temperature of 500 K. Afterwards, the sample was cooled down to ~ 100 K, maintaining the NO₂ pressure until 300 K. At 300 K the NO₂ is pumped down, restoring UHV conditions. Examination of the sample by LEED results in a faint (1×1) pattern, shown in figure 5.3 a). The corresponding O 1s HRCLS spectrum is shown in figure 5.3 b). The O 1s spectrum can be decomposed by three components: the p(4×4) reconstruction shows up at binding energy of 528.1 eV, the component at 530.0 eV is attributed to chemisorbed oxygen [14] and the component 531.3 eV is related to the presence of NO on the surface [12]. At 500 K NO₂ decomposes into NO and O on the Ag(111) surface. At this temperature NO desorbs and above 420 K chemisorbed atomic oxygen transforms into the p(4×4) reconstruction [14]. Under these conditions small islands of the p(4×4) structure are formed, which is shown in the first part of figure 5.3 c). Cooling down to 300 K under NO₂ atmosphere leads to the adsorption of NO and O in between the small islands of the p(4×4) reconstruction, resulting in the faint LEED pattern and the already discussed O 1s spectrum. Heating under UHV conditions to 500 K leads to the desorption of NO and the chemisorbed oxygen is transformed into the p(4×4) reconstruction, which is shown in figure 5.3 c). Correspondingly, the typical LEED pattern of the p(4×4) reconstruction can be observed and is shown in figure 5.3 d). The (0,0) reflection is visible below the shadow of the electron gun, since the silver

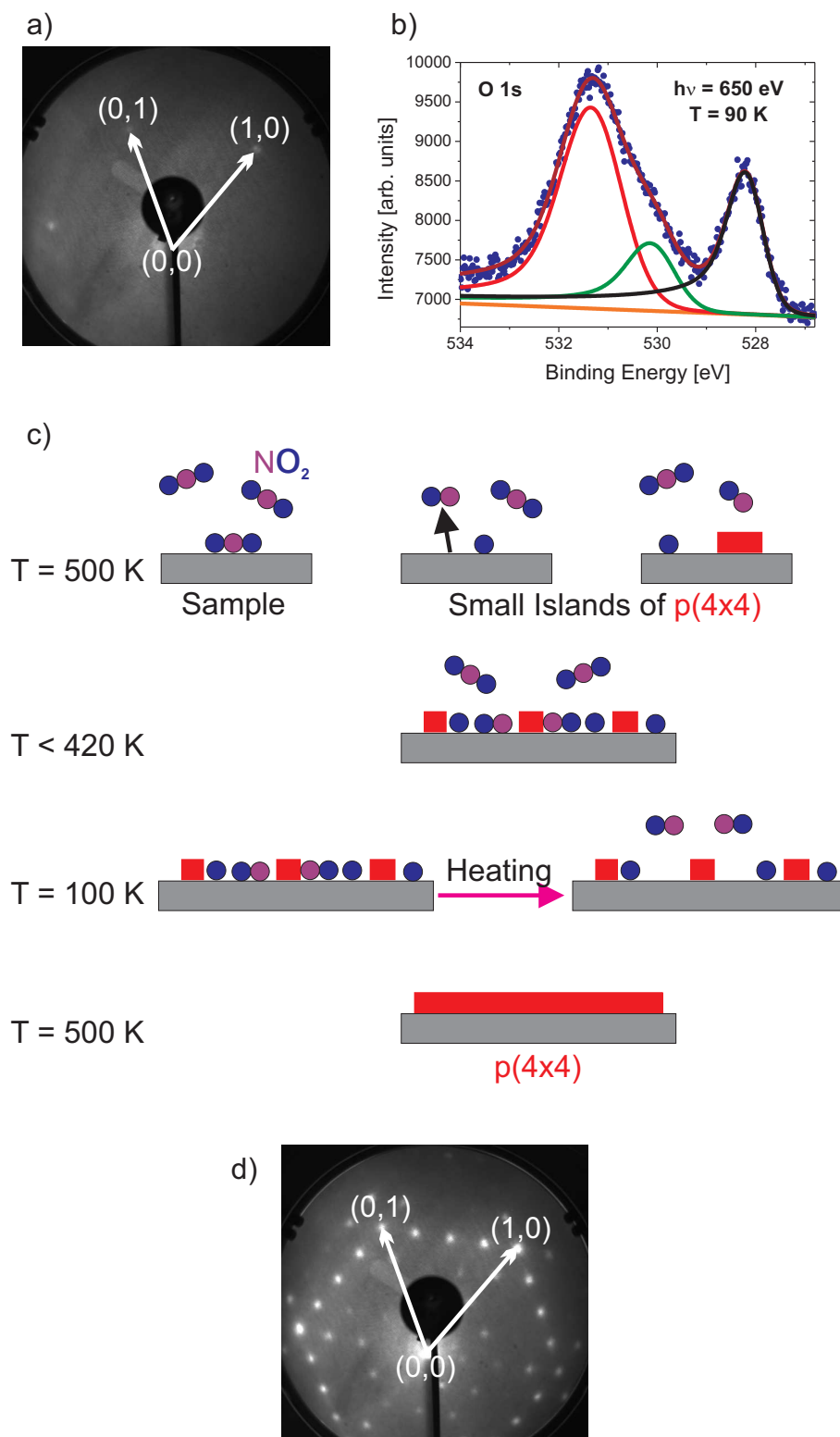


Figure 5.3: a) LEED image of the Ag(111) surface after oxidizing with 600 L NO_2 with subsequent cooling to ~ 100 K. b) Decomposed O 1s spectrum of the oxidized Ag(111) surface, as shown in a). c) Sketch of the oxidation procedure with NO_2 . d) LEED image of the $p(4 \times 4)$ reconstruction after complete oxidation procedure as described in c). Details to this figure are explained in the text.

sample was slightly tilted during the measurements. The O 1s spectrum of the p(4×4) reconstruction, showing only one component at a binding energy of 528.2 eV, is plotted in figure 5.10 b).

5.2 Decomposition of the p(4×4) reconstruction

The SXRD data set of the p(4×4) reconstruction, consisting of CTRs, superstructure rods and in-plane structure factors, was measured after a fresh preparation of the p(4×4) structure at 200 mbar of oxygen and 553 K for 30 minutes. The measurements were performed at 300 K and 5 mbar of oxygen. The elevated oxygen pressure prevents a fast decomposition of the p(4×4) structure during the measurements. Nevertheless, a reduction of the p(4×4) reconstruction was observed, which is attributed to reactions of the p(4×4) structure with reducing gases, like CO or H₂. The decomposition of the p(4×4) reconstruction was monitored by measuring a reference scan at (0.25, 0.75, 0.2) in between the rod measurements.

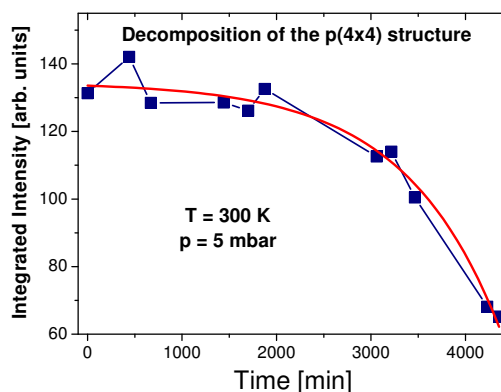


Figure 5.4: Evolution of the integrated intensity of a reference scan at $q = (0.25, 0.75, 0.2)$ measured at 300 K and 5 mbar of oxygen. The reduction of the signal of the p(4×4) reconstruction can be described by an exponentially increasing decomposition.

The evolution of the integrated intensity of the reference scan, which is proportional to the coverage of the Ag(111) surface with the p(4×4) structure, is shown in figure 5.4. The decomposition of the p(4×4) reconstruction increases exponentially and can be described by using the relation $I = I_0 - e^{t/\tau}$ for the integrated intensity (Fit results: $I_0 = 135$ and $\tau = 1017$ min). After a fresh preparation almost the whole surface is covered by the p(4×4) reconstruction, exhibiting only few defects. We suggest, that the

reduction of the $p(4\times 4)$ reconstruction by reducing gases is only possible at defect sites at room temperature. In the early stage of the decomposition the reduction events are restricted to domain boundaries, step edges and to the few defects within the domains. Every reduction step creates a new defect, which explains the observed exponential decomposition behaviour.

The square root of the integrated intensity is proportional to the amplitude of the structure factor, so a correction of the data set is straightforward. The corrections were applied to the in-plane data set and to the superstructure rods, since their signal is only caused by scattering from atoms of the $p(4\times 4)$ reconstruction. The measured CTRs cannot be corrected for the decomposition of the $p(4\times 4)$ reconstruction, because the signal of the CTRs is caused by a coherent superposition of scattered intensity from the bulk and from the reconstructed surface. The CTRs were measured in the plateau region visible in figure 5.4 for $t < 2400$ min, so the missing correction of the CTRs has a negligible influence on the results and is taken into account by the error bars.

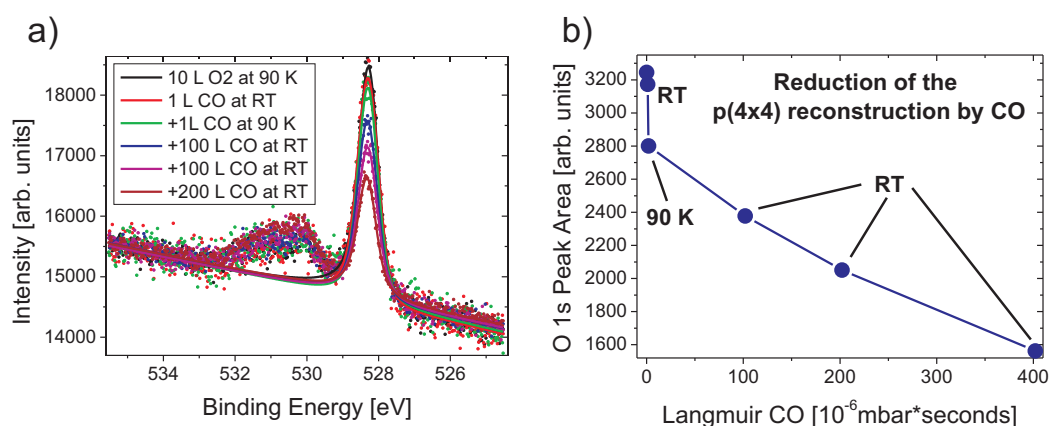


Figure 5.5: a) Evolution of O 1s spectra of the $p(4\times 4)$ reconstruction under CO dosage. b) Fitted peak area of the O 1s component of the $p(4\times 4)$ structure in dependency of CO coverage.

The ability of CO to reduce the $p(4\times 4)$ reconstruction was verified by a sequence of HRCLS measurements, shown in figure 5.5 a). The $p(4\times 4)$ structure was prepared by the recipe described in section 5.1. Some residual contaminations by O and NO are visible in the O 1s spectrum and show binding energies of 530 and 531 eV respectively. At first the $p(4\times 4)$ reconstruction was additionally oxidized by 10 L of O₂, which had no effect on the O 1s spectrum. Subsequently, CO was dosed in 5 steps up to a total coverage of 402 L. A strong reduction of the signal of the $p(4\times 4)$ is visible upon the CO treatment. All spectra are shown in figure 5.5 a), for the sake of simplicity only the fitted components of the $p(4\times 4)$ structure are plotted. The fitted peak area is shown in figure 5.5 b), showing a strong decrease after dosing 2 L of CO. This is attributed to

the decomposition of small islands of the p(4×4) reconstruction in the beginning of the CO treatment. Further CO dosage leads to a rather linear reduction of the O 1s signal of the p(4×4) structure. Additionally, we have measured the C 1s spectrum during the CO treatment. No peak was observed in the C 1s spectra. This implies, that CO reacts with oxygen atoms from the p(4×4) reconstruction and leaves the Ag(111) surface as CO₂. Finally, we could show, that the CO fraction in the residual gas can explain the decomposition of the p(4×4) reconstruction during our SXRD measurements.

5.3 Comparison with previously discussed Models

The structure of Ag(111)-p(4×4)-O, which was made responsible for the catalytic activity of silver regarding the epoxidation of ethylene [16, 22], seemed to be solved by a combination of STM measurements, STM image simulations and DFT calculations [15, 16, 18, 50]. The models, which were proposed, are based on a three-layer slab of the bulk oxide Ag₂O in (111) orientation, rotated by 30° relative to the Ag(111) surface normal, resulting in an O-Ag-O trilayer, as it was put forward by LEED and XPS measurements [10, 11]. The Ag₁₁O₆ model (referred to as 'Ag_{1.83}O' model in [15]), which was optimized by means of DFT calculations [16], is shown in figure 5.6 a) and consists of hexagonal O-Ag-rings, which are build up by straight O-Ag-O blocks. Compared to a pristine Ag₂O(111) trilayer every third Ag atom within the O-Ag-rings is missing.

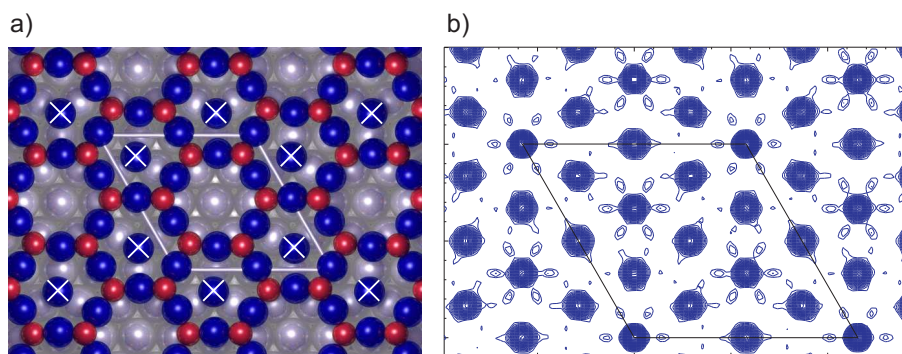


Figure 5.6: a) Two structural models of the p(4×4) reconstruction. Blue (large) spheres represent Ag atoms within the oxide layer, whereas the oxygen atoms are shown as red (small) spheres. The Ag₁₁O₆ model of the p(4×4) structure comprises all shown atoms. In the case of the Ag₉O₆ model the central Ag atoms, marked by the crosses, are omitted. b) Patterson function of the Ag₁₁O₆ model, computed from the calculated in-plane structure factors of the Ag₁₁O₆ model, using only the superstructure reflections.

Further investigation of the Ag₁₁O₆ model by means of DFT revealed, that remov-

ing all Ag atoms within the O-Ag-rings results in a model with Ag_9O_6 stoichiometry (referred to as 'Ag_{1.33}O' model in [18]), which is energetically more favourable than the formerly proposed structure [18]. The silver atoms, which were removed from the Ag_{11}O_6 model are marked by the crosses in figure 5.6 a).

The Patterson function of the Ag_{11}O_6 structure, plotted in figure 5.6 b), shows a completely different behaviour than the one which was calculated from our in-plane data set shown in figure 5.2 c). The same is true for the Patterson function of the Ag_9O_6 model, showing exactly the same features as figure 5.6 b). The position of the maxima of the Patterson function for the case of the Ag_{11}O_6 model coincide with the position of the Ag atoms within the unit cell, besides the maximum in the centre of the unit cell. This observation can be explained by a so-called 'Heavy Atom Approach' [63]. For the calculation of the Patterson function the structure factor is used, as can be seen in equation 5.1. The structure factor is proportional to the atomic form factor, which is much higher for silver atoms than for oxygen atoms, due to the big difference in the atomic number of the two elements. In this approach Ag atoms are located at the positions of the strongest maxima of the Patterson function. The difference in the Patterson functions is a strong indication, that the hitherto discussed models of the p(4×4) reconstruction are not correct, which will be corroborated by a comparison of structure factors of the Ag_{11}O_6 model with our SXRD data set, shown in figure 5.8.

5.4 Structural Model of O-p(4×4)/Ag(111)

The 'Heavy Atom Approach' was used for the determination of a new model of the p(4×4) reconstruction. Placing silver atoms at the positions of the strongest maxima of the Patterson function, leads to a Ag-Adatom-Trimer model, shown in figure 5.7 b). The model is built up by two Ag trimers, whereas one half of the Ag atoms occupy fcc sites and the others are located on hcp sites. This model is a part of the Ag_{12}O_6 model proposed on the basis of STM measurements, shown in figure 5.7 b) [19]. The number of Ag atoms per (4×4) unit cell was determined, by reducing the p(4×4) structure by CO. The reduced surface was probed by STM, resulting in 12 ± 1 Ag atoms per (4×4) unit cell (A more detailed description of this experimental approach can be found in [19].). The most prominent feature of the STM images of the p(4×4) reconstruction, besides the imaged honeycomb structure, are up to ~ 2 Å deep 'corner holes' [15, 19, 20]. The only physically reasonable possibility to arrange 12 atoms in the (4×4) cell results in 2 closely packed Ag_6 triangles located on fcc and hcp sites respectively. This structure shows free area at the origin of the unit cell, which can explain the observed corner holes. The position of the oxygen atoms was determined by DFT calculations [19,20]. Each pair of Ag_6 triangles is connected by 2 oxygen atoms, which are located in the furrows between the silver adatoms, resulting in 6 oxygen atoms per unit cell. All interatomic distances within the p(4×4) reconstruction, as determined by the Patterson function shown in figure 5.7 a), are reproduced by the Ag_{12}O_6 model.

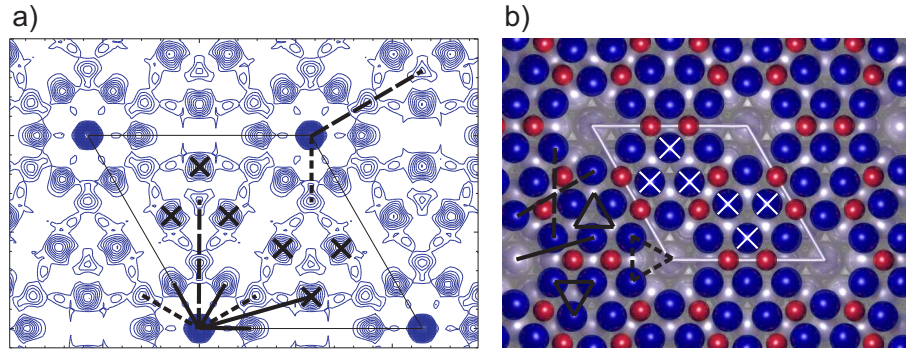


Figure 5.7: a) Patterson function calculated from the in-plane superstructure reflections. The strongest maxima, which are used for the 'Heavy Atom Approach' are marked by crosses. All relevant vectors connecting the maxima of the Patterson function and the origin of the unit cell are marked by the dashed and solid lines. b) Structural models of the p(4×4) structure. Blue (large) spheres represent Ag atoms, whereas the oxygen atoms are shown as red (small) spheres. Ag-Adatom-Trimer model, built up by the Ag atoms marked by crosses and Ag_{12}O_6 model containing all shown atoms. All interatomic distances arising from the Patterson function, marked by the corresponding lines, are in agreement with the Ag_{12}O_6 structure.

The corresponding distances are marked in figure 5.7 b). Not all interatomic distances occurring in the first substrate layer are visible in the Patterson function calculated from our in-plane data set. This can be explained by the fact, that the in-plane structure factors of the CTRs were not used for the calculation, since the signal on the CTRs is a coherent superposition of scattered intensities from the bulk and the reconstructed surface. The missing Fourier components lead to the absence of some maxima of the Patterson function corresponding to interatomic distances in the first substrate layer.

The complete set of measured structure factors of the p(4×4) reconstruction is shown in figure 5.8. The first result of our SXRD measurements is, that all previous models of the p(4×4) structure from [15, 18, 50] can be ruled out. As an example, the calculated structure factors of the Ag_{11}O_6 model are compared with the measured in-plane data and the superstructure rods, shown in figure 5.8 a) and b). The model cannot describe our SXRD measurements and further relaxation of the model leads to unphysical structures.

DFT calculations, obtained at 0 K, revealed an energy gain of 0.2 eV per (4×4) cell, if the p6mm symmetry of the Ag_{12}O_6 model is broken [19]. The energetic most favourable structure, shows small rotations of the Ag_6 triangles in the surface plane. The clockwise and counterclockwise movement of the Ag_6 triangles leads to an alternating up and down movement of the oxygen atoms in the furrows. Our SXRD measurements are in good agreement with the Ag_{12}O_6 structure and in a first step both rotational orientations of the Ag_6 triangles were used with equivalent probability to

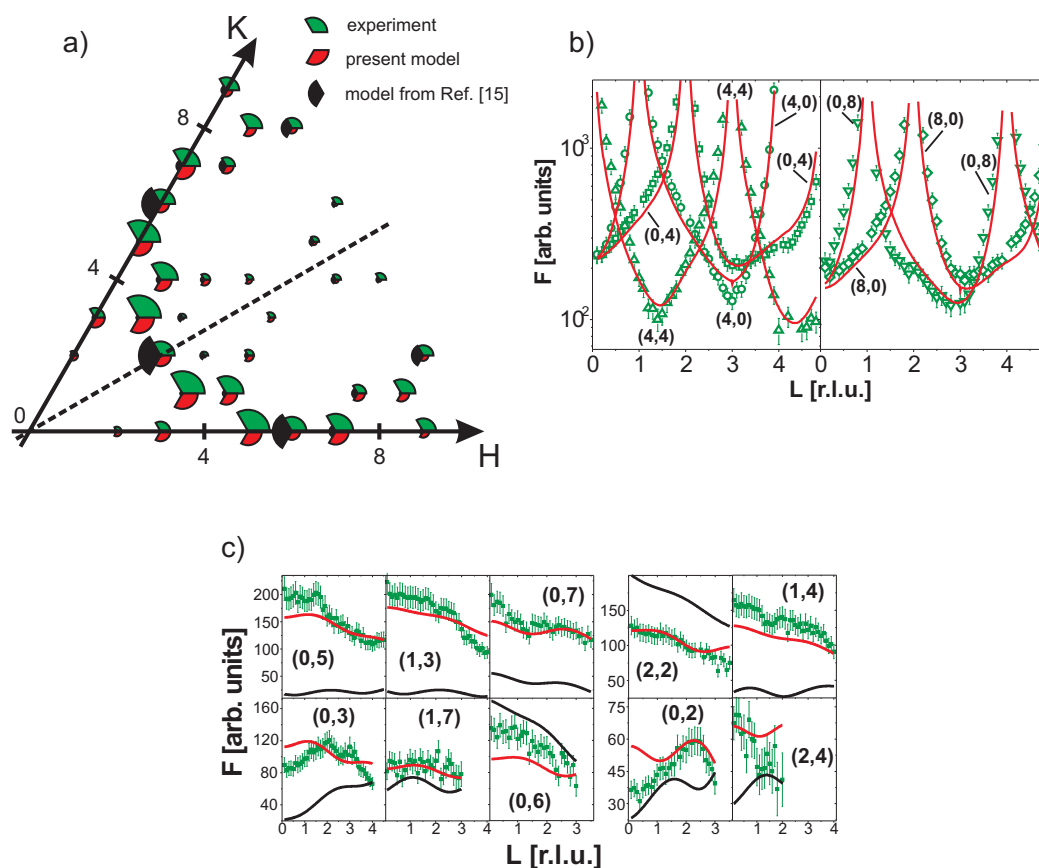


Figure 5.8: Experimental and calculated structure factors. a) In-plane structure factors measured at $L = 0.2$, b) crystal truncation rods and c) surface rods of the $p(4 \times 4)$ reconstruction. q -values are given in reciprocal lattice units (r.l.u.) of the (4×4) cell. The shown error bars are a combination of statistical and systematic errors.

calculate the structure factors, whereas $p3m1$ symmetry was applied. The result of the fit is a vanishing rotation of the Ag_6 triangles, giving rise to a similar height of the oxygen atoms in the furrows. *Ab initio* Molecular Dynamics (MD) simulations showed, that the $Ag_{12}O_6$ structure is rather soft, resulting in a very small energy barrier between the two rotational configurations [19]. This is in agreement with the large vibrational amplitudes of the Ag_6 triangles obtained from the SXR D refinement with $p3m1$ symmetry. The SXR D measurements were performed at 300 K, so the mean position between the two rotational configurations was probed. For the final fit to our data set $p6mm$ symmetry was used for the adatoms and the first substrate layer, resulting in 13 independent positional fit parameters, thereof 5 in-plane positional parameters and 1 z displacement parameter for the second substrate layer. The fit was performed simultaneously to all in-plane data, superstructure rods and CTRs, giving a total of 576

data points.

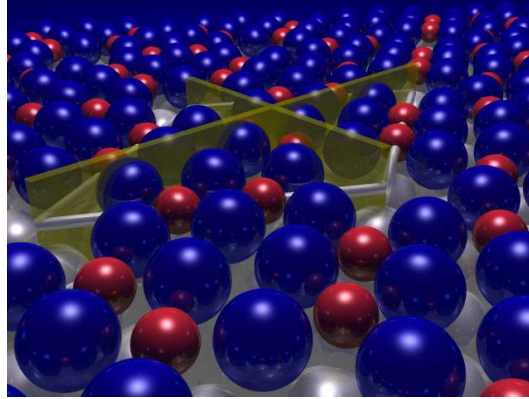


Figure 5.9: Ag_{12}O_6 model of the $p(4\times 4)$ reconstruction, as determined by our SXR D fit using $p6mm$ symmetry. The mirror planes of the $p6mm$ symmetry are marked by the yellow planes.

The in-plane data set, used for the final fit, was symmetrised according to $p6mm$ symmetry. The coverage of the $\text{Ag}(111)$ surface with the $p(4\times 4)$ structure, was used as a fit parameter, giving a result of 80 %. The result of the fit, shown in figure 5.8, is $\chi^2 = 3.7$ ($\chi^2 = 2.6$ for the in-plane data), showing a reasonable agreement with our measurements. One scale factor was used for the in-plane structure factors and the surface rods, leading to a systematic offset for the calculated in-plane data, due to the decomposition of the $p(4\times 4)$ reconstruction during the measurements of the superstructure rods. The effect of the decomposition is also visible on the superstructure rods, since the shape of almost all calculated rods reproduces the measurements and only an offset between measurement and calculation is observed, as for the $(0, 6)$ and the $(1, 4)$ rod. In the case of the CTRs a remarkably good agreement between experiment and calculation is obtained. The signal on the CTRs is very sensitive to the amount of silver atoms in the unit cell and to their position, giving a strong support for the proposed Ag_{12}O_6 structure, which also agrees with a study including STM measurements and DFT calculations [20]. The rotational averaged structure of the $p(4\times 4)$ reconstruction, which was probed by our SXR D measurements, results in a planar arrangement of the oxygen atoms. The structural model obtained from the SXR D fit is shown in figure 5.7 b) and figure 5.9. Other O arrangements were also checked by means of DFT, but none of them is energetically favourable, especially the formation of subsurface oxygen atoms below the Ag_6 triangles can be ruled out [19]. A lifting of the Ag_6 triangles due to subsurface oxygen can also be excluded by our SXR D measurements, which would lead to a completely different shape of the CTRs.

Further confirmation for the Ag_{12}O_6 model comes from our HRCLS measurements. The main results are shown in figure 5.10. The $\text{Ag } 3d_{5/2}$ spectrum can be decomposed

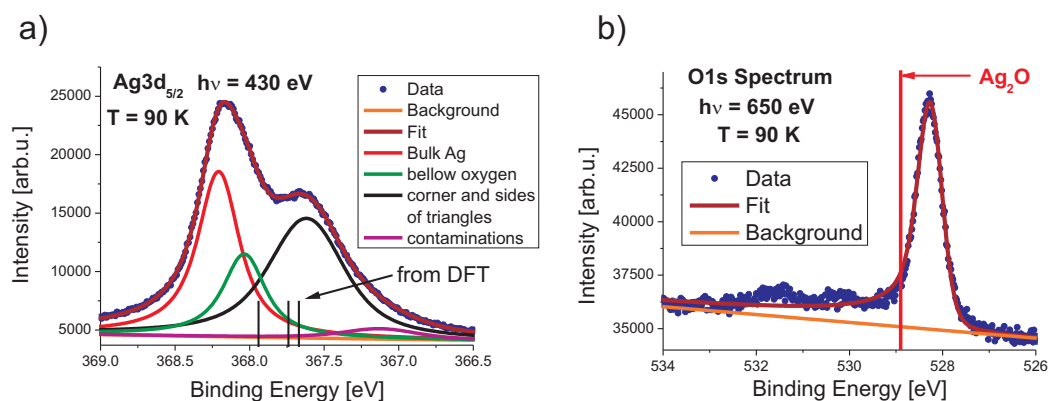


Figure 5.10: a) Decomposition of the Ag $3d_{5/2}$ spectrum, in presence of the p(4×4) reconstruction. b) O 1s spectrum of the p(4×4) reconstruction. The O 1s binding energy of the bulk oxide Ag_2O is labelled by the red line.

using four components, showing the following binding energies: bulk Ag has a binding energy of 368.2 eV, silver atoms in the furrows below the oxygen atoms show a binding energy of 368.0 eV, silver atoms in the Ag_6 triangles have a binding energy of 367.6 eV and the small component at 367.1 eV is attributed to contaminations due to NO and O on the surface. This assignment is in agreement with core level shifts calculated from the model, as determined by DFT calculations [19]. The calculated binding energies are shown as black lines in figure 5.10 a). The splitting of the binding energy of the corner and side atoms of the Ag_6 triangles cannot be resolved experimentally. Our HRCLS measurement of the Ag $3d_{5/2}$ spectrum was the first study, where the surface contribution of the p(4×4) reconstruction could be completely resolved. Interestingly, the binding energies of the Ag $3d_{5/2}$ surface components are shifted to lower values, which is a rather unexpected behaviour for an oxidized system. Normally, oxygen atoms attract a part of the charge of the metal atoms, due to their high electronegativity, resulting in a less screened metal atomic core, giving rise to a higher binding energy of the core electrons of the metal atoms. This observation is still not completely understood and is also observed in XPS measurements of the bulk oxide Ag_2O [49]. The O 1s spectrum of the p(4×4) reconstruction, plotted in figure 5.10 b), shows only a single nonbroadened peak at a binding energy of 528.2 eV. This observation is in agreement with several XPS studies [11, 12, 14]. This is also consistent with the proposed $Ag_{12}O_6$ model, which bears no resemblance to Ag_2O , showing an O 1s binding energy of 528.9 eV [49]. For comparison, the O 1s binding energy of Ag_2O is shown in figure 5.10 b) by the red line. DFT calculations give a similar result for the binding energy of the O 1s spectrum [19]. The calculated splitting of the O 1s spectrum by 0.12 eV, due to the different height of the oxygen atoms in the $Ag_{12}O_6$ model, is experimentally not resolved.

The small energy barrier for the rotations of the Ag_6 triangles is reflected by the fact, that the fitted Debye-Waller factor (DWF) of the corner atoms of the Ag_6 triangles is twice as large as the DWF of the Ag atoms in the centre of the Ag_6 triangles. The best SXRD fit result was obtained with isotropic DWFs. All fitted DWFs are on the order of the bulk Ag value of 0.8 \AA^2 , except for the DWF of the Ag atoms at the corners of the Ag_6 triangles, showing a value of 1.73 \AA^2 . Accordingly, the rms vibrational amplitude of the corner Ag atoms in the surface plane is on the order of 0.15 \AA , which is ~ 1.4 times the value of the vibrational amplitude of the Ag atoms in the centre of the triangles.

The presence of the p(4×4) reconstruction leads to a pronounced rumpling of the first substrate layer. The mean inward displacement of the first substrate layer is equal to 0.06 \AA , showing a buckling with an amplitude of 0.12 \AA . The highest lying silver atoms of the first substrate layer are located at the bottom of the furrows in the middle of the oxygen atoms and the lowest lying silver atoms are the corner hole substrate atoms. The silver adatoms reproduce the buckling of the substrate, giving rise to an enhanced height of the silver adatoms in the centre of the Ag_6 triangles. The interatomic distance of the Ag adatoms is expanded with respect to the bulk value of 2.89 \AA up to 2.94 \AA . The second substrate layer shows an inward relaxation of 0.02 \AA . The mean height of the oxygen atoms above the first substrate layer is 2.28 \AA , whereas they are located $\sim 0.11 \text{ \AA}$ below the Ag_6 triangles. Giving rise to a Ag-O distance of $\sim 2.2 \text{ \AA}$. The proposed structural model of the p(4×4) reconstruction is a planar nano-structured adsorbate layer, which bears no resemblance to the bulk oxide Ag_2O . Correspondingly, the p(4×4) structure is not a prototype of a trilayered surface oxide [1].

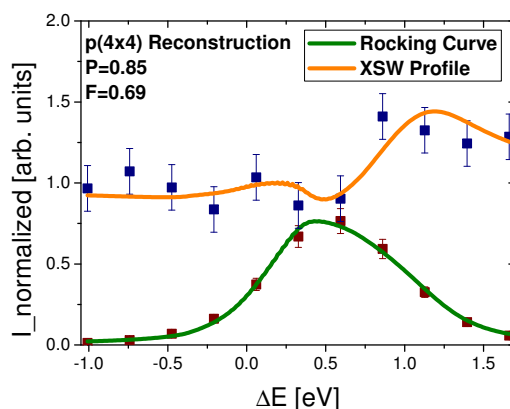


Figure 5.11: Standing wave profile of the oxygen atoms of the p(4×4) reconstruction, showing a coherent position P of 0.85 and a coherent fraction F of 0.69.

The height of the oxygen atoms of the p(4×4) reconstruction with respect to the

bulk Ag(111) planes was determined in addition by NIXSW measurements. The standing wave profile of the oxygen atoms of the $p(4\times 4)$ structure was determined from the oxygen species showing a component in the XPS spectrum at a binding energy of 528.2 eV. One spectrum of the measured data set is shown in figure 6.3. The preparation conditions for the $p(4\times 4)$ structure will be described in section 6.2. The result of the fit to the XSW profile is a coherent position $P = 0.85$ and a coherent fraction $F = 0.69$, which is shown in figure 5.11. The XSW result agrees with a planar oxygen arrangement at a height of 2.00 Å above the bulk Ag(111) planes. The coherent fraction F of 0.69, can be explained by the rotations of the Ag_6 triangles, leading to a distribution of the oxygen position around the mean value. The position of the oxygen atoms relative to the bulk Ag(111) planes, as determined by our SXR measurements, is equal to 2.23 Å, corresponding to a coherent position P of 0.94. In addition, SXR is not very sensitive to the position of the oxygen atoms, due to the low atomic number of oxygen compared to silver. The position of the oxygen atoms determined by SXR and NIXSW agree well, if the error bars are taken into account.

5.5 Stability Diagram of the $p(4\times 4)$ structure

For a profound understanding of the catalytic activity of silver it is indispensable to determine the stable phases under industrial relevant conditions. The phase diagram of the O/Ag(111)-system was calculated by *ab initio* atomistic thermodynamics [16, 22]. It was predicted, that the $p(4\times 4)$ reconstruction is stable under the catalytic conditions of the epoxidation of ethylene (temperatures around 500 K and atmospheric oxygen pressure). We have determined the stability diagram of the O/Ag(111)-system by in-situ SXR measurements. For this purpose scans, which are characteristic for the different phases, are measured against sample temperature and oxygen pressure. The presence of chemisorbed oxygen for example was monitored by a comparison of the signal in the minimum of a CTR at a certain oxygen pressure compared to the clean state under UHV conditions (cf. section 6.2). Three different phases were observed: the clean Ag(111) surface, disordered chemisorbed oxygen and the $p(4\times 4)$ reconstruction. The measured stability diagram is shown in figure 5.12 a).

We have measured the stability diagram from UHV up to 2 bar and from 473 to 723 K, so we closed the so-called 'pressure gap', which describes the discrepancy between ex-situ measurements and the catalytic conditions, by our in-situ SXR measurements. The theoretically predicted phase diagram [16, 22] is in agreement with our results, if the errors of the calculations are taken into account. The error is estimated from the calculated decomposition temperature of Ag_2O at atmospheric oxygen. In the theoretical phase diagram the temperature is underestimated by 110 K and the oxygen pressure is 3 orders of magnitude too high (cf. section 2.2.5). At low temperatures and low oxygen pressures the clean Ag(111) surface is stable. An increase in oxygen pressure leads to dissociative chemisorption of oxygen. From DFT calculations it is known, that oxy-

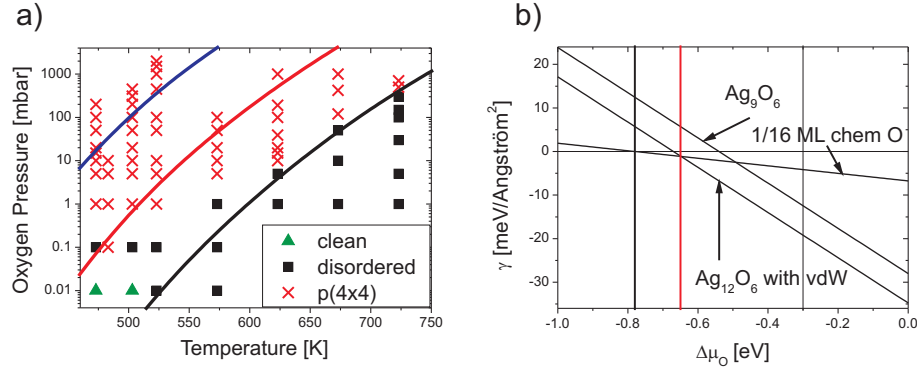


Figure 5.12: a) Stability diagram of the O/Ag(111)-system measured by in-situ SXR. Black line is the calculated stability border of 1/16 ML chemisorbed oxygen, as determined in b). The blue line is the stability border of the Ag_{11}O_6 model determined in [22]. The red line is the stability border of the Ag_{12}O_6 model including effects due to van der Waals interaction [19]. b) Calculated phase diagram in terms of surface energy γ and oxygen chemical potential μ_{O} . The values for the Ag_9O_6 model are taken from [18]. The values for 1/16 ML chemisorbed oxygen are from [22].

gen coverages higher than 0.25 ML lead to a strong repulsion of the partially negative charged oxygen atoms [22, 43]. A further increase of the oxygen pressure results in the formation of the p(4×4) reconstruction, if the temperature is high enough to overcome kinetic barriers, since a considerable rearrangement of silver atoms takes place, when the p(4×4) reconstruction is formed. For example, excess silver atoms must be transported away from the area where the p(4×4) structure grows. The calculated phase diagram in terms of surface energy γ and oxygen chemical potential μ_{O} is shown in figure 5.12 b). The theory of *ab initio* atomistic thermodynamics is explained in section B.2. The structure showing the lowest value of γ is stable for the corresponding values of the oxygen chemical potential. The stability borders in terms of oxygen pressure and temperature are calculated by use of the ideal gas equation. The clean surface acts as a reference and is stable for $\gamma = 0 \text{ eV}/\text{\AA}^2$, which is the horizontal line figure 5.12 b). The clean surface is stable up to an oxygen chemical potential of -0.78 eV, for higher values of μ_{O} disordered chemisorbed oxygen with a coverage of 1/16 ML becomes stable [22]. The calculated stability border of chemisorbed oxygen is shown as black line in figure 5.12 a). The result is in agreement with our measurements, if the error bars of the calculations and our measurements are included. These are 2-3 orders of magnitude in the oxygen pressure for the calculations [22] and ~ 1 order of magnitude in the oxygen pressure for our measurements. Including van der Waals-like interactions between the Ag atoms, the Ag_{12}O_6 model is by 0.8 eV per unit cell more stable, than the Ag_9O_6 model, which is the most stable structure in regular DFT calculations [19]. The energy gain is explained by the fact, that the Ag atoms in the Ag_{12}O_6

model have bulk like Ag-Ag distances. In the Ag_9O_6 model, which is related to the bulk oxide Ag_2O , the Ag-Ag distances are expanded by a factor of 1.2. The Ag_{12}O_6 and the Ag_9O_6 structures have the same amount of oxygen atoms per unit cell, resulting in parallel lines of the surface energy, shown in figure 5.12 b) (cf. section B.2). The $p(4\times 4)$ reconstruction is stable for values of the oxygen chemical potential higher than -0.65 eV. The corresponding stability border of the Ag_{12}O_6 including van der Waals interactions is shown in figure 5.12 a) as red line. For comparison, the stability border of the Ag_{11}O_6 model, as determined in [22], is shown by the blue line in figure 5.12 a). The calculated stability border of the Ag_{12}O_6 model, shown in figure 5.12 a), is in agreement with our SXR measurements, giving a more consistent result, than the previously proposed Ag_{11}O_6 model.

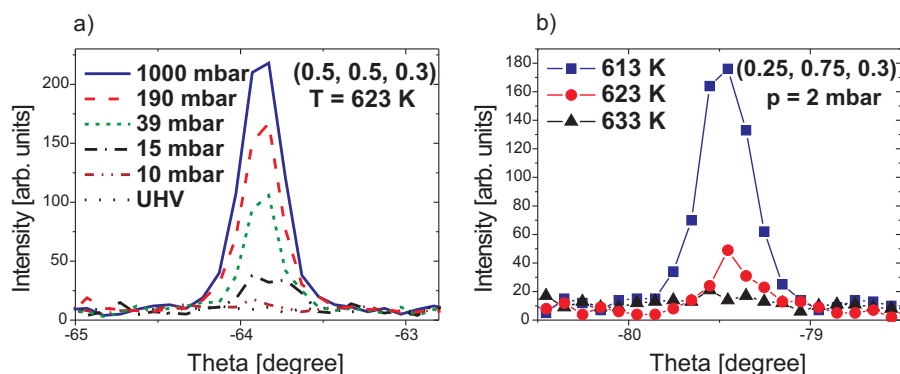


Figure 5.13: Reversible formation and decomposition of the $p(4\times 4)$ reconstruction monitored by in-situ SXR. a) Variation of oxygen pressure at 623 K. b) Variation of sample temperature at 2 mbar of oxygen.

Once formed, the $p(4\times 4)$ reconstruction is stable in UHV up to a temperature of 523 K. This is in agreement with several Temperature Programmed Desorption (TPD) measurements, reporting desorption peaks associated with the decomposition of the $p(4\times 4)$ structure between 560 and 580 K [10, 11, 14]. The onset of the desorption during the TPD experiments agrees with the value of 523 K observed by our SXR measurements. At elevated temperatures ($T > 523\text{K}$) in-situ measurements are indispensable, due to the decomposition or desorption of the different phases if the oxygen pressure is reduced. An extrapolation from ex-situ measurements is not possible in this temperature region. For temperatures $\geq 523\text{K}$ chemisorbed oxygen and the $p(4\times 4)$ structure are in thermodynamic equilibrium with the surrounding gas phase. The variation of the oxygen pressure in this temperature region leads to an instantaneous decomposition or formation of the $p(4\times 4)$ reconstruction, which can be followed by in-situ SXR. Figure 5.13 shows two series of temperature and oxygen pressure scans crossing the phase boundary of the $p(4\times 4)$ reconstruction, where the reversible growth and decomposition of the $p(4\times 4)$ structure was observed in-situ. The formation and de-

composition of the p(4×4) reconstruction is completely reversible under the conditions shown in figure 5.13.

Another important result is the fact, that the p(4×4) reconstruction is stable under the catalytic conditions of the epoxidation of ethylene (523 K and an oxygen pressure of 2 bar), which can be seen in figure 5.12 a). This might be an indication, that the p(4×4) reconstruction plays an important role for the catalytic activity of silver for the epoxidation of ethylene. The structure of the p(4×4) reconstruction remains unaffected by changing temperature and oxygen pressure, which was proven by measuring an in-plane data set of the p(4×4) reconstruction at 553 K and 80 mbar of oxygen, showing the same behaviour as the one measured at room temperature, shown in figure 5.8 a).

Further theoretical input including DFT and *ab initio* atomistic thermodynamics calculations on the basis of the new Ag₁₂O₆ model is needed to determine possible reaction pathways for the epoxidation of ethylene in the presence of the p(4×4) reconstruction. Thereby, it is most likely that the p(4×4) structure acts as a reservoir of atomic oxygen facilitating the oxidation reactions.

Chapter 6

A Zoo of Oxygen Induced Structures

The interaction of oxygen with the Ag(111) surface was studied by systematic SXR and LEED measurements, revealing several previously unknown oxygen induced structures. The results presented here, range from the determination of the relaxation of the clean Ag(111) surface to the formation of the bulk oxide Ag₂O. The chapter is structured as follows: at first the results for the clean surface are presented, the formation of disordered chemisorbed oxygen was studied by SXR and NIXSW, in the following we will focus on oxygen induced structures, involving ordered chemisorbed oxygen, then three reconstructions built up by Ag triangles will be presented, the formation of the bulk oxide in $(\bar{1}\bar{1}\bar{1})$ orientation will be discussed, showing a coexistence with a $p(7\times 7)$ reconstruction, which is most likely a surface oxide and finally the stability diagram of the O/Ag(111)-system will be presented.

6.1 The clean Ag(111) Surface

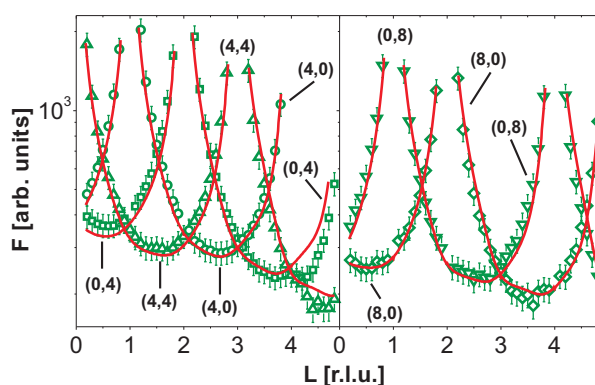


Figure 6.1: Measured CTRs of the clean Ag(111) surface and the corresponding fit.

The relaxation of the clean Ag(111) surface was determined by a simultaneous fit of five independent CTRs, which were measured under UHV conditions and room temperature. The CTRs and the corresponding fit are shown in figure 6.1. For the structure refinement 7 independent parameters were used: 2 scale factors, 3 z-displacement parameters of the first 3 layers and the Debye-Waller factors of the first and second layer B_2 and B_1 . The Debye-Waller parameter B_0 of the third layer was fixed to the bulk value of 0.8 \AA^2 . The agreement between the fitted and the measured CTRs is very good, as can be seen in figure 6.1, which is reflected in a χ^2 of 1.20. The result of the fit is a reduction of the first interlayer spacing by 1.23 % and a contraction by 1.17 % of the second interlayer spacing, which is shown in figure 6.2.

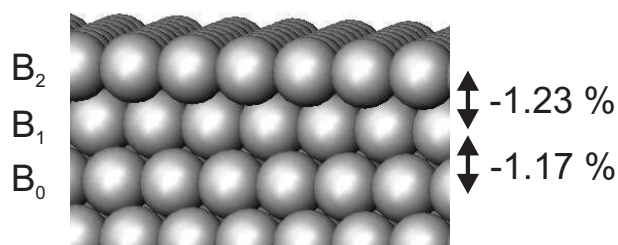


Figure 6.2: Relaxation and Debye-Waller factors of the clean Ag(111) surface determined by SXRD.

From the fit one obtains a value of 1.62 \AA^2 for the Debye-Waller factor B_2 of the topmost silver layer and a value of $B_1 = 1.10 \text{ \AA}^2$ for the second substrate layer. This means, that the vibrational amplitude of the atoms of the first silver layer is strongly enhanced, which is an expected behaviour for a material showing a low Debye temperature. The results are in agreement with a LEED-I(V) study [41] and serve as a reference for the studies of the oxidized Ag(111) surface. The results of the LEED-I(V) study are a contraction of the first interlayer spacing by $(0.5 \pm 0.8)\%$ and $(0.4 \pm 1.2)\%$ for the second interlayer spacing.

6.2 Disordered chemisorbed Oxygen

For low temperatures and low oxygen pressure, disordered dissociative chemisorption of oxygen on Ag(111) can be observed [14, 42]. The chemisorption of oxygen was studied by STM at a coverage of 0.05 monolayers (ML) [42]. A repulsive interaction of the partially negative charged oxygen atoms was observed, resulting in a minimum distance of $\sim 10 \text{ \AA}$ between two oxygen atoms. The presence of this oxygen species can be observed by XPS, showing an O 1s component at a binding energy of 530 eV [14]. In this work the height of oxygen atoms above the first substrate layer was determined by a fit of the x-ray standing wave profile of the O 1s component at a

binding energy of 530 eV. The height of the oxygen atoms above the first substrate layer can be extracted from the fitted coherent position P . The clean Ag(111) surface was oxidized by 600 Langmuir (1 Langmuir = 10^{-6} mbar · seconds) NO_2 at a temperature of 518 K. A coexistence of three different oxygen species was observed by measuring the O 1s photoelectron spectrum, which is shown in figure 6.3.

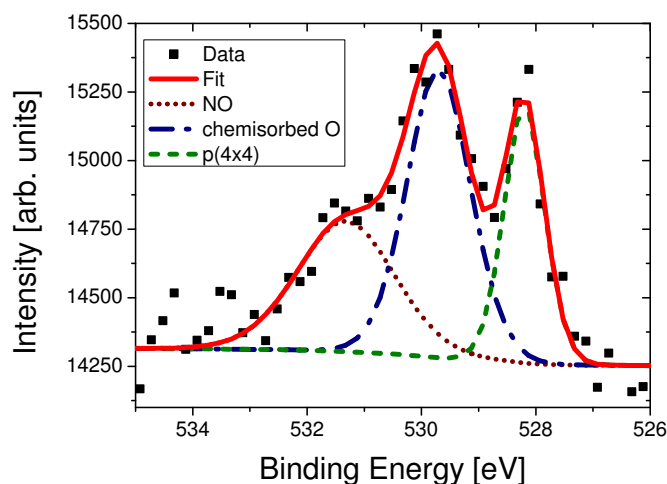


Figure 6.3: XPS spectrum of the oxidized Ag(111) surface. The $p(4 \times 4)$ reconstruction shows a component at 528.2 eV, the component at 529.7 eV is assigned to chemisorbed oxygen and the one at 531.3 eV is due to the presence of NO on the surface.

The presence of the $p(4 \times 4)$ reconstruction was proven by LEED measurements (not shown here). The $p(4 \times 4)$ reconstruction shows a component at 528.2 eV, chemisorbed oxygen gives rise to the component at 529.7 eV and the presence of NO on the surface is reflected in the component at 531.3 eV. The observed values of the binding energies are in agreement with other XPS measurements [12, 14]. The measured XPS spectrum was decomposed using a Gaussian/Lorentzian product form line shape for the three components and a Shirley-type background to take the observed asymmetry into account. The standing wave profile for chemisorbed oxygen with the fit is shown in figure 6.4.

The result is a coherent position P of 0.67, which corresponds to an oxygen height of 1.57 \AA above the first substrate layer. The value of the coherent fraction of 0.43 is rather low, which is an indication for a broad distribution of the oxygen position around the mean value of 1.57 \AA due to static and dynamic displacements. This implies, that small changes in P only lead to small variations of the standing wave profile, which means that a wide range of P values is in agreement with the experimentally observed standing wave profile. This fact is shown in figure 6.5, where the value of χ^2

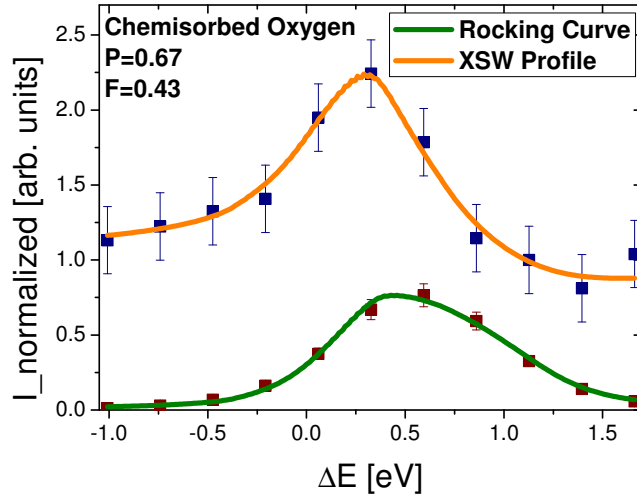


Figure 6.4: Standing wave profile of disordered chemisorbed oxygen on Ag(111), showing a coherent position P of 0.67 and a coherent fraction F of 0.43.

of different fits is plotted against a range of P values, whereas F was kept constant at 0.43.

The result of the χ^2 -analysis is, that the simulated standing wave profiles are in sufficient agreement with the data set for values of the coherent position between 0.5 and 0.75, which corresponds to a height of the oxygen atoms above the first substrate layer of 1.47 ± 0.3 Å. By means of DFT the energetically most favourable adsorption site was determined to be the on-surface fcc hollow site [16, 43, 44]. The calculated height of the oxygen atoms above the first substrate layer varies between 1.21 and 1.32 Å, depending on the oxygen coverage and the details of the calculation. DFT calculations from [16] predict a height of 1.21 to 1.32 Å for an oxygen coverage of 0.06 to 0.25 ML, the results of a second DFT study [43] are oxygen heights of 1.24 to 1.22 Å for an oxygen coverage of 0.11 to 0.25 ML and in [44] a height of 1.32 Å was determined for an oxygen coverage of 0.25 ML. Our results agree with an on-surface adsorption of the oxygen atoms at fcc sites.

In a STM study the adsorption of single oxygen atoms on Ag(111) was observed, but at the same time aggregates of up to three oxygen atoms were also present [42]. These structures show a slightly different appearance in the STM. We propose, that this observation is caused by the repulsive interaction of the chemisorbed oxygen atoms, leading to changes in the local binding geometry at the fcc site, depending on the surrounding of the individual oxygen atom. The disordered nature of the adsorption process gives rise to different possibilities of the local binding geometry of the oxygen

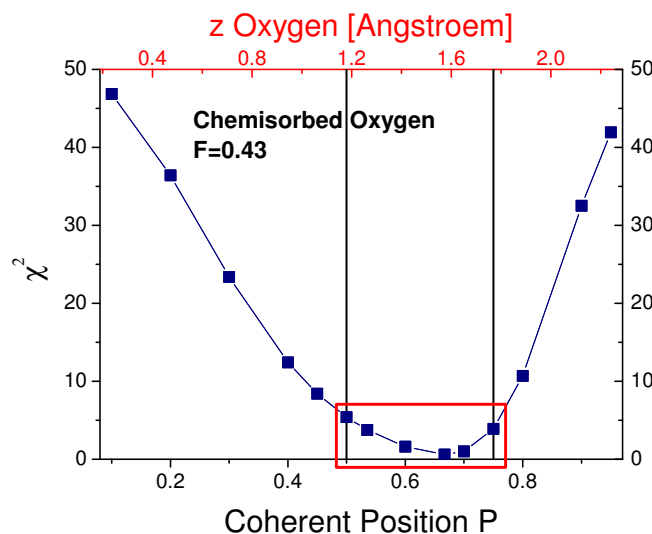


Figure 6.5: χ^2 values for a constant coherent position of 0.43 for different P values. The standing wave profile shows sufficient agreement with the data set for P values between 0.5 and 0.75, which corresponds to heights of the oxygen atoms above the first substrate layer between 1.18 Å and 1.77 Å.

atoms at the fcc site, resulting in a broad height distribution of the oxygen atoms, which is in agreement with the observed coherent fraction of 0.43.

Further insight into the adsorption process of oxygen atoms on the Ag(111) surface is provided by our in situ SXR measurements. In the case of the SXR measurements the clean Ag(111) surface was oxidized by molecular oxygen at elevated sample temperatures. Rocking scans were performed at a q-value of (1, 1, 1.2) in the minimum of a CTR of the silver surface at a temperature of 573 K. At this so-called "Anti-Bragg"-position of the CTR the signal is very sensitive to small changes of the position of the silver atoms within the surface. The signal of the clean surface was measured as a reference under UHV conditions. For oxygen pressures between 0.01 and 0.1 mbar a loss of intensity was observed, which can be seen in figure 6.6. Further exploration of reciprocal space showed, that no ordered superstructure was present on the surface under these conditions. The decrease of the signal is caused by chemisorption of atomic oxygen in a disordered state. The bonding of the oxygen atoms to the silver surface leads to displacements of silver atoms within the first substrate layer. Disordered chemisorption leads to random displacements of silver atoms with respect to their mean positions in the clean state. The reduction in the integrated intensity of the rocking scans, which is proportional to the structure factor, can be described by a Debye-Waller factor, since we are dealing with random displacements with respect

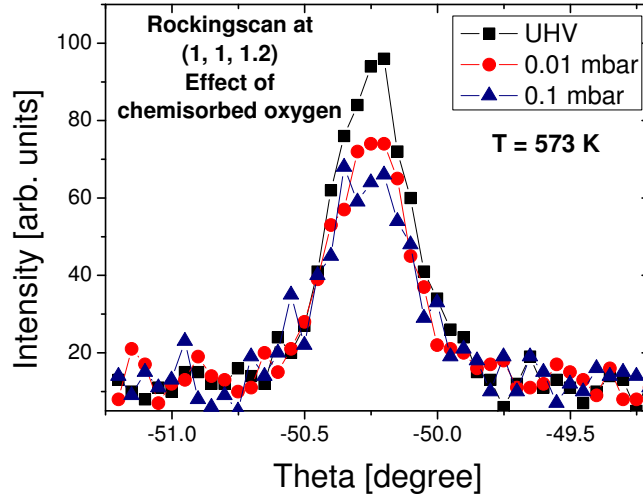


Figure 6.6: Rocking scans measured in the minimum of a CTR for different oxygen pressures at a temperature of 573 K. The loss of intensity is caused by static displacements of the silver atoms of the first substrate layer, due to the disordered chemisorption of oxygen atoms at an oxygen pressure of 0.01 and 0.1 mbar.

to the mean position of the clean state. The result is a root mean square (rms) displacement $\sqrt{\langle u_x^2 \rangle} = 0.12 \text{ \AA}$ of the silver atoms in the surface plane. This result is in agreement with DFT calculations [43], where in-plane displacements of silver atoms between 0.03 and 0.11 \AA were determined, for oxygen coverages of chemisorbed oxygen between 0.11 and 0.75 MLs.

In summary, we have determined a height of $1.47 \pm 0.3 \text{ \AA}$ of chemisorbed oxygen atoms above the first substrate layer of the Ag(111) surface. The low coherent fraction of 0.43 of the standing wave profile reflects the disordered adsorption geometry of the oxygen atoms, resulting in a broad height distribution of the adsorbates. Our results are in line with an adsorption of the oxygen atoms at the fcc hollow site, as predicted by DFT calculations [16, 43, 44], leading to random in-plane displacements of the silver atoms on the order of 0.12 \AA , as determined by our in situ SXR measurements. Further reciprocal space exploration by SXR proved the disordered nature of the dissociative chemisorption process of molecular oxygen on the Ag(111) surface, as it was observed by STM measurements [42].

6.3 Periodic Structures induced by chemisorbed Oxygen

6.3.1 Oxygen induced modulation along (110)

Extensive reciprocal space exploration revealed the occurrence of satellite peaks close to the (1,0) and (0,1) CTR at an oxygen pressure of 15 mbar and a sample temperature of 473 K. Two peaks were observed near the (0,1) CTR. One peak in the $(\bar{1}\bar{1})$ direction at $(-0.14, 0.86, 0.3)$ and a second peak in the $(1\bar{2})$ direction at $(0.14, 0.72, 0.3)$. The corresponding satellite peaks were also observed close to the (1,0) CTR. At $(0.72, 0.14, 0.3)$ in the $(\bar{2}1)$ direction and at $(0.86, -0.14, 0.3)$ in the $(\bar{1}\bar{1})$ direction. An in-plane scan along the (1,1) direction through the (1,0) CTR, including the satellite peak at $(0.86, -0.14, 0.3)$, is shown in figure 6.7 a).

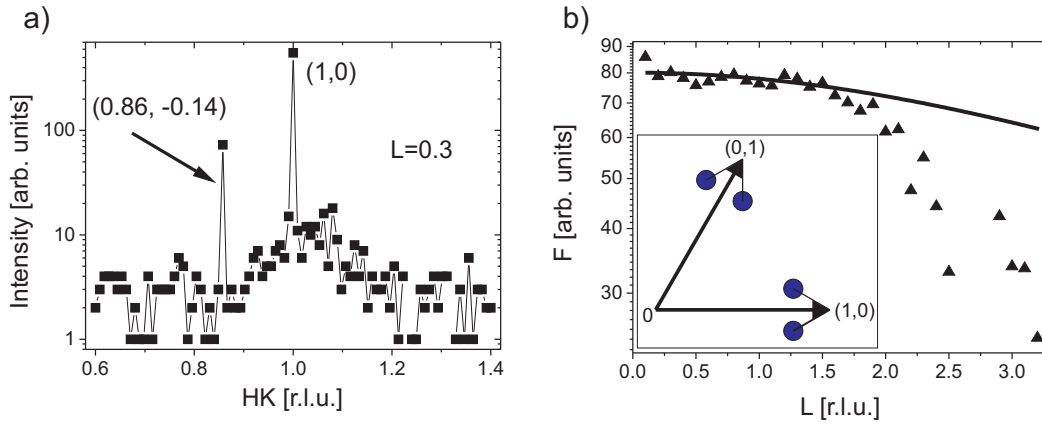


Figure 6.7: a) In-plane Scan along the (110) direction through the CTR at $(1,0,0.3)$. The satellite peak from the modulated structure is visible at $(0.86, -0.14, 0.3)$. b) Surface rod measured along $(-0.14, 0.86, L)$, compared with the surface contribution of an undistorted silver monolayer (solid line). The position of the satellite peaks in the HK-plane is shown in the inset of b).

Satellite peaks are observed, if a modulated structure is present [24]. In this case, the diffraction pattern consists of the Bragg peaks of the mean lattice and the satellite peaks caused by the modulation of the lattice. The wave vector of the modulation, given by $\mathbf{q}_m = 2\pi/\lambda_m$, defines the distance between the Bragg peaks and satellite peaks in reciprocal space. λ_m defines the period length of the modulation in real space and the direction of the modulation is given by the direction of \mathbf{q}_m . The distance to the CTRs is equivalent for all satellite peaks. The value of λ_m can be determined from the position of the satellite peaks. For the determination of λ_m the length of the reciprocal lattice \mathbf{a}_1^* vector is needed, which is given by $|\mathbf{a}_1^*| = 2\pi/\frac{\sqrt{3}}{2}a_1$. $a_1 = 2.89 \text{ \AA}$ is the

lattice constant of the hexagonal Ag(111) surface in the surface plane. The result for λ_m is obtained by

$$q_m = \frac{4\pi}{\sqrt{3}a_1} \cdot \frac{\sqrt{3}}{2} \cdot 0.28 = \frac{2\pi}{\lambda_m} \quad (6.1)$$

$$\lambda_m = \frac{a_1}{0.28}. \quad (6.2)$$

The satellite peaks can be explained by an oxygen induced modulation of the Ag(111) surface along the (110) direction, showing a period length of 10.32 Å. Further exploration of reciprocal space showed, that the modulated structure is only periodic along the (110) direction.

The surface rods of the modulated structure were measured, providing more insight into the structure of the modulation. All surface rods show the same behaviour and as an example the (-0.14,0.86,L) rod is shown in figure 6.7 b). The surface rod is compared to the calculated signal of an undistorted silver monolayer. The signal of the modulated structure is similar to the calculated monolayer contribution and shows a stronger decrease of the signal for large values of L. The most important result is, that no oscillations can be observed along the surface rod, which means, that the modulation is restricted to the topmost silver layer. Furthermore, we know, that the period length of the modulation is incoherent with respect to the substrate lattice. This implies, that the repulsive oxygen-oxygen interaction dominates over the oxygen-substrate interactions, resulting in arbitrary oxygen positions with respect to the substrate. The construction of a model is straightforward and the result is shown in figure 6.8.

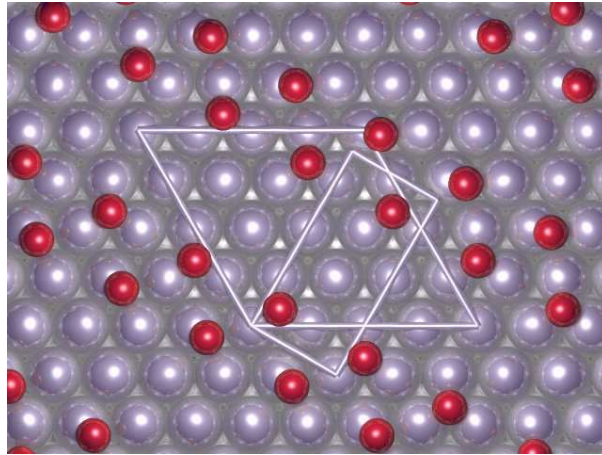


Figure 6.8: Oxygen induced modulation of the first substrate layer along the (110) direction with a period length of 10.32 Å. Chemisorbed oxygen atoms are shown as red spheres. The unit cell of the p(4×4) reconstruction is shown as reference.

Even though the modulation is only periodic along the (110) direction, we have chosen a $\sqrt{3}$ R30° periodicity perpendicular to the (110) direction for the illustration of the structure in figure 6.8. This assumption is in agreement with our measurements, if the domain size of the modulated in the direction perpendicular to the (110) direction is very small, or if the adsorption of oxygen does not lead to distortions of the silver substrate in this direction. This choice is also based on the results which were obtained for the $(\sqrt{3} \times 2.28)\text{rect}$ R30° reconstruction, which will be presented in the following section. In the model shown in figure 6.8 two chemisorbed oxygen atoms are placed on two of the four possible fcc sites in the unit cell, resulting in an oxygen coverage of 0.28 ML, which can be compared to the value of 0.375 ML for the p(4×4) reconstruction. The modulation of the first silver layer is produced by the stripes of chemisorbed oxygen, which result in a periodic distortion of the first substrate layer. In figure 6.8 only one of three possible domains is presented, which are rotated by 120° with respect to each other.

The modulated structure was observed up to a sample temperature of 503 K in coexistence with the p(4×4) structure. Furthermore, we observed an increase of the signal of the p(4×4) reconstruction with increasing oxygen pressure, accompanied by a decomposition of the satellite peaks (cf. section 6.6). This observation is an indication, that the modulated structure is a transient state transforming into the p(4×4) reconstruction. Up to a temperature of 503 K this metastable state seems to be 'frozen', for temperatures higher than 503 K the formation of the modulation could not be observed. The formation of a metastable precursor of the formation of the p(4×4) reconstruction was studied by means of DFT calculations [51]. It was suggested, that for an oxygen coverage higher than 0.24 ML a transient state, built up by on-surface and sub-surface oxygen, should form. From our measurements, we cannot conclude that sub-surface oxygen is present, since the deformation of the silver lattice upon adsorption of oxygen below the first substrate layer, would lead to oscillations on the surface rods, which were not observed for the modulated structure. We suggest, that the repulsive interaction of the partially negative charged oxygen atoms leads to the formation of the stripes with a distance of 10.32 Å and the repulsive interaction seems to be not strong enough to give rise to a strong deformation of the first silver layers due to the formation of sub-surface oxygen. The oxygen coverage of 0.28 ML for the model of the modulation is midway of the formation of disordered chemisorbed oxygen with a coverage of 0.05 ML, as it was observed during STM measurements [42], and the p(4×4) reconstruction, showing an oxygen coverage of 0.375 ML. This is in agreement with the assumption, that the modulated structure is a metastable state, transforming into the p(4×4) reconstruction with increasing oxygen pressure and instantaneously for temperatures higher than 503 K.

6.3.2 $(\sqrt{3} \times 2.28)\text{rect R}30^\circ$ Reconstruction

Systematic LEED measurements revealed the formation of an oxygen induced $(\sqrt{3} \times 2.28)\text{rect R}30^\circ$ reconstruction, after oxidizing the Ag(111) sample at a temperature of ~ 430 K and oxygen pressures between 5 and 10 mbar for 30 minutes. An inverted LEED pattern, measured at an electron energy of 48 eV, and a calculated LEED pattern of a $(\sqrt{3} \times 2.28)\text{rect R}30^\circ$ reconstruction are shown in figure 6.9. All measured reflections can be explained by three domains of a $(\sqrt{3} \times 2.28)\text{rect R}30^\circ$ reconstruction rotated by 120° with respect to each other, as it is shown in figure 6.9 b).

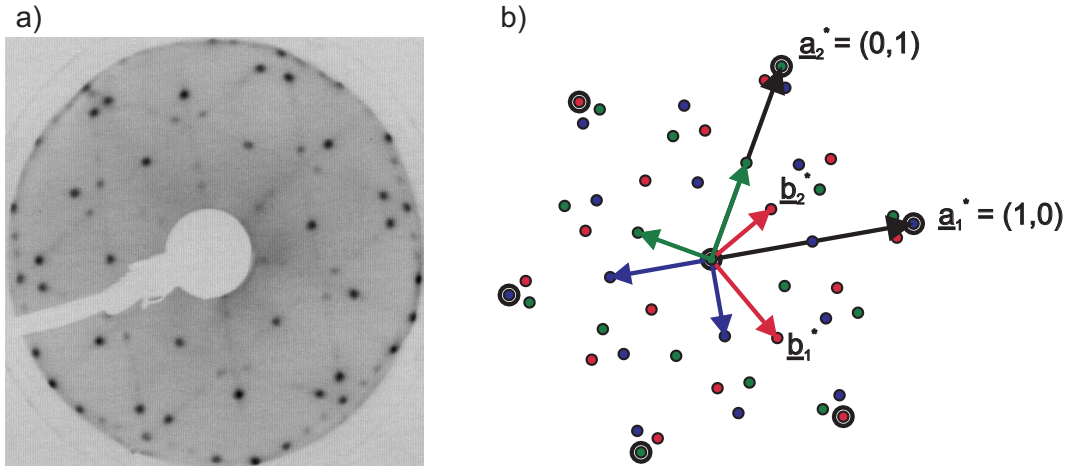


Figure 6.9: a) Inverted LEED image of the oxygen induced $(\sqrt{3} \times 2.28)\text{rect R}30^\circ$ reconstruction, measured at an electron energy of 48 eV. b) Calculated LEED image, reproducing all observed reflections.

The structure has a rectangular unit cell, which is commensurate along the $(1\bar{1}0)$ direction with a period length of $\sqrt{3}a_1 = 5.01$ Å, being two times the substrate lattice plane spacing along this direction, and incoherent along the (110) direction with a period length of 6.59 Å. The incoherent superstructure is either described by the Wood notation as $(\sqrt{3} \times 2.28)\text{rect R}30^\circ$ reconstruction or in matrix notation by the following matrix $\mathfrak{M}_{\text{incoherent}}$ relating the in-plane unit cell vectors of the reconstruction \mathbf{b}_1 and \mathbf{b}_2 to the in-plane unit cell vectors of the substrate \mathbf{a}_1 and \mathbf{a}_2 (cf. section A.2).

$$\mathbf{b} = \mathfrak{M} \cdot \mathbf{a} \quad (6.3a)$$

$$\mathfrak{M}_{\text{incoherent}} = \begin{pmatrix} 1 & -1 \\ 2.28 & 2.28 \end{pmatrix} \quad (6.3b)$$

The construction of the simplest model is related to the modulated structure, which was discussed in the preceding section. The incoherent $(\sqrt{3} \times 2.28)\text{rect R}30^\circ$ recon-

struction has no common periodicity with respect to the substrate along the (110) direction, as it is the case for the modulated structure. This is an indication, that the repulsive oxygen-oxygen interaction dominates over the oxygen-substrate interaction. Furthermore, the formation of sub-surface oxygen should occur theoretically at tetrahedrally coordinated sites between the first and second substrate layer below the on-surface fcc hollow site, as it was determined by DFT calculations [16, 51, 52]. Such an incorporation would lead to a periodic arrangement of the oxygen atoms, which is not observed experimentally. We suggest, that two chemisorbed oxygen atoms are present per unit cell. In the model, shown in figure 6.10, they are positioned at two of four fcc hollow sites within the unit cell. This oxygen arrangement results, like for the modulated structure, in oxygen stripes, which are 6.59 Å apart. The oxygen atoms are located on arbitrary positions with respect to the substrate, due to the incommensurability along the (110) direction. The smallest oxygen-oxygen distance is 3.37 Å, which is a little bit smaller than for the modulated structure, showing an oxygen-oxygen distance of 3.98 Å within the stripes. These values are still smaller, than the oxygen-oxygen distance in the $p(4\times 4)$ reconstruction showing a value of 2.84 Å. This seems to be related to a stronger repulsive interaction of the chemisorbed oxygen atoms in the modulated structure and the $(\sqrt{3} \times 2.28)\text{rect } R30^\circ$ reconstruction.

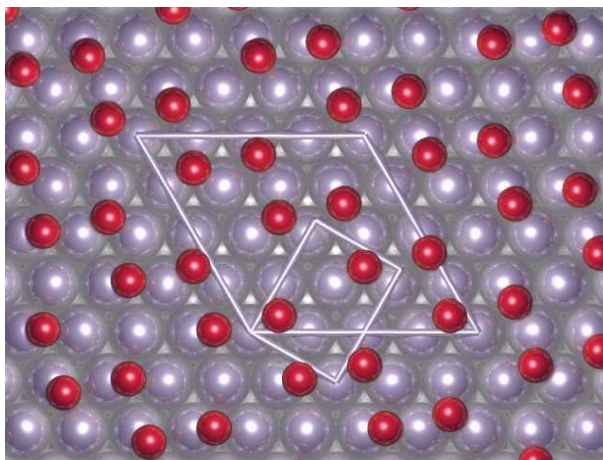


Figure 6.10: Oxygen induced $(\sqrt{3} \times 2.28)\text{rect } R30^\circ$ reconstruction. Chemisorbed oxygen atoms are shown as red spheres. The unit cell of the $p(4\times 4)$ reconstruction is shown as reference.

The proposed model of the $(\sqrt{3} \times 2.28)\text{rect } R30^\circ$ reconstruction has an oxygen coverage of 0.44 ML, which is the highest coverage of all observed oxygen induced structures on Ag(111). A coexistence of the $p(4\times 4)$ structure and the $(\sqrt{3} \times 2.28)\text{rect } R30^\circ$ reconstruction was observed after oxidizing the Ag(111) surface at a temperature of ~ 430 K and an oxygen pressure of 1 mbar, resulting in a superposition of the LEED patterns of both structures (not shown here). The $p(4\times 4)$ reconstruction, which has an

oxygen coverage of 0.375 ML, transforms into the $(\sqrt{3} \times 2.28)\text{rect R}30^\circ$ structure at an oxygen pressure of 5 mbar and a temperature of 430 K. The $(\sqrt{3} \times 2.28)\text{rect R}30^\circ$ reconstruction seems to be a metastable structure, which is only stable around 430 K, since it was not observed during our in-situ SXRD measurements, which were performed for temperatures higher than 473 K. High coverage structures built up by chemisorbed oxygen atoms are also observed on Rh(111), where a $(2\sqrt{3} \times 2\sqrt{3})\text{R}30^\circ$ reconstruction is observed, showing an oxygen coverage of $2/3$ ML [87].

The oxygen induced modulation along the (110) direction and the $(\sqrt{3} \times 2.28)\text{rect R}30^\circ$ reconstruction, which were observed by us for the first time, are incoherent with respect to the substrate. Similar results are obtained for CO adsorption on Pt(111), where the repulsive adsorbate-adsorbate interaction dominates over the adsorbate-substrate interactions for the case of the $(\sqrt{19} \times \sqrt{19})\text{R}23.4^\circ$ reconstruction [88–90] and similar incoherent structures [91, 92].

6.4 Reconstructions involving adsorbed Silver Triangles

6.4.1 O-p(4×4)/Ag(111): No surface oxide

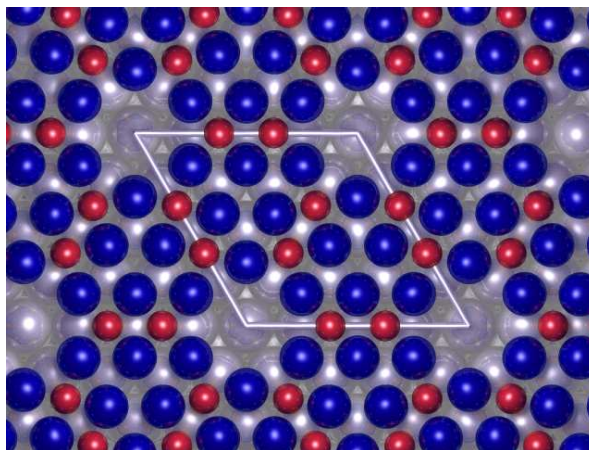


Figure 6.11: Oxygen induced p(4×4) reconstruction. Adsorbed silver atoms within the triangles are shown as blue spheres. Oxygen atoms are shown as red spheres.

The structure of the p(4×4) reconstruction was already discussed in detail in chapter 5. The proposed model is built up by two Ag_6 triangles of adsorbed silver atoms, one triangle located on fcc sites and the other on hcp sites. The silver triangles are connected by 6 oxygen atoms per unit cell, resulting in a Ag_{12}O_6 stoichiometry and an oxygen coverage of 0.375 ML. The best fit to our SXRD data set was obtained with

$p6mm$ symmetry, which was observed in the measured in-plane data, which are shown in figure 5.8 a). Applying $p6mm$ symmetry results in a planar arrangement of the silver adatoms and the oxygen atoms. The structural model, shown in figure 6.11, bears no resemblance to a three-layered slab of $Ag_2O(111)$ and is accordingly not a surface oxide, but rather a nano structured adsorbate layer. The formation of adsorbed silver triangles seems to be a structural building block, which can be used to build models of the oxygen induced $p(5 \times 5)$ and $c(3 \times 5\sqrt{3})rect$ reconstructions. This will be discussed in the following sections.

6.4.2 O- $p(5 \times 5)/Ag(111)$ Reconstruction

An oxygen induced $p(5 \times 5)$ reconstruction could be observed by us in our in-situ SXR D measurements and in LEED for the first time. The LEED measurements were performed at Lund, where the $Ag(111)$ surface was oxidized with 600 L NO_2 at 500 K. The NO_2 was pumped down and the sample was cooled down to room temperature, followed by an annealing cycle up to 418 K, resulting in the formation of the $p(5 \times 5)$ reconstruction. The corresponding LEED pattern is shown in figure 6.12 a).

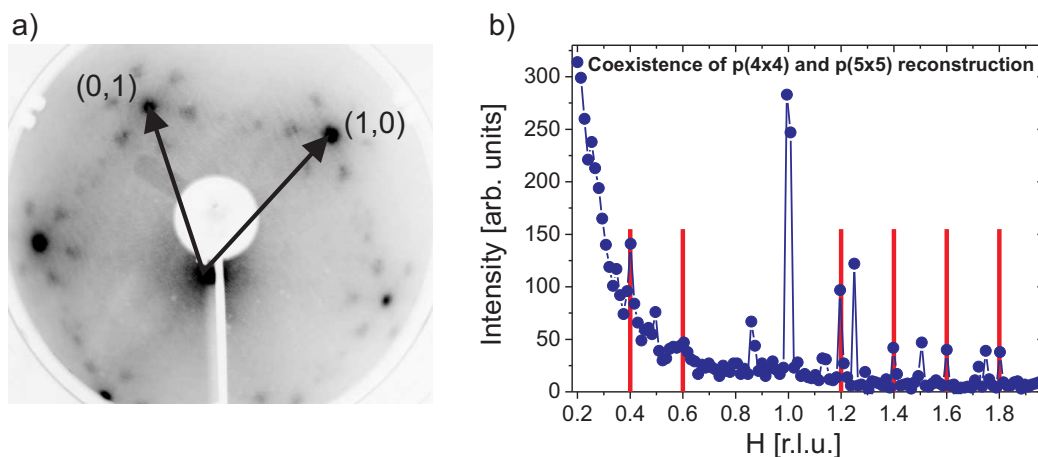


Figure 6.12: a) LEED image of the oxygen induced $p(5 \times 5)$ reconstruction, recorded at an electron energy of 118 eV. The superstructure reflections are visible at multiples of 0.2. b) In-plane scan along the (100) direction for $L = 0.1$, showing a coexistence of the $p(4 \times 4)$ and $p(5 \times 5)$ reconstructions, measured at 423 K. All observed reflections of the $p(5 \times 5)$ reconstruction are marked by the red lines.

During the in-situ SXR D experiments the $Ag(111)$ sample was oxidized at 473 K and 1 bar of oxygen resulting in the formation of the $p(4 \times 4)$ reconstruction. The sample was cooled down to 453 K at 1 bar of oxygen. Under these conditions the formation of the $p(5 \times 5)$ reconstruction in coexistence with the $p(4 \times 4)$ structure was observed.

The same observation was made at 423 K. An in-plane scan along the (100) direction, showing superstructure reflections of the $p(5 \times 5)$ structure at multiples of 0.2 and reflections of the $p(4 \times 4)$ reconstruction at multiples of 0.25, measured at 423 K and 1 bar of oxygen, is shown in figure 6.12 b). In the LEED experiment only the $p(5 \times 5)$ reconstruction was observed, because chemisorbed oxygen atoms transform into the $p(4 \times 4)$ reconstruction above ~ 420 K. During the preparation, the sample, covered by chemisorbed oxygen, was only heated to 418 K. This means, that the $p(5 \times 5)$ reconstruction forms at lower temperatures than the $p(4 \times 4)$ structure.

We propose a structural model of the $p(5 \times 5)$ reconstruction, which is built up by two Ag_{10} triangles, located on fcc and hcp sites, as it is the case for the $p(4 \times 4)$ structure. The adsorbed Ag_{10} triangles are connected by 9 oxygen atoms per unit cell, resulting in a Ag_{20}O_9 stoichiometry and an oxygen coverage of 0.36 ML. This model is obtained from the structure of the $p(4 \times 4)$ reconstruction by adding one silver row to the Ag_6 triangles. The structural model is shown in figure 6.13.

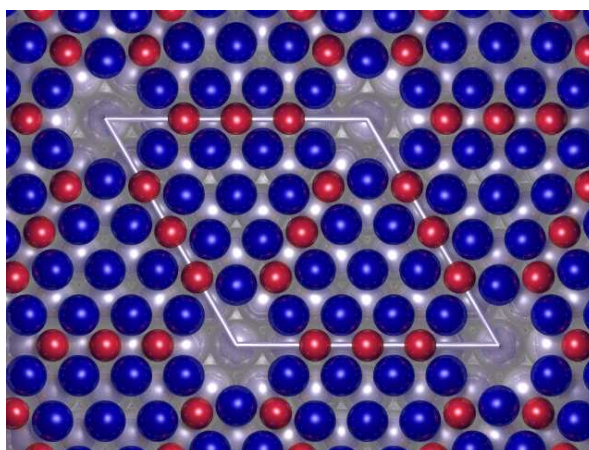


Figure 6.13: Oxygen induced $p(5 \times 5)$ reconstruction. Adsorbed silver atoms within the triangles are shown as blue spheres. Oxygen atoms are shown as red spheres.

In our in-situ SXRD experiments we could observe the $p(5 \times 5)$ reconstruction only up to a temperature of 453 K. At higher temperatures the $p(5 \times 5)$ structure is not stable and either transforms into the $p(4 \times 4)$ reconstruction, which has a slightly higher oxygen coverage, or it decomposes. The proposed model of the $p(5 \times 5)$ structure is not a surface oxide, since it bears no resemblance to a three-layered slab of the bulk oxide Ag_2O in (111) orientation.

6.4.3 $c(3 \times 5\sqrt{3})_{\text{rect}}$ Reconstruction

STM measurements revealed the formation of a $c(3 \times 5\sqrt{3})_{\text{rect}}$ reconstruction after oxidizing the clean $\text{Ag}(111)$ surface with atomic oxygen at a temperature of 500 K

[20]. This reconstruction was observed in coexistence with the $p(4\times 4)$ reconstruction by STM. The model proposed in [20] is similar to the Ag_{12}O_6 model of the $p(4\times 4)$ reconstruction. The Ag_6 triangles are arranged in another orientation with respect to the substrate, resulting in a $c(3 \times 5\sqrt{3})\text{rect}$ periodicity, having the same oxygen coverage as the $p(4\times 4)$ reconstruction. The structural model is shown in figure 6.14, where the primitive unit cell of the $c(3 \times 5\sqrt{3})\text{rect}$ is also shown. The primitive unit cell is described in matrix notation by the matrix $\mathfrak{M}_{c(3 \times 5\sqrt{3})}$

$$\mathfrak{M}_{c(3 \times 5\sqrt{3})} = \begin{pmatrix} 3 & 0 \\ 4 & 5 \end{pmatrix}. \quad (6.4)$$

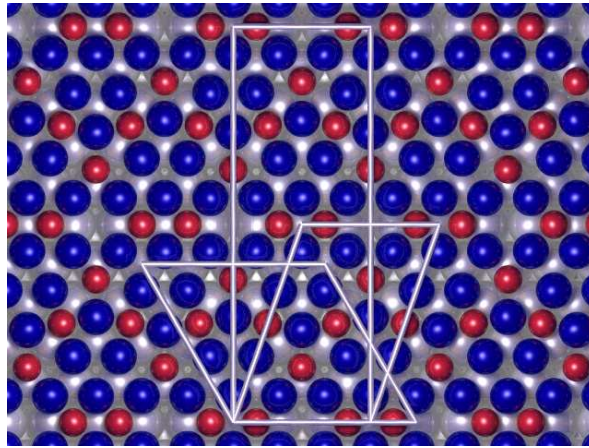


Figure 6.14: Oxygen induced $c(3 \times 5\sqrt{3})\text{rect}$ reconstruction. Adsorbed silver atoms within the triangles are shown as blue spheres. Oxygen atoms are shown as red spheres. The rectangular and the primitive unit cell of the $c(3 \times 5\sqrt{3})\text{rect}$ reconstruction are shown. The unit cell of the $p(4\times 4)$ reconstruction is shown as reference.

DFT calculations showed, that the $c(3 \times 5\sqrt{3})\text{rect}$ reconstruction has a ground state energy similar to the Ag_{12}O_6 model of the $p(4\times 4)$ reconstruction [20]. The $c(3 \times 5\sqrt{3})\text{rect}$ reconstruction could not be observed by us during our SXR and LEED measurements, which could be related to the fact, that we have never used atomic oxygen during our experiments.

6.5 Structures related to $\text{Ag}_2\text{O}(\bar{1}\bar{1}\bar{1})$

For a detailed microscopic picture of the catalytic properties of $\text{Ag}(111)$ it is of key importance to understand, whether or not an O-Ag-O trilayer surface oxide can emerge, as it was found for the other 4d transition metals, like Pd and Rh [1, 3, 4], and whether the growth of a Ag_2O bulk oxide on $\text{Ag}(111)$ is even possible. The oxidation behaviour of

Ag(111) was studied by means of in-situ surface x-ray diffraction at atmospheric oxygen pressure [21]. Exposure to 1 bar oxygen at 773 K reveals a competing growth of three different oxygen-induced structures on Ag(111), namely the well-known $p(4 \times 4)$ reconstruction, a surface oxide in a $p(7 \times 7)$ coincidence structure and the bulk oxide Ag_2O in $(\bar{1}\bar{1}\bar{1})$ orientation. The latter two exhibit the same honeycomb on hexagon arrangement of the Ag sublattice with respect to the Ag(111) surface. An inverted stacking of Ag planes in the bulk oxide islands is observed as compared to the Ag(111) substrate, which sheds new light on the Ag_2O formation process. As we will show, Ag_2O grows epitaxially on Ag(111) in a Stranski-Krastanow like growth mode [45]. Finally, we present a structural model of the $p(7 \times 7)$ reconstruction, based on a three-layer O-Ag-O slab of $\text{Ag}_2\text{O}(111)$.

6.5.1 Structure and orientation of Ag_2O on Ag(111)

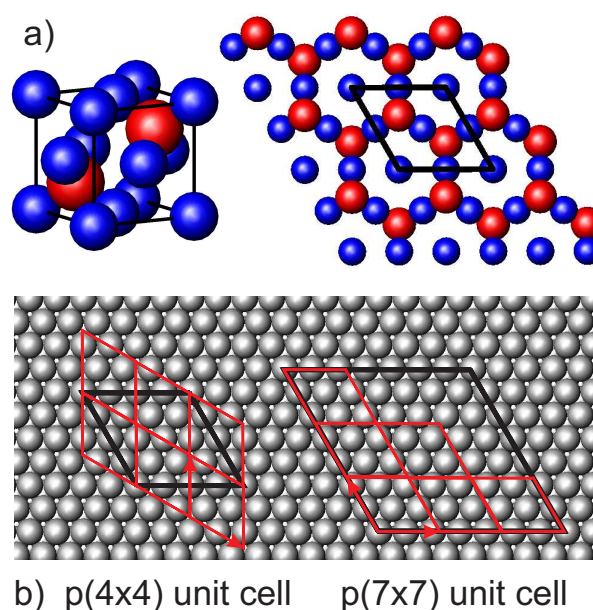


Figure 6.15: a) Ag_2O bulk unit cell and a three-layer slab of $\text{Ag}_2\text{O}(111)$. Silver atoms are shown as blue and oxygen atoms as red spheres. b) Possible orientations of the $\text{Ag}_2\text{O}(111)$ surface unit cell on Ag(111). Previously proposed orientation of the $p(4 \times 4)$ reconstruction on Ag(111), showing a row matching. Honeycomb on hexagon arrangement resulting in a $p(7 \times 7)$ coincidence structure.

Fcc Ag is transformed into Ag_2O by occupation of one quarter of its tetrahedral sites by oxygen accompanied by a lattice expansion of 15 %. The lattice constants of the hexagonal unit cell of $\text{Ag}_2\text{O}(111)$ are $a = b = 6.675 \text{ \AA}$ and $c = 8.175 \text{ \AA}$. The trilayer $\text{Ag}_2\text{O}(111)$ structure consists of a hexagonal ring structure, which is composed

of straight O-Ag-O chains. A silver atom is located in the middle of each O-Ag ring. The unit cell of Ag_2O and a three-layer slab of $\text{Ag}_2\text{O}(111)$ is shown in figure 6.15 a).

Two possible orientations of a $\text{Ag}_2\text{O}(111)$ unit cell on $\text{Ag}(111)$ are shown in figure 6.15 b). Although for the left orientation a row matching perpendicular to the a and b axis with a misfit of less than 0.1 % is present, it has not been observed experimentally. A honeycomb on hexagon arrangement resulting in a $p(7\times 7)$ coincidence structure is observed in this study both for bulk oxide islands as well as for a 2D surface oxide layer. The large misfit for the honeycomb on hexagon arrangement between the oxide and the metal is compensated by a coincidence structure, in which 3 $\text{Ag}_2\text{O}(111)$ surface unit cells fit within a misfit of 1 % onto 7 $\text{Ag}(111)$ surface unit cells, as sketched schematically in the right part of 6.15 b). This emerging coincidence lattice gives rise to a $p(7\times 7)$ superstructure of the 2D surface layer.

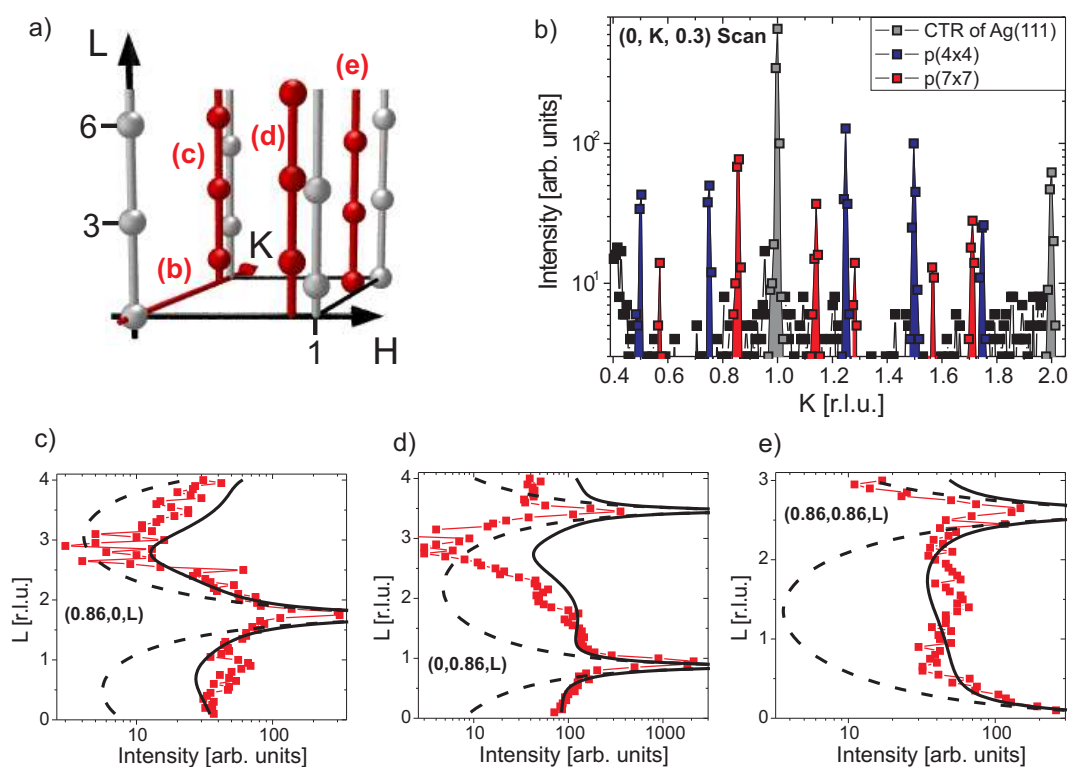


Figure 6.16: a) Sketch of reciprocal space, showing the $\text{Ag}_2\text{O}(111)$ CTRs (red) and the $\text{Ag}(111)$ CTRs (grey). Positions of Bulk Bragg peaks are marked by spheres. b) In-plane K scan ($L=0.3$) showing the coexistence of three oxygen-induced superstructures. c-e) L-Scans along the CTRs for $\text{Ag}_2\text{O}(111)$ (data points). The dashed lines are calculated CTRs of bulk terminated $\text{Ag}_2\text{O}(111)$; their intensity was adjusted to the tails of the Bragg reflections. The solid line represents a simulation of the diffracted intensity including the contribution of the 2D layer as described in the text.

After exposure to 1 bar O_2 at 773 K and cooling down to room temperature under constant O_2 pressure, reciprocal space scans in H and K direction at $L=0.3$ have been performed at 10 mbar O_2 pressure. Typical experimental results are shown in figure 6.16. In addition to the crystal truncation rods (CTRs) of the Ag(111) surface at $H=1$ and $H=2$, two different sets of diffraction spots are observed, as explained in the following: reflections are visible at $H=4/7, 6/7, 8/7, 9/7, 11/7$ and $12/7$, compatible with a $p(7\times 7)$ superstructure. In addition we observe reflections at $H=1/2, 3/4, 5/4, 3/2$ and $7/4$, originating from the $p(4\times 4)$ reconstruction, which is stable under the preparation conditions described in section 5.1.

To obtain more information on the three-dimensional structure of the oxide formed, L scans with momentum transfer perpendicular to the surface have been carried out at $(H=0, K=0.86), (H=0.86, K=0), (H=0.86, K=0.86)$ (figures 6.16 c-e)). These H and K values lay in between the nominal positions for CTRs from a $Ag_2O(111)$ surface and for a $p(7\times 7)$ superstructure. Within the experimental resolution, the signal of both structures is detected simultaneously. As a first observation, bulk Bragg reflections are observed at multiples of $\Delta L=3 \times 0.86$, corresponding to the fcc stacking of subsequent Ag planes in Ag_2O , with a hexagon-on-hexagon arrangement to the Ag(111) surface. It can be clearly recognized that the 'ABC' like stacking of the Ag(111) substrate is not maintained, because e.g. on the $(0,0.86)$ rod reflections at $L=0.86$ and $L=4 \times 0.86$ are observed, whereas for the corresponding Ag $(0,1)$ rod reflections at $L=2$ and $L=5$ are present. The resulting 'CBA' stacking inversion is visualized in figure 6.17.

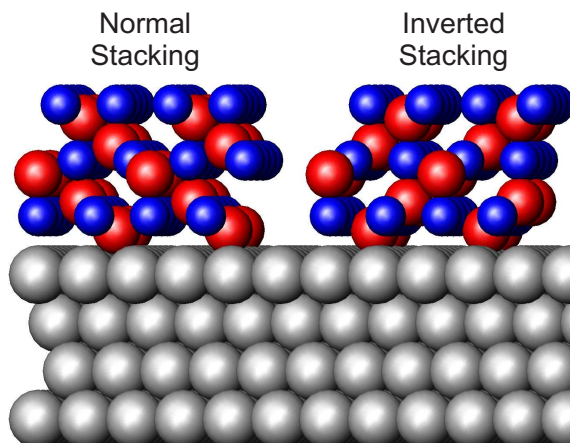


Figure 6.17: Inverted and normal stacking sequence of $Ag_2O(111)$ on $Ag(111)$. Under the experimental conditions applied in this study, the inverted stacking is favoured. Silver atoms are shown as blue and oxygen atoms as red spheres.

Interestingly, the same epitaxial orientation and stacking inversion was reported for the iso-structural system of cuprite $Cu_2O(\bar{1}\bar{1}\bar{1})$ on $Cu(111)$ under electrochemical conditions [93].

Bulk Ag_2O grows in form of domains with a wide height distribution, as we can conclude from the missing finite film thickness oscillations in the L scans in figure 6.16 c)-e). In addition, in specular reflectivity measurements (not shown here), no film thickness oscillations were observed, in agreement with a very rough surface. Nevertheless, from the width of the Bragg peaks in the L direction, a height of 50 Å can be estimated. For a 50 Å thick, homogeneous Ag_2O film, the intensity of the Ag_2O Bragg reflections is expected to be orders of magnitude higher than observed experimentally. Therefore, we argue that the Ag_2O bulk oxide does not cover the whole surface and grows as islands. The stacking inversion of the Ag planes in the bulk oxide islands is not compatible with the simple picture of Ag_2O formation, that oxygen atoms would enter into the Ag substrate, thereby occupying tetrahedral sites and expanding the Ag lattice to Ag_2O . Instead, a silver mass transport perpendicular to the surface must be invoked to grow the Ag_2O islands.

6.5.2 $\text{O-p}(7 \times 7)/\text{Ag}(111)$: A surface oxide

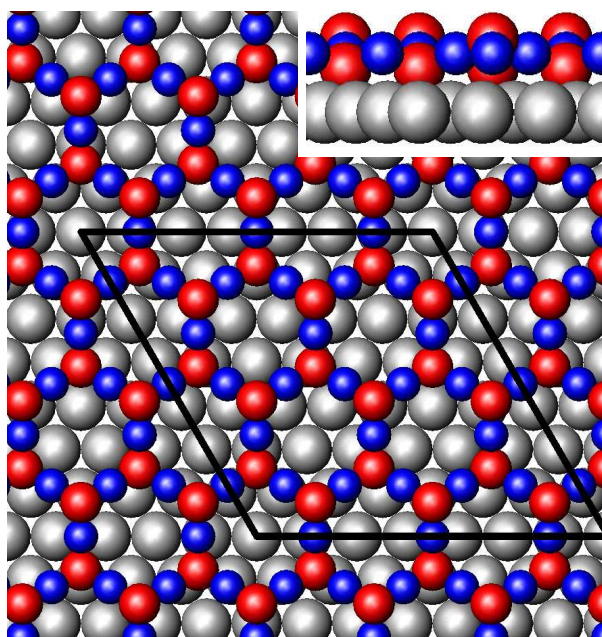


Figure 6.18: Structural model of the surface oxide with $p(7 \times 7)$ coincidence structure. In the inset a side view is presented. Silver atoms are shown as blue and oxygen atoms as red spheres. Hexagon on hexagon arrangement of silver atoms is visible at the origin of the unit cell.

Surprisingly, we observe additional signal in the L scans in figure 6.16 c)-e) in-between the Ag_2O Bragg reflections. If we assume a perfectly smooth $\text{Ag}_2\text{O}(111)$ surface, one would expect a CTR signal plotted as dashed line in figure 6.16 c)-e), falling

significantly below the experimental data points. The remaining intensity, which is varying slowly along the oxide rods, can be explained by the presence of a 2D layer, laterally coexisting with the Ag_2O islands. This layer exhibits the same in-plane epitaxial alignment and interatomic row distances as the $\text{Ag}_2\text{O}(111)$ islands. We argue that this 2D layer gives rise to the satellite peaks at multiples of $1/7$ in the K scan in figure 6.16 b). We propose, that this layer forms a $p(7\times 7)$ coincidence structure on top of the $\text{Ag}(111)$ substrate, since 3 unit cells of $\text{Ag}_2\text{O}(111)$ fit almost perfectly on 7 unit cells of $\text{Ag}(111)$, resulting in a lattice mismatch of 1 %. A sketch of the model is shown in figure 6.18. It is build from one silver layer, which is surrounded by two oxygen ion layers in the surface oxide O-Ag-O architecture. The solid line in figures 6.16 c)-e) are simulations of the diffracted intensity based on the structural model shown in figure 6.18, including some rumpling of the first $\text{Ag}(111)$ layer, which is most likely to occur because of the (7×7) coincidence structure. Although we can not perform a rigorous quantitative analysis on the basis of the present data, the model explains the main features in the L scans like the minima at $L\approx 3$. They occur because of the interference of the scattered waves from the Ag atoms in the 2D oxide layer and the rumpled first substrate layer. The stoichiometry of this layer is Ag_9O_6 , in correspondence to the energetically most stable O-Ag-O surface oxide layer on $\text{Ag}(111)$ [19], according to DFT calculations. It was shown in a recent DFT study [18] of O-Ag-O trilayers constructed from a $\text{Ag}_2\text{O}(111)$ slab, that Ag atoms located in the middle of the O-Ag rings are energetically not favourable. A Ag-Ag interface of the $p(7\times 7)$ reconstructed layer and the $\text{Ag}(111)$ substrate is not considered, as it would lead to unfavourable on-top positions of the Ag atoms. We propose, that the observed alignment of the surface oxide layer and the bulk oxide is preferred because of the hexagon on hexagon arrangement of the silver atoms in the oxide layer and the substrate silver atoms, which leads to a low mismatch coincidence structure with a lateral repeat distance of 7 substrate unit cells.

This layer is the first observation of a surface oxide O-Ag-O trilayer on $\text{Ag}(111)$ and should have severe ramifications for our microscopic understanding of the catalytic properties of $\text{Ag}(111)$ facets.

6.6 Stability Diagram of the O/Ag(111)-system

In-situ SXRD is the optimal experimental method to measure the stability diagram of the O/Ag(111)-system from UHV up to an oxygen pressure of 2 bar. The so-called 'pressure gap', describing the discrepancy between UHV studies and the catalytic conditions, was closed by our experiments. Scans in reciprocal space, which are typical for the clean surface, disordered chemisorbed oxygen, the oxygen induced modulation along the (110) direction and the $p(4\times 4)$ reconstruction were measured in dependency of sample temperature and oxygen pressure. The resulting stability diagram of the O/Ag(111)-system is shown in figure 6.19.

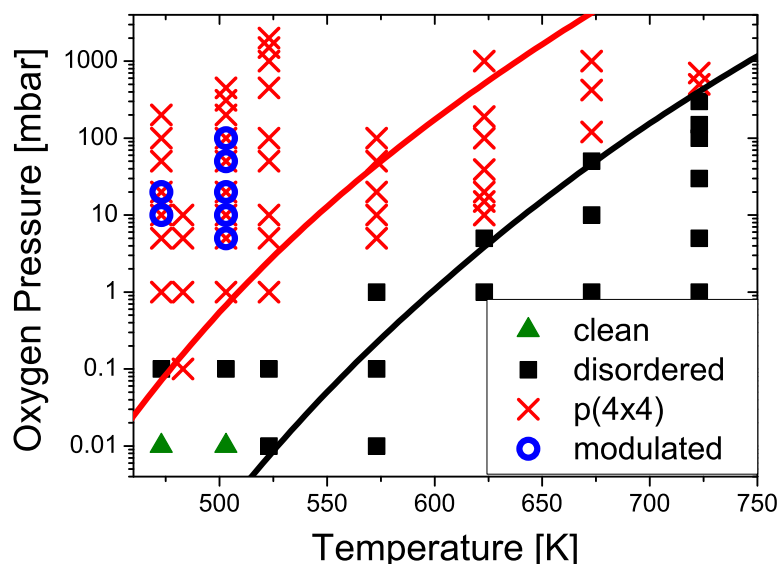


Figure 6.19: Stability diagram of the O/Ag(111)-system measured by in-situ SXR. The black line is the calculated stability border of 1/16 ML chemisorbed oxygen. The red line is the calculated stability border of the Ag₁₂O₆ model including effects due to van der Waals interaction [19]. For the details of the calculations see also chapter 5.5.

A common feature, which was observed for the entire studied temperature range of 473 to 723 K, is, that the oxidation of the Ag(111) surface starts with the formation of disordered chemisorbed oxygen. This oxygen species occupies most likely fcc sites on the silver surface, which was proposed by DFT calculations [16,43,44] and STM measurements [42] and is also in agreement with our SXR and NIXSW measurements (cf. section 6.2). An increase of the oxygen pressure, which is accompanied by an enhanced oxygen coverage, leads to a strong repulsion of the partially negative charged oxygen atoms. The repulsive interaction is stabilised by two different mechanisms. On the one hand, we observed the formation of an incoherent modulation of the Ag(111) surface along the (110) direction, and on the other hand the p(4×4) reconstruction starts to form. We propose, that the modulation is caused by stripes of chemisorbed oxygen with a period length of 10.32 Å on the Ag(111) surface, which seem to minimise the repulsive interaction of the oxygen atoms (cf. section 6.3.1). The stability region of the modulated structure is shown in figure 6.19. The modulation along (110) was always observed in coexistence with the p(4×4) reconstruction and only up to a temperature of 503 K. With increasing oxygen pressure the scattered signal of the modulated structure

decreased, while the signal of the $p(4\times 4)$ structure increased. The incommensurate modulation was only observed up to an oxygen pressure of 100 mbar. We suggest, that the modulated structure is a metastable transient phase, transforming into the $p(4\times 4)$ reconstruction, minimising the repulsive oxygen-oxygen interaction, which is 'frozen' up to a temperature of 503 K.

The measured stability diagram is compared with *ab initio* thermodynamic calculations, resulting in the stability border for disordered chemisorbed oxygen with a coverage of 1/16 ML and the stability border of the Ag_{12}O_6 model of the $p(4\times 4)$ reconstruction including van der Waals interactions of the silver atoms within the Ag_6 triangles, which are shown in figure 6.19. Details of the calculations were already discussed in section 5.5. A good agreement between calculations and measurements is obtained, reproducing the slope of the stability borders for temperatures ≥ 523 K. Between 473 and 503 K kinetic effects play an important role for the formation of the $p(4\times 4)$ reconstruction, since a considerable transport of silver atoms takes place, explaining the rather big discrepancy between calculations and measurements in this temperature region. For temperatures ≥ 523 K only disordered chemisorbed oxygen and the $p(4\times 4)$ reconstruction were observed. Under these conditions both structures are in thermodynamic equilibrium with the surrounding gas phase, resulting in an instantaneous growth or decomposition, if the stability borders are passed (cf. section 5.5).

The incoherent $(\sqrt{3} \times 2.28)\text{rect } R30^\circ$ reconstruction, which was observed by ex-situ LEED measurements after oxidizing the $\text{Ag}(111)$ surface at ~ 430 K and 5 to 10 mbar of oxygen, was not observed during our in-situ SXRD experiments in the temperature range shown in figure 6.19. The model, which was described in section 6.3.2, is built up by oxygen stripes, showing an oxygen coverage of 0.44 ML, being the highest coverage of all observed structures. This high coverage structure seems to be only stabilised at rather low temperatures about 430 K. Similar results are obtained for the $p(5\times 5)$ reconstruction, which was only observed between 423 and 453 K and 1 bar of oxygen in coexistence with the $p(4\times 4)$ structure. The proposed structure of the $p(5\times 5)$ reconstruction is built up by silver triangles, as it is the case for the $p(4\times 4)$ reconstruction, showing an oxygen coverage of 0.36 ML. We suggest, that the $p(5\times 5)$ reconstruction either transforms into the $p(4\times 4)$ reconstruction, which shows an oxygen coverage of 0.375 ML, for higher temperatures, or it decomposes.

An important result is the fact, that the $p(4\times 4)$ reconstruction is stable at 523 K and 2 bar of oxygen, which is close to the industrial conditions for the epoxidation of ethylene. It is still under debate, if the $p(4\times 4)$ reconstruction is stable under real catalytic conditions, when a mixture of oxygen and ethylene is applied [46]. Further in-situ SXRD experiments have to be performed, using mixtures of ethylene and oxygen to answer this question unambiguously.

The formation of the bulk oxide $\text{Ag}_2\text{O}(\bar{1}\bar{1}\bar{1})$ and the $p(7\times 7)$ reconstruction in coexistence with the $p(4\times 4)$ structure was observed after oxidizing the $\text{Ag}(111)$ surface at 773 K and 1 bar of oxygen and cooling down under constant O_2 pressure. Increasing

the temperature from 300 K at 1 bar of oxygen leads to the formation of the $p(4\times 4)$ reconstruction at 420 K, the formation of small amounts of the bulk oxide is observed at 473 K. In addition to the already mentioned growth experiments, we also analysed in-situ the decomposition behaviour of the oxide structures. The $p(4\times 4)$ reconstruction decomposes at 523 K in UHV, whereas the bulk oxide $\text{Ag}_2\text{O}(\bar{1}\bar{1}\bar{1})$ already decomposes at 510 K. Altogether, the bulk oxide shows a higher growth temperature at 1 bar of oxygen and decomposes at lower temperatures than the $p(4\times 4)$ structure. Keeping in mind, that by increasing the temperature at elevated pressures almost no bulk oxide is formed, we suggest, that the $p(4\times 4)$ reconstruction acts as a passivating layer with respect to the formation of the bulk oxide and the $p(7\times 7)$ reconstruction on Ag(111). Only on the small amount of unreconstructed surface area the bulk oxide and the $p(7\times 7)$ coincidence structure can grow. By reducing the temperature from 773 K at 1 bar of oxygen one reaches a temperature region, where the surface is not completely covered by the $p(4\times 4)$ reconstruction. Under these circumstances (523 K and 1 bar of oxygen) the bulk oxide and the $p(7\times 7)$ structure start to form and cover larger surface areas. In both cases a coexistence of the $p(4\times 4)$ reconstruction, $\text{Ag}_2\text{O}(\bar{1}\bar{1}\bar{1})$ and the $p(7\times 7)$ reconstruction is observed. The competing growth of the three observed oxide phases is in line with the observation of different oxygen induced superstructures on Ag(111) with more or less degenerate energetics [20]. Therefore, it is most likely, that not only the $p(4\times 4)$ reconstruction is responsible for the catalytic properties of silver, but also energetically degenerate surface structures or Ag_2O bulk oxide islands.

Chapter 7

Summary

The oxidation behaviour of the Ag(111) surface was studied by systematic in-situ SXRD, HRCLS, NIXSW and LEED measurements, revealing a competing growth of several oxygen induced reconstructions and the bulk oxide Ag₂O in ($\bar{1}\bar{1}\bar{1}$) orientation, which leads to strong implications for the understanding of the catalytic properties of Ag(111) facets. In this chapter the main results are summarised, including a new model of the oxygen induced p(4×4) reconstruction and the observation of a p(7×7) coincidence structure, which is most likely the first observation of a surface oxide on the Ag(111) surface.

The clean Ag(111) Surface

The clean surface is stable under UHV conditions and at low temperatures and low oxygen pressures, before the dissociative chemisorption of oxygen takes place. We have determined the relaxation of the clean Ag(111) surface by SXRD measurements, whereas our results agree with a LEED-I(V) study [41]. The first interlayer spacing is contracted by 1.23 % and the second interlayer spacing by 1.17 %. The results for the fitted Debye-Waller factors of 1.62 Å² for the topmost silver layer and 1.10 Å² for the second silver layer show an enhanced vibrational amplitude, compared to the bulk value of 0.8 Å², which is already adopted by the third silver layer.

Disordered chemisorbed Oxygen

Disordered chemisorbed oxygen is stable in a wide range of oxygen pressure and temperature, prior to the formation of oxygen induced ordered reconstructions, as it was determined by our in-situ SXRD experiments. The height of the oxygen atoms above the first substrate layer is 1.47 ± 0.3 Å, which was determined by means of NIXSW. It is most likely, that the adsorption takes place at on-surface fcc sites, as it was predicted by DFT calculations [16, 43, 44]. The low coherent fraction of the fitted standing wave profile points to a broad height distribution of the oxygen atoms, which is caused by

the disordered nature of the adsorption process, due to the repulsive interaction of the oxygen atoms, resulting in many possibilities of the local binding geometry at the fcc hollow site. The disordered chemisorption process leads to random distortions in the first substrate layer on the order of 0.12 Å, which results from our SXRD measurements. A further increase of the oxygen coverage leads to the formation of ordered structures, which minimise the repulsive oxygen-oxygen interactions. These superstructures will be discussed in the following section.

Oxygen induced Reconstructions and $\text{Ag}_2\text{O}(\bar{1}\bar{1}\bar{1})$

During our SXRD, HRCLS, NIXSW and LEED studies we have observed six different periodic oxygen induced structures: the $p(4\times 4)$, $p(5\times 5)$ and $p(7\times 7)$ reconstructions, the modulation along (110), a $(\sqrt{3} \times 2.28)\text{rect } R30^\circ$ reconstruction and bulk oxide islands in $(\bar{1}\bar{1}\bar{1})$ orientation. All structures can be observed in coexistence with the most prominent superstructure, namely the $p(4\times 4)$ reconstruction.

We have put forward a new Ag_{12}O_6 model of the $p(4\times 4)$ reconstructions, which was determined by a collaborative work, including SXRD, STM, HRCLS measurements and DFT calculations [19]. The structure is build up by two Ag_6 triangles, showing bulk-like silver-silver distances. One triangle is located on fcc sites and the other on hcp sites. The Ag_6 triangles are interlinked by 6 oxygen atoms per unit cell, whereas always to oxygen atoms are located in the furrows between two silver triangles, resulting in an oxygen coverage of 0.375 MLs. The ground state structure determined by DFT at 0 K shows small clockwise and counter-clockwise rotations of the Ag_6 triangles in the surface plane, resulting in an up and down movement of the oxygen atoms. Our SXRD experiments were performed at room temperature. Under these conditions the Ag_6 triangles flip between the two rotational configurations, resulting in a vanishing rotation of the silver triangles and a planar arrangement of the oxygen atoms, as it was obtained by the structural refinement to our SXRD data set, which shows $p6mm$ symmetry. Furthermore, the Ag_{12}O_6 model of the $p(4\times 4)$ reconstruction is not a prototype of a surface oxide in the O-Ag-O trilayer architecture, but rather a nano-structured adsorbate layer.

Additionally, we have determined the stability of the $p(4\times 4)$ reconstruction by our in-situ SXRD measurements. The $p(4\times 4)$ reconstruction is stable for a wide range of oxygen pressure and temperature. Our results are in agreement with *ab initio* thermodynamic calculations, if van der Waals interactions of the silver atoms within the Ag_6 triangles are included. Thereby, the $p(4\times 4)$ structure is stable under the catalytic conditions of the epoxidation of ethylene (523 K and up to 2 bar of oxygen). The $p(4\times 4)$ reconstruction and disordered chemisorbed oxygen are in thermodynamic equilibrium with the surrounding gas phase for temperatures ≥ 523 K. Under these conditions an instantaneous growth or decomposition of the respective phases is observed, if the stability borders are passed.

A modulation of the first silver layer along the (110) direction was observed up

to 503 K during our in-situ SXRD experiments. We propose, that the modulation is caused by stripes of on-surface chemisorbed oxygen with a period length of 10.32 Å. The stripes are aligned perpendicular to the (110) direction and show an oxygen coverage of 0.28 ML. The structure is incoherent along the (110) direction, which is an indication, that the repulsive oxygen-oxygen interactions dominate over the oxygen-silver interactions. We suggest, that the modulated structure is a metastable transient state, which is 'frozen' up to 503 K. With increasing oxygen pressure this structure transforms into the $p(4\times 4)$ reconstruction, as it was observed by our in-situ SXRD measurements.

A $(\sqrt{3} \times 2.28)\text{rect R}30^\circ$ reconstruction was observed by LEED after oxidizing the clean Ag(111) surface at 430 K and 5 to 10 mbar of O_2 . This reconstruction shows a behaviour similar to the modulated structure, since it is also incoherent along the (110) direction. The construction of a model is straightforward, resulting in stripes of on-surface chemisorbed with a period length of 6.59 Å. This model shows an oxygen coverage of 0.44 ML, which is the highest coverage of all observed superstructures. The reconstruction is only stabilised at temperatures around 430 K, due to the strong repulsive interaction of the oxygen atoms. Oxidation of the Ag(111) surface at 430 K and 1 mbar of O_2 leads to a coexistence of the $(\sqrt{3} \times 2.28)\text{rect R}30^\circ$ reconstruction and the $p(4\times 4)$ superstructure.

The formation of adsorbed silver triangles, as it is the case for the $p(4\times 4)$ reconstruction, seems to be a structural building block, which is also observed in the oxygen induced $p(5\times 5)$ structure. This reconstruction is stable between 423 and 453 K at atmospheric oxygen and shows a coexistence with the $p(4\times 4)$ reconstruction. We propose a model, which contains two Ag_{10} triangles, being located on fcc and hcp sites, which are connected by 9 oxygen atoms per unit cell, resulting in an oxygen coverage of 0.36 MLs. The $p(5\times 5)$ reconstruction was not observed for temperatures ≥ 453 K.

We have demonstrated, that bulk $\text{Ag}_2\text{O}(\bar{1}\bar{1}\bar{1})$ grows on Ag(111) in a Stranski-Krastanow like growth mode after exposure to 1 bar of oxygen at 500°C and cooling down to room temperature [21]. The bulk oxide and the 2D surface oxide like layer form a honeycomb on hexagon arrangement with respect to the Ag(111) surface. The 2D layer exhibits a $p(7\times 7)$ coincidence diffraction pattern and its structure is most likely explained by an Ag_9O_6 layer, rotated by 30°, as compared to the alignment in the earlier models for the $p(4\times 4)$ structure. In this model, the bonding of the layer to the substrate is mediated by interfacial oxygen sitting on near on-top, threefold and bridge sites of the Ag(111) surface. The $p(4\times 4)$ reconstruction acts as a passivating layer with respect to the formation of the bulk oxide and the $p(7\times 7)$ structure, since it shows a lower growth temperature at 1 bar of O_2 . Finally, the formation of the bulk oxide islands cannot be explained by simple incorporation of oxygen atoms at tetrahedral sites in the silver bulk. The inverted stacking sequence of the bulk oxide is very likely associated to a silver mass transport perpendicular to the surface plane.

Conclusions

Systematic LEED and in-situ SXRD studies revealed the formation of the $p(5\times 5)$, $p(7\times 7)$ and $(\sqrt{3}\times 2.28)\text{rect } R30^\circ$ reconstructions, the modulated structure and bulk oxide islands, besides the already known $p(4\times 4)$ reconstruction. Furthermore, we have closed the so-called 'pressure gap' by our in-situ SXRD experiments, by measuring the stability diagram of the O/Ag(111)-system. Our results shed new light on the catalytic properties of Ag(111) facets, thereby reconstructions only stabilised at temperatures between 423 and 453 K, as the $(\sqrt{3}\times 2.28)\text{rect } R30^\circ$ and the $p(5\times 5)$ reconstruction, does not seem to play an important role for the catalytic activity of Ag(111) facets, since real catalytic processes are conducted at temperatures between 500 and 600 K. The modulated structure cannot be made responsible for the catalytic activity of silver as well, since it is not stable at atmospheric oxygen pressure. Under the catalytic conditions we have observed a competing growth of the $p(4\times 4)$ reconstruction, the $p(7\times 7)$ coincidence structure and inversely stacked bulk oxide islands. Therefore, it is most likely, that not only the $p(4\times 4)$ reconstruction is responsible for the catalytic properties of silver, but also energetically degenerate surface structures or Ag_2O bulk oxide islands.

Outlook

Further SXRD studies and theoretical modelling have to be performed to confirm the structural models of the $p(5\times 5)$, $p(7\times 7)$ and $(\sqrt{3}\times 2.28)\text{rect } R30^\circ$ reconstructions unambiguously. Additionally, our in-situ SXRD experiments have to be extended to real catalytic conditions, by using mixtures of molecular oxygen and ethylene, to determine the active oxygen species on the Ag(111) surface under these conditions. A final step to a full understanding of the catalytic properties of silver would be the study of epitaxially grown silver nano particles supported on oxides, like Al_2O_3 , MgO or ZnO, under in-situ x-ray diffraction control. In this context, size effects of the nano particles and if oxygen induced reconstructions can form on (111) facets of the nano particles, which were already observed on the Ag(111) surface, should be investigated.

Appendix A

2 and 3D Crystallography

A.1 Ag(111) Surfaces

Silver crystallises in the fcc structure, showing a lattice constant $a_0 = 4.0853 \text{ \AA}$. Commonly, (111) surfaces of fcc metals are described by hexagonal unit cells. The transformation from fcc coordinates \mathbf{A}_i to hexagonal (111) surface coordinates \mathbf{a}_i is given by

$$\mathbf{a}_1 = -\mathbf{A}_1/2 + \mathbf{A}_2/2 \quad (\text{A.1a})$$

$$\mathbf{a}_2 = -\mathbf{A}_2/2 + \mathbf{A}_3/2 \quad (\text{A.1b})$$

$$\mathbf{a}_3 = \mathbf{A}_1 + \mathbf{A}_2 + \mathbf{A}_3 \quad (\text{A.1c})$$

The same transformation holds for the Miller indices H, K and L [23]. \mathbf{a}_1 and \mathbf{a}_2 enclose an angle of 120° and lie in the (111) plane, where $|\mathbf{a}_1| = |\mathbf{a}_2| = a_0/\sqrt{2}$. \mathbf{a}_3 is standing perpendicular to the (111) plane, having a length of $\sqrt{3}a_0$. Resulting in a Ag(111) lattice plane spacing $d_{111} = a_0/\sqrt{3} = 2.36 \text{ \AA}$. The hexagonal unit cell contains 3 atoms, showing p3m1 symmetry [77]. The positions \mathbf{r}_j are

$$\mathbf{r}_1 = \mathbf{0} \quad (\text{A.2a})$$

$$\mathbf{r}_2 = \frac{2}{3}\mathbf{a}_1 + \frac{1}{3}\mathbf{a}_2 + \frac{1}{3}\mathbf{a}_3 \quad (\text{A.2b})$$

$$\mathbf{r}_3 = \frac{1}{3}\mathbf{a}_1 + \frac{2}{3}\mathbf{a}_2 + \frac{2}{3}\mathbf{a}_3, \quad (\text{A.2c})$$

giving rise to an ABC stacking of silver layers along the [001] direction (expressed in surface coordinates). The selection rules for the allowed Bragg reflections can be easily calculated from equations 3.12 and A.2, resulting in

$$2H + K + L = 3m \quad \text{and} \quad H + 2K + 2L = 3n \quad ; m, n \in \mathbb{Z} \quad (\text{A.3})$$

The CTRs can be calculated by equation 3.5. For (1,1,L)-type CTRs one obtains

$$F_{\text{CTR}}(\mathbf{q}) = f_{\text{Ag}} \frac{-e^{-i\pi L/3}}{2i \sin \frac{\pi L}{3}}, \quad (\text{A.4})$$

showing Bragg peaks at $L = 0, 3, 6, \dots$. Similar results are obtained for the (1,0,L) CTR, showing Bragg peaks at $L = 1, 4, 7, \dots$ and the (0,1,L) CTR, showing Bragg peaks for $L = 2, 5, 8, \dots$.

Stacking faults occur to some extent in any fcc metal. Relevant for this study are so-called 'twins', showing an inverted stacking sequence CBA. The twinning has an effect on the shape of the (1,0,L)- and (0,1,L)-type CTRs shown in figure A.1.

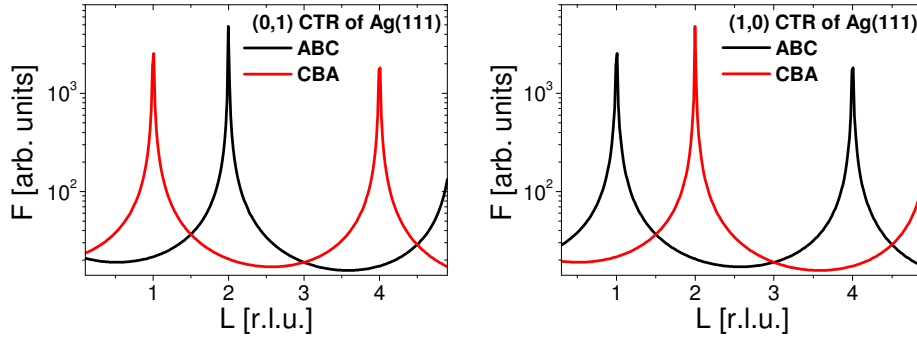


Figure A.1: Effect of twinning on the shape of the (0,1,L) and (1,0,L) CTRs.

(1,1,L), (3,0,L) and (0,3,L)-type CTRs are not sensitive to the stacking sequence.

A.2 2D Crystallography, Wood and Matrix notation

Any surface structure can be classified by 5 types of 2D Bravais 'nets': square, primitive and centred rectangular, hexagonal and oblique [94], described by \mathbf{a}_1 and \mathbf{a}_2 .

Size and orientation of a reconstruction of/on the surface is given by the matrix \mathfrak{M} , defining the in-plane unit cell of the reconstruction, expressed in terms of \mathbf{b}_1 and \mathbf{b}_2 [56].

$$\mathbf{b} = \mathfrak{M} \cdot \mathbf{a} \quad (\text{A.5})$$

The matrix notation can be used to describe any type of reconstruction. Nevertheless, the Wood notation [94] is generally applied to describe a superstructure. In this case, primitive and centred structures are marked by a leading 'p' or 'c'. The length of

\mathbf{b}_1 and \mathbf{b}_2 is given in units of \mathbf{a}_1 and \mathbf{a}_2 , a rotation of x° of the unit cell with respect to the substrate is indicated by $R x^\circ$. A typical example of a reconstruction on a (111) surface of a fcc metal is a $p(\sqrt{3} \times \sqrt{3})R 30^\circ$ reconstruction. The Wood notation cannot be applied if the angle enclosed by the unit cell vectors is different for the reconstruction and the substrate.

Depending on their relation to the substrate lattice, reconstructions can be grouped in 3 types [30]:

- **Simple Structures:** Defined by $|\mathfrak{M}| \in \mathbb{Z}$. In this case \mathbf{a} and \mathbf{b} are simply related to each other. Example: $(\sqrt{3} \times \sqrt{3})R 30^\circ$ on hexagonal surface mesh, where $\mathfrak{M} = \begin{pmatrix} 1 & -1 \\ 1 & 2 \end{pmatrix}$.
- **Incommensurate layers:** Defined by $|\mathfrak{M}| \in \mathbb{Q}$. Typical examples are coincidence structures, like $\mathfrak{M} = \begin{pmatrix} 4/3 & 0 \\ 0 & 4/3 \end{pmatrix}$. In this case, 3 superstructure cells fit perfectly on 4 substrate cells.
- **Incoherent structures:** Defined by $|\mathfrak{M}| \in \mathbb{R}$. In this case no common periodicity between substrate and adlayer exists. This case can be observed, if the interactions between the adatoms exceed the interactions between substrate and adsorbed atoms.

Appendix B

Theoretical Methods

Density Functional Theory (DFT) [95,96] and *ab initio* thermodynamics [97] are commonly used theoretical techniques. One application amongst others is the determination of the structure and stability of oxygen induced reconstructions on surfaces of the late 4d transition metals.

B.1 Density Functional Theory

The ground state of an interacting electron gas in a static potential, cannot be solved analytically due to the interactions of the electrons. In DFT calculations the exchange and correlation effects are included in the functional $E_{xc}[n(\mathbf{r})]$, which is the exchange and correlation energy of the system and $n(\mathbf{r})$ is the electron density [95]. It can be shown, if $n(\mathbf{r})$ is a slowly varying number, that the ground state of the system can be calculated by solving the one-particle Schrödinger equation

$$\left\{ -\frac{1}{2}\nabla^2 + [\varphi(\mathbf{r}) + \mu_{xc}(n(\mathbf{r}))] \right\} \psi_i(\mathbf{r}) = \epsilon_i \psi_i(\mathbf{r}), \quad (\text{B.1a})$$

$$n(\mathbf{r}) = \sum_{i=1}^N |\psi_i(\mathbf{r})|^2. \quad (\text{B.1b})$$

Equation B.1a describes a system of N noninteracting electrons moving in a potential $\varphi(\mathbf{r}) + \mu_{xc}(n(\mathbf{r}))$, where $\mu_{xc}(n(\mathbf{r}))$ is the contribution to the chemical potential due to exchange and correlation. The difficult task is to solve the equations defining φ and μ_{xc} , the stationary condition and equations B.1 self-consistently, which is described in [95] for different approximations. In the last years big advance was made in DFT calculations. Standard code packages like the Vienna *ab initio* simulation package (VASP) are available [96].

The ground state energy and structure of oxygen induced reconstructions of the late 4d transition metals can be calculated nowadays with high precision. The adsorption

energy per oxygen atom is readily calculated from the total energy of the system, as determined by DFT.

B.2 *Ab initio* Thermodynamics

Ab initio thermodynamics is a theoretical approach to extend DFT results, which are calculated for $T = 0$ K and no oxygen partial pressure, to ambient conditions, which are relevant for industrial applications [22, 97, 98].

The surface is thought to be in contact with an oxygen reservoir, giving oxygen atoms to the surface or taking oxygen atoms away, without changing the pressure and temperature of the system. The appropriate thermodynamic potential is the Gibbs free energy $G(T, p, N_{\text{Ag}}, N_{\text{O}})$ for the case of a silver surface. N_{Ag} and N_{O} are the number of silver and oxygen atoms per surface unit cell. The structure with the lowest surface free energy $\gamma(T, p)$ is thermodynamically stable. The surface free energy is given by

$$\gamma(T, p) = \frac{1}{A} \left[G(T, p, N_{\text{Ag}}, N_{\text{O}}) - N_{\text{Ag}} \mu_{\text{Ag}}(T, p) - N_{\text{O}} \mu_{\text{O}}(T, p) \right], \quad (\text{B.2})$$

where A is the area of the surface unit cell and μ_{Ag} and μ_{O} are the chemical potentials of the Ag and O atoms, respectively. For calculations the oxygen chemical potential is referred to half the binding energy of an oxygen molecule $1/2 E_{\text{O}_2}^{\text{total}}$, which is calculated by DFT [22, 98].

$$\Delta\mu_{\text{O}}(T, p) = \mu_{\text{O}}(T, p_{\text{O}_2}) - \frac{1}{2} E_{\text{O}_2}^{\text{total}}, \quad (\text{B.3})$$

The Gibbs free energy is given by

$$G = F - TS^{\text{vib}} + pV, \quad (\text{B.4a})$$

$$G = E^{\text{total}} + E^{\text{vib}} - TS^{\text{vib}} + pV. \quad (\text{B.4b})$$

It can be shown, that the pV term can be neglected for pressures lower than 100 atm [97]. The energy of the vibrations E^{vib} and their entropic contribution TS^{vib} can be calculated, which is shown in references [22, 97]. In many cases the vibrational contributions can also be neglected.

The oxygen chemical potential, the oxygen pressure and the temperature of the system are related via the ideal gas equation [97]

$$\Delta\mu_{\text{O}}(T, p) = \mu_{\text{O}}(T, p^0) + \frac{1}{2} k_B T \ln \left(\frac{p_{\text{O}_2}}{p^0} \right), \quad (\text{B.5})$$

where $p^0 = 1$ atm. The relevant values of $\mu_{\text{O}}(T, p^0)$ are tabulated in [97]. An approximation for the surface free energy, which is valid for thin oxide layers, neglects

the vibrational contributions and the terms containing the chemical potential of the substrate atoms [98]. The surface free energy is then determined by

$$\gamma(\Delta\mu_{\text{O}}(T, p)) = \frac{N_{\text{O}}}{A} \left[E_{\text{O}}^{\text{bind}} + \Delta\mu_{\text{O}} \right]. \quad (\text{B.6})$$

The binding energy per oxygen atom $E_{\text{O}}^{\text{bind}} = E^{\text{total}}/N_{\text{O}}$ is obtained by total energy calculations of the system by means of DFT. The phase diagram is determined by computing equation B.6 for all oxygen induced structures, where the clean surface is stable for $\gamma = 0 \text{ eV}/\text{\AA}^2$. The higher the oxygen content the steeper the slope of $\gamma(\Delta\mu_{\text{O}})$. The stable phase in terms of $\Delta\mu_{\text{O}}$, is the one showing the smallest surface free energy. By using equation B.5, the phase diagram in terms of temperature and oxygen pressure can be calculated.

Appendix C

Abbreviations and Acronyms

AES	Auger Electron Spectroscopy
ANKA	Ångströmquelle Karlsruhe
BM	Bending Magnet
CTR	Crystal Truncation Rod
DFT	Density Functional Theory
DŠ	Doniach-Šunjić
DWF	Debye-Waller Factor
ESCA	Electron Spectroscopy for Chemical Analysis
ESRF	European Synchrotron Radiation Facility
FWHM	Full Width at Half Maximum
HRCLS	High Resolution Core Level Spectroscopy
ID	Insertion Device
L	Langmuir
LEED	Low Energy Electron Diffraction
MAX-lab	Synchrotron in Lund, Sweden
ML	Monolayer
NIXSW	Normal Incidence X-Ray Standing Wave Absorption
RTR	Region of Total external Reflection
STM	Scanning Tunneling Microscopy
SXRD	Surface X-Ray Diffraction
TDS	Thermal Diffuse Scattering
TPD	Temperature Programmed Desorption
UHV	Ultra High Vacuum
VASP	Vienna ab initio Simulation Package
VUV	Vacuum Ultraviolet
XIF	X-Ray Interference Field
XPS	X-Ray Photoelectron Spectroscopy
XSW	X-Ray Standing Wave

Appendix D

Symbols used in Equations

Surface X-Ray Diffraction

λ	photon wavelength
\mathbf{k}_i	wave vector of incident x-rays
\mathbf{k}_f	wave vector of scattered wave
$\mathbf{a}_i \ i = 1, 2, 3$	unit cell vectors in real space
$\mathbf{q} = \mathbf{k}_f - \mathbf{k}_i = \mathbf{q}_{\parallel} + \mathbf{q}_z$	wave vector transfer
\mathbf{q}_{\parallel}	in-plane momentum transfer
\mathbf{q}_z	out-of-plane momentum transfer
$I(\mathbf{q})$	scattered intensity
$A(\mathbf{q})$	scattering amplitude
r_0	classical electron radius
$f_j(\mathbf{q})$	atomic form factor
$F(\mathbf{q})$	structure factor of the unit cell
2ϑ	angle between \mathbf{k}_i and \mathbf{k}_f
N	number of illuminated unit cells
H, K and L	Miller indices
$\mathbf{G} = H\mathbf{a}_1^* + K\mathbf{a}_2^* + L\mathbf{a}_3^*$	reciprocal lattice vector
ε	absorption per atomic layer
Θ	coverage
\mathbf{b}_1 and \mathbf{b}_2	in-plane unit cell vectors of a reconstructed surface
\mathfrak{M}	matrix, which relates \mathbf{b} and \mathbf{a}
$n = 1 - \delta - i\beta$	index of refraction
ρ	electron density
α_i	incident angle with respect to the surface plane
α_f	exit angle
α_c	critical angle for total external reflection
δ	instantaneous displacement of an atom
$e^{-M_j(q^2, T)}$	Debye-Waller factor

$B_j(T) = 8\pi^2 \langle \delta_{qj}^2(T) \rangle$	temperature factor
$P(\mathbf{X})$	Patterson function
V	volume of the unit cell in real space
θ	rocking angle
$\frac{d\sigma}{d\Omega}$	differential scattering cross section
I_{int}	integrated intensity
χ^2	goodness of the fit
M	number of data points
p	number of fitting parameters
$\varsigma(\mathbf{q})$	total error bar

High Resolution Core Level Spectroscopy

E_{kin}	kinetic energy of the photoelectron
E_{bind}	binding energy of the electron
h	Planck's constant
$h\nu$	photon energy
Φ	work function of the metal
$Y(\Delta E)$	photoelectron yield function
ΔE	energy offset
Γ	gamma function
α	asymmetry parameter
γ	lifetime of the core hole

Normal Incidence X-Ray Standing Waves

\mathbf{K}	wave vector of incoming wave outside the crystal
$ \mathbf{K} = 1/\lambda = k$	value of incoming wave vector
\mathbf{K}_0	wave vector of incident wave inside the crystal
\mathbf{K}_H	wave vector of scattered wave inside the crystal
d	lattice plane spacing
\mathbf{H} ; $ \mathbf{H} = 1/d$	wave vector transfer
$F(\mathbf{H}) = F' + iF''$	structure factor
$\kappa(\mathbf{r})$	complex dielectric constant
$\Gamma = r_0 \lambda^2 / \pi V$	abbreviation
$\hbar = h/2\pi$	Planck's constant
$\hbar\omega$	photon energy
$f(\mathbf{H}) + f'(\hbar\omega) + if''(\hbar\omega)$	atomic form factor with dispersion corrections
\mathfrak{A}	electric or magnetic field vector

\mathbf{E}	electric field vector
\mathbf{H}	magnetic field vector
E_0	electric field amplitude of incident wave
E_H	electric field amplitude of scattered wave
P	polarisation factor
ξ_0	difference between $ \mathbf{K}_0 $ and k corrected by n_{material}
ξ_H	difference between $ \mathbf{K}_H $ and k corrected by n_{material}
s_0	offset of the Bragg peak
m	order of the Bragg reflection
D	distance of diameter points of the dispersion surface
ϑ or ϑ_B	Bragg angle
$\Delta\vartheta$	offset from the Bragg angle ϑ
$\eta = \eta' + i\eta''$	complex variable, used for the calculation of the Darwin curve
R	reflected intensity
w_D^{FWHM}	angular full width at half maximum of the Darwin curve
w^{RTR}	width of the region of total external reflection
χ_H	Fourier component of the susceptibility
c	speed of light in vacuum
\mathbf{e}_0 and \mathbf{e}_H	polarisation unit vectors
v	phase between E_0 and E_H
M_{fi}	matrix element
$ i\rangle$	initial state
$ f\rangle$	final state
$\hat{p} = -i\hbar\nabla$	momentum operator
Y_{dip}^H	photoelectron yield in dipole approximation
F^H	coherent fraction
P^H	coherent position
Y^H	generalised yield function
S_R, S_I and ψ	multipole corrections

Low Energy Electron Diffraction

λ	wavelength of the electron
p	momentum of the electron
$\lambda = h/p$	de Broglie relation

Density Functional Theory

$n(\mathbf{r})$	electron density
-----------------	------------------

$E_{xc}[n(\mathbf{r})]$	functional of the electron energy due to exchange and correlations
∇	nabla operator
$\varphi(\mathbf{r})$	static potential of the atoms
$\mu_{xc}(n(\mathbf{r}))$	chemical potential due to exchange and correlations
$\psi_i(\mathbf{r})$	one-particle wave function
ϵ_i	eigenvalue of the Hamiltonian

***Ab initio* Thermodynamics**

G	Gibbs free energy
T	temperature
p	pressure
γ	surface free energy
A	area of the surface unit cell
N_X	number of atoms of element X per surface unit cell
μ	chemical potential
$1/2 E_{O_2}^{\text{total}}$	half binding energy of an oxygen molecule
$\Delta\mu_O(T, p)$	chemical potential referred to $1/2 E_{O_2}^{\text{total}}$
F	free energy
S	entropy
V	volume
p^0	atmospheric oxygen pressure
k_B	Boltzmann's constant
E^{total}	total energy of the system determined by DFT
E_O^{bind}	binding energy per oxygen atom

Bibliography

- [1] E. Lundgren, A. Mikkelsen, J. N. Andersen, G. Kresse, M. Schmid, and P. Varga. Surface oxides on close-packed surfaces of late transition metals. *J. Phys.: Condens. Matter*, **18** R481, (2006).
- [2] H. Over, Y. D. Kim, A. P. Seitsonen, S. Wendt, E. Lundgren, M. Schmid, P. Varga, A. Morgante, and G. Ertl. Atomic-Scale Structure and Catalytic Reactivity of the RuO₂(110) Surface. *Science*, **287** 1474, (2000).
- [3] M. Todorova, E. Lundgren, V. Blum, A. Mikkelsen, S. Gray, J. Gustafson, M. Borg, J. Rogal, K. Reuter, J. N. Andersen, and M. Scheffler. The Pd(100)-($\sqrt{5} \times \sqrt{5}$)R27°-O surface oxide revisited. *Surf. Sci.*, **541** 101, (2003).
- [4] J. Gustafson, A. Mikkelsen, M. Borg, E. Lundgren, L. Köhler, G. Kresse, M. Schmid, P. Varga, J. Yuhara, X. Torrelles, C. Quirós, and J. N. Andersen. Self-Limited Growth of a Thin Oxide Layer on Rh(111). *Phys. Rev. Lett.*, **92** 126102, (2004).
- [5] T. Reiss and G. Luft. Katalysator- und Inhibitorverhalten in der instationären Formierungsphase eines Silberträgerkatalysators zur Synthese von Ethylenoxid. *Chem. Ing. Tech.*, **68** 165, (1996).
- [6] R. J. Chimentão, I. Kirm, F. Medina, X. Rodríguez, Y. Cesteros, P. Salagre, J. E. Sueiras, and J. L. G. Fierro. Sensitivity of styrene oxidation reaction to the catalyst structure of silver nanoparticles. *Appl. Surf. Sci.*, **252** 793, (2005).
- [7] S. N. Goncharova, E. A. Paukshtis, and B. S. Bal'zhinimaev. Size effects in ethylene oxidation on silver catalysts. Influence of support and Cs promoter. *Appl. Catal. A*, **126** 67, (1995).
- [8] A. Nagy, G. Mestl, D. Herein, G. Weinberg, E. Kitzelmann, and R. Schlögl. The Correlation of Subsurface Oxygen Diffusion with Variations of Silver Morphology in the Silver-Oxygen System. *Jour. Catal.*, **182** 417, (1999). and references therein.
- [9] G. Rovida, F. Pratesi, M. Maglietta, and E. Ferroni. Effects of Oxygen on Silver Surface Structure. *J. Vac. Sci. Technol.*, **9** 796, (1972).

- [10] G. Rovida, F. Pratesi, M. Maglietta, and E. Ferroni. Chemisorption of Oxygen on the Silver (111) Surface. *Surf. Sci.*, **43** 230, (1974).
- [11] C. T. Campbell. Atomic and Molecular Oxygen Adsorption on Ag(111). *Surf. Sci.*, **157** 43, (1985).
- [12] S. R. Bare, K. Griffiths, W. N. Lennard, and H. T. Tang. Generation of atomic oxygen on Ag(111) and Ag(110) using NO₂: a TPD, LEED, HREELS, XPS and NRA study. *Surf. Sci.*, **342** 185, (1995).
- [13] A. Nagy and G. Mestl. High temperature partial oxidation reactions over silver catalysts. *Appl. Catal. A*, **188** 337, (1999). and references therein.
- [14] V. I. Bukhtiyarov, V. V. Kaichev, and I. P. Prosvirin. Oxygen adsorption on Ag(111): X-ray photoelectron spectroscopy (XPS), angular dependent x-ray photoelectron spectroscopy (ADXPS) and temperature-programmed desorption (TPD) studies. *Jour. Chem. Phys.*, **111** 2169, (1999).
- [15] C. I. Carlisle, D. A. King, M.-L. Bocquet, J. Cerdá, and P. Sautet. Imaging the Surface and the Interface Atoms of an Oxide Film on Ag(111) by Scanning Tunneling Microscopy: Experiment and Theory. *Phys. Rev. Lett.*, **84** 3899, (2000).
- [16] A. Michaelides, M.-L. Bocquet, P. Sautet, A. Alavi, and D. A. King. Structures and thermodynamic phase transitions for oxygen and silver oxide phases on Ag(111). *Chem. Phys. Lett.*, **367** 344, (2003).
- [17] W. X. Li, C. Stampfl, and M. Scheffler. Why is a Noble Metal Catalytically Active? The Role of the O-Ag Interaction in the Function of Silver as an Oxidation Catalyst. *Phys. Rev. Lett.*, **90** 256102, (2003). and references therein.
- [18] A. Michaelides, K. Reuter, and M. Scheffler. When seeing is not believing: Oxygen on Ag(111), a simple adsorption system? *J. Vac. Sci. Technol. A*, **23** 148, (2005).
- [19] M. Schmid, A. Reicho, A. Stierle, I. Costina, J. Klikovits, P. Kostelnik, O. Dubay, G. Kresse, J. Gustafson, E. Lundgren, J. N. Andersen, H. Dosch, and P. Varga. Structure of Ag(111)-p(4×4)-O: No Silver Oxide. *Phys. Rev. Lett.*, **96** 146102, (2006).
- [20] J. Schnadt, A. Michaelides, J. Knudsen, R. T. Vang, K. Reuter, E. Lægsgaard, M. Scheffler, and F. Besenbacher. Revisiting the Structure of the p(4×4) Surface Oxide on Ag(111). *Phys. Rev. Lett.*, **96** 146101, (2006).
- [21] A. Reicho, A. Stierle, I. Costina, and H. Dosch. Stranski-Krastanov like oxide growth on Ag(111) at atmospheric oxygen pressures. *Surf. Sci. Lett.*, **601** L19, (2007).

- [22] W.-X. Li, C. Stampfl, and M. Scheffler. Insights into the function of silver as an oxidation catalyst by *ab initio* atomistic thermodynamics. *Phys. Rev. B*, **68** 165412, (2003).
- [23] B. E. Warren. *X-Ray Diffraction*. Dover Publications, Inc., Mineola, (1990).
- [24] J. Als-Nielsen and D. McMorrow. *Elements of Modern X-Ray Physics*. John Wiley and Sons, Ltd., Chichester, (2001).
- [25] I. K. Robinson. Crystal truncation rods and surface roughness. *Phys. Rev. B*, **33** 3830, (1986).
- [26] I. K. Robinson and D. J. Tweet. Surface x-ray diffraction. *Rep. Prog. Phys.*, **55** 599, (1992).
- [27] R. Feidenhans'l. Surface Structure Determination by X-Ray Diffraction. *Surf. Sci. Rep.*, **10** 105, (1989).
- [28] E. Vlieg. ROD: a program for surface X-ray crystallography. *J. Appl. Cryst.*, **33** 401, (2000).
- [29] H. Dosch. Critical Phenomena at Surfaces and Interfaces. In *Springer Tracts in Modern Physics*, volume 126. Springer Verlag, Berlin, (1992).
- [30] G. Ertl and J. Küppers. *Low Energy Electrons and Surface Chemistry*. VCH, Weinheim, (1985).
- [31] M. Smedh. *Molecular overlayers on homogeneous and heterogeneous metal surfaces studied by core-level photoemission*. PhD thesis, Lund University, (2001).
- [32] M. Henzler and W. Göpel. *Oberflächenphysik des Festkörpers*. Teubner, Stuttgart, (1991).
- [33] B. W. Batterman and H. Cole. Dynamical Diffraction of X-Rays by Perfect Crystals. *Rev. Mod. Phys.*, **36** 681, (1964).
- [34] J. Zegenhagen. Surface structure determination with X-Ray standing waves. *Surf. Sci. Rep.*, **18** 199, (1993).
- [35] D. P. Woodruff. Normal Incidence X-Ray Standing Wave Determination of Adsorbate Structures. *Prog. Surf. Sci.*, **57** 1, (1998).
- [36] A. Caticha and S. Caticha-Ellis. Dynamical theory of x-ray diffraction at Bragg angles near $\pi/2$. *Phys. Rev. B*, **25** 971, (1982).
- [37] A. Stierle, A. Steinhäuser, A. Rühm, F. U. Renner, R. Weigel, N. Kasper, and H. Dosch. Dedicated Max-Planck beamline for the *in situ* investigation of interfaces and thin films. *Rev. Sci. Instr.*, **75** 5302, (2004).

- [38] R. Nyholm, J. N. Andersen, U. Johansson, B. N. Jensen, and I. Lindau. Beamline I311 at MAX-LAB: a VUV/soft X-ray undulator beamline for high resolution electron spectroscopy. *Nucl. Inst. Meth. Phys. Res. A*, **467-468** 520, (2001).
- [39] N. Måtensson, P. Baltzer, P. A. Brühwiler, J.-O. Forsell, A. Nilsson, A. Stenborg, and B. Wannberg. A very high resolution electron spectrometer. *J. Elec. Spectr. Rel. Phen.*, **70** 117, (1994).
- [40] ESRF ID32. Beamline Layout. <http://www.esrf.eu/UsersAndScience/Experiments/SurfaceScience/ID32/Beamline>.
- [41] E A Soares, G S Leatherman, R D Diehl, and M A Van Hove. Low-energy electron diffraction study of the thermal expansion of Ag(111). *Surf. Sci.*, **468** 129, (2000).
- [42] C. I. Carlisle, T. Fujimoto, W. S. Sim, and D. A. King. Atomic imaging of the transition between oxygen chemisorption and oxide film growth on Ag(111). *Surf. Sci.*, **470** 15, (2000).
- [43] W.-X. Li, C. Stampfl, and M. Scheffler. Oxygen adsorption on Ag(111): A density-functional theory investigation. *Phys. Rev. B*, **65** 075407, (2002).
- [44] D. Torres, K. M. Neyman, and F. Illas. Oxygen atoms on the (111) surface of coinage metals: On the chemical state of the adsorbate. *Chem. Phys. Lett.*, **429** 86, (2006).
- [45] I. N. Stranski and L. Krastanow. Zur Theorie der orientierten Ausscheidung von Ionenkristallen aufeinander. *Sitzungsber. Akad. Wissenschaften Wien*, **146** 797, (1938).
- [46] R. Reichelt, S. Günther, M. Rößler, J. Winterlin, B. Kubias, B. Jakobi, and R. Schlögl. High-pressure STM of the interaction of oxygen with Ag(111). *Phys. Chem. Chem. Phys.*, **9** 3590, (2007).
- [47] WebElements Periodic Table. Elemental properties. <http://www.webelements.com>.
- [48] C. Leygraf and T. Graedel. *Atmospheric Corrosion*. John Wiley and Sons, New York, (2000).
- [49] L. H. Tjeng, M. B. J. Meinders, J. van Elp, J. Ghijsen, G. A. Sawatzky, and R. L. Johnson. Electronic structure of Ag₂O. *Phys. Rev. B*, **41** 3190, (1990).
- [50] M.-L. Bocquet, A. Michaelides, P. Sautet, and D. A. King. Initial stages in the oxidation and reduction of the 4×4 surface oxide phase on Ag(111): A combined density-functional theory and STM simulation study. *Phys. Rev. B*, **68** 075413, (2003).

- [51] M. Todorova, W. X. Li, M. V. Ganduglia-Pirovano, C. Stampfl, K. Reuter, and M. Scheffler. Role of Subsurface Oxygen in Oxide Formation at Transition Metal Surfaces. *Phys. Rev. Lett.*, **89** 096103, (2002).
- [52] W.-X. Li, C. Stampfl, and M. Scheffler. Subsurface oxygen and surface oxide formation at Ag(111): A density-functional theory investigation. *Phys. Rev. B*, **67** 045408, (2003).
- [53] W. L. Bragg. The Diffraction of Short Electromagnetic Waves by a Crystal. *Proc. Camb. Phil. Soc.*, **17** 43, (1913).
- [54] W. Friedrich, P. Knipping, and M. Laue. Interferenzerscheinungen bei Röntgenstrahlen. *Ann. Phys.*, **346** 971, (1913). Previously published in *Sitzungsberichte der Königlich Bayerischen Akademie der Wissenschaften*, 1912.
- [55] M. Becker. Spannungsinduziertes Legieren und Entmischen an metallischen Grenzflächen. Diploma thesis, Universität Stuttgart, (2004).
- [56] R. L. Park and H. H. Madden. Annealing Changes on the (100) Surface of Palladium and their Effect on CO Adsorption. *Surf. Sci.*, **11** 188, (1968).
- [57] A. J. Bradley and S. S. Lu. The Crystal Structures of Cr_2Al and Cr_5Al_8 . *Z. Krist.*, **96** 20, (1937).
- [58] M. Holt, Z. Wu, H. Hong, P. Zschack, P. Jemian, J. Tischler, H. Chen, and T.-C. Chiang. Determination of Phonon Dispersions from X-Ray Transmission Scattering: The Example of Silicon. *Phys. Rev. Lett.*, **83** 3317, (1999).
- [59] I. Ramsteiner. *High-Energy X-Ray Study of Short Range Order and Phase Transformations in Titanium-Vanadium*. PhD thesis, Universität Stuttgart, (2005). and references therein.
- [60] M. Mezger. Diffuse Röntgenstreuung an Ni-Pd Legierungen. Diploma thesis, Universität Stuttgart, (2004). and references therein.
- [61] M. V. Linkoaho. The X-ray Debye Temperatures of V, Ni, Cu, Nb and Ag from the measured Integrated Intensities at 300 K and 4 K. *Phil. Mag.*, **23** 191, (1971). and references therein.
- [62] A. L. Patterson. A Fourier Series Method for the Determination of the Components of Interatomic Distances in Crystals. *Phys. Rev.*, **46** 372, (1934).
- [63] H. Lipson and W. Cochran. *The determination of crystal structures*. G. Bell and Sons, Ltd., London, (1968).
- [64] E. Vlieg. Integrated Intensities Using a Six-Circle Surface X-ray Diffractometer. *J. Appl. Cryst.*, **30** 532, (1997).

- [65] E. Vlieg. ANA-ROD. http://www.esrf.eu/computing/scientific/joint_projects/ANA-ROD.
- [66] UK Surface Analysis Forum. Online Databases. <http://www.uksaf.org/data.html#1>.
- [67] XPS International. Fundamental XPS Data from Pure Elements, Pure Oxides, and Chemical Compounds. <http://www.xpsdata.com>.
- [68] M. P. Seah and W. A. Dench. Quantitative Electron Spectroscopy of Surfaces: A Standard Data Base for Electron Inelastic Mean Free Paths in Solids. *Surf. Inter. Anal.*, **1** 2, (1979).
- [69] S. Doniach and M. Šunjić. Many-electron singularity in x-ray photoemission and x-ray line spectra from metals. *J. Phys. C.*, **3** 285, (1970).
- [70] C. G. Darwin. The Theory of X-Ray Reflexion. *Phil. Mag.*, **27** 315, (1914).
- [71] C. G. Darwin. The Theory of X-Ray Reflexion. Part II. *Phil. Mag.*, **27** 675, (1914).
- [72] P. P. Ewald. Zur Begründung der Kristallogik Teil I: Theorie der Dispersion. *Ann. Physik*, **49** 1, (1916).
- [73] P. P. Ewald. Zur Begründung der Kristallogik Teil III: Die Kristallogik der Röntgenstrahlen. *Ann. Physik*, **54** 519, (1917).
- [74] M. von Laue. Die dynamische Theorie der Röntgenstrahlinterferenzen in neuer Form. *Ergeb. Exakt. Naturw.*, **10** 133, (1931).
- [75] Lawrence Berkeley National Laboratory. Center for X-Ray Optics. <http://www-cxro.lbl.gov/>.
- [76] National Institute of Standards and Technology. X-Ray Form Factor, Attenuation, and Scattering Tables. <http://physics.nist.gov/PhysRefData/FFast/Text/cover.html>.
- [77] E. Prince. *International Tables for Crystallography, Volume C*. Kluwer Academic Publishers, Dordrecht, (2004).
- [78] J. B. Marion and M. A. Heald. *Classical Electromagnetic Radiation*. Academic Press, New York, (1980).
- [79] B. W. Batterman. Effect of Dynamical Diffraction in X-Ray Fluorescence Scattering. *Phys. Rev.*, **133** A759, (1964).

- [80] I. Vartanyants, T.-L. Lee, S. Thiess, and J. Zegenhagen. Non-dipole effects in X-ray standing wave photoelectron spectroscopy experiments. *Nucl. Inst. Meth. Phys. Res. A*, **547** 196, (2005).
- [81] D. P. Woodruff. Non-dipole effects in high-energy photoelectron emission; identification and quantification using X-ray standing waves. *Nucl. Inst. Meth. Phys. Res. A*, **547** 187, (2005).
- [82] F. Schwabl. *Quantenmechanik*. Springer Verlag, Berlin, (2002).
- [83] C. Davisson and L. H. Germer. Diffraction of Electrons by a Crystal of Nickel. *Phys. Rev.*, **30** 705, (1927).
- [84] P. Auger. Sur L'Effet Photoélectrique Composé. *J. Phys. Radium*, **6** 205, (1925).
- [85] P. W. Palmberg, G. E. Riach, R.E.Weber, and N.C. MacDonald. *Handbook of Auger Electron Spectroscopy*. Physical Electronics Industries, Edina, (1972).
- [86] Certified Scientific Software. spec. <http://www.certif.com>.
- [87] L. Köhler, G. Kresse, M. Schmid, E. Lundgren, J. Gustafson, A. Mikkelsen, M. Borg, J.Yuhara, J. N. Andersen, M. Marsman, and P. Varga. High-Coverage Oxygen Structures on Rh(111): Adsorbate Repulsion and Site Preference Is Not Enough. *Phys. Rev. Lett.*, **93** 266103, (2004).
- [88] I. Villegas and M. J. Weaver. Carbon monoxide adlayer structures on platinum (111) electrodes: A synergy between *in-situ* scanning tunneling microscopy and infrared spectroscopy. *J. Chem. Phys.*, **101** 1648, (1994).
- [89] J. X. Wang, I. K. Robinson, B. M. Ocko, and R. R. Adzic. Adsorbate-Geometry Specific Subsurface Relaxation in the CO/Pt(111) System. *J. Phys. Chem. B*, **109** 24, (2005).
- [90] A. Menzel, K.-C. Chang, V. Komanicky, Y. V. Tolmachev, A. V. Tkachuk, Y. S. Chu, and H. You. High-density electrosorbed carbon monoxide monolayers on Pt(111) under atmospheric pressure. *Phys. Rev. B*, **75** 035426, (2007).
- [91] S. R. Longwitz, J. Schnadt, E. Kruse Vestergaard, R. T. Vang, E. Lægsgaard, I. Stensgaard, H. Brune, and F. Besenbacher. High-Coverage Structures of Carbon Monoxide Adsorbed on Pt(111) Studied by High-Pressure Scanning Tunneling Microscopy. *J. Phys. Chem. B*, **108** 14497, (2004).
- [92] K.-C. Chang, A. Menzel, V. Komanicky, and H. You. Electrosorbed carbon monoxide monolayers on Pt(111). *Electroch. Acta*, **52** 5749, (2007).
- [93] Y. S. Chu, I. K. Robinson, and A. A. Gewirth. Comparison of aqueous and native oxide formation on Cu(111). *J. Chem. Phys.*, **110** 5952, (1999).

- [94] E. A. Wood. Vocabulary of Surface Crystallography. *J. Appl. Phys.*, **35** 1306, (1964).
- [95] W. Kohn and L. J. Sham. Self-Consistent Equations Including Exchange and Correlation Effects. *Phys. Rev. A*, **140** 1133, (1965).
- [96] G. Kresse and J. Furthmüller. Efficiency of ab-initio total energy calculations for metals and semiconductors using a plane-wave basis set. *Comput. Mater. Sci.*, **6** 15, (1996). and references therein.
- [97] K. Reuter and M. Scheffler. Composition, structure and stability of RuO₂(111) as a function of oxygen pressure. *Phys. Rev. B*, **65** 035406, (2001). and references therein.
- [98] H. Gabasch, W. Unterberger, K. Hayek, Bernhard Klötzer, G. Kresse, C. Klein, M. Schmid, and P. Varga. Growth and decay of the Pd(111)–Pd₅O₄ surface oxide: Pressure-dependent kinetics and structural aspects. *Surf. Sci.*, **600** 205, (2006).

Danksagung

- **Prof. Dr. Helmut Dosch** danke ich, dass er diese Arbeit ermöglicht und stets gefördert hat.
- Mein besonderer Dank gilt **Dr. Andreas Stierle**, für die zahlreichen Diskussionen, Hilfestellungen und seine Unterstützung während der Messzeiten. Des Weiteren hat er die vorliegende Arbeit kritisch korrigiert und so maßgeblich zu ihrem Gelingen beigetragen.
- Ich möchte **Prof. Dr. Ulrich Stroth** danken, dass er sich bereit erklärt hat, den Mitbericht für meine Doktorarbeit zu übernehmen.
- Ohne die Unterstützung der Mitglieder der Oxidationsgruppe wäre diese Arbeit nicht möglich gewesen. Insbesondere möchte ich **Dr. Ioan Costina** danken, der mich zu Beginn meiner Diplomarbeit in die experimentellen Methoden eingeführt hat und bei vielen Strahlzeiten tatkräftig zur Hand gegangen ist. **Dr. Reinhard Streitl** danke ich für seine Einweisung in die Software ROD, **Alina Vlad** für Ihre Einführung in die Photoelektronenspektroskopie und **Dr. Vedran Vonk** für seine Hilfe während der Strahlzeit an BM 25.
- **Annette Weißhardt** danke ich für die exzellente Probenpolitur, ohne die die Experimente nicht möglich gewesen wären.
- **Dr. Nikolai Kasper** und **Ralf Weigel** haben immer für einen reibungslosen Ablauf der Experimente am Synchrotron ANKA gesorgt.
- **Prof. Dr. Edvin Lundgren**, **Dr. Johan Gustafson** und **Prof. Dr. Jesper Andersen** haben maßgeblich zum Gelingen der HRCLS Experimente in Lund beigetragen. Des Weiteren möchte ich Ihnen für die Hilfe bezüglich der Datenauswertung danken.
- Ich möchte **Prof. Dr. Michael Schmid**, **Prof. Dr. Georg Kresse**, **Prof. Dr. P. Varga**, **Dr. J. Klikovits**, **Dr. P. Kostelnik** und **Dr. O. Dubay** für Ihre Kooperation im Rahmen der Strukturbestimmung der $p(4 \times 4)$ Rekonstruktion danken.

- Ich danke **Dr. Jörg Zegenhagen**, der die NIXSW Experimente an ID 32 ermöglicht, durch Diskussionen mir beim Verständnis der theoretischen Grundlagen geholfen und entscheidend an der Datenauswertung mitgewirkt hat. **Dr. Sebastian Thiess** danke ich für die zahlreichen Diskussionen und die Hilfe während der Messzeit. Des Weiteren haben **Dr. Tien-Lin Lee** und **Dr. Frank Uwe Renner** für eine erfolgreiche Durchführung der Experimente an ID 32 gesorgt.
- Mein Dank gilt **Prof. Dr. Wolfgang Moritz, Dr. Hubert Keller, Moritz Becker** und **Bernd Steinheil**, die die Messungen mit der DIVA ermöglicht haben.
- Ich danke **Dr. Germán Castro** und **Dr. Juan Rubio-Zuazo** für Ihre Hilfe während unserer SXR D Experimente an BM 25.
- Meinen Zimmerkollegen **Claus Ellinger, Ulrich Gebhardt** und **Markus Mezger** danke ich für Ihre Hilfe und die vielen Diskussionen, die mir immer weitergeholfen haben.
- Ich danke **allen Mitgliedern der Abteilung Dosch**, die stets für eine angenehme Arbeitsatmosphäre gesorgt haben. Insbesondere haben die Diskussionen mit **Dr. Hubert Keller, Moritz Becker, Philipp Nolte, Bernd Steinheil, Martino Sarcino, Felix Maye** und **Navid Khorshidi** zu einer Festigung meines Wissens in Fragen der Oberflächenröntgenbeugung geführt.
- Herrn **Manfred Grein** möchte ich danken, der immer ein offenes Ohr für mich hatte.
- All meinen 'Eltern' **Reiner, Sibylle, Rudi, Sabine, Marion** und **Roland** danke ich, dass Sie mir das Studium ermöglicht haben und mich in allen Belangen stets unterstützt haben.
- Mein besonderer Dank gilt **meiner Freundin Kathrin**, die mit mir durch dick und dünn gegangen ist, immer an meiner Seite stand und mir die Kraft gegeben hat diese Arbeit zu vollenden.